Stabilization of Floating Wind Turbines

Morten Dinhoff Pedersen

May 18, 2017

Summary

Wind turbines mounted on floating platforms are, under a specific set of circumstances, prone to a phenomena called control-induced resonance. The phenomena materializes as persistent oscillations in the platform's surge and pitch displacement and occurs when pitch-control algorithms without modifications for floating operation are used.

This thesis examines the physical underpinnings of the resonance problem by a novel modeling strategy. A systems approach is adopted where the floating wind turbine is conceived as an interconnection of subsystems. New aerodynamic models suitable for a systems approach are proposed, validated and examined. Notably, a vortex theoretical approach is shown to be fruitful both in the steady and unsteady loading regimes. A new type of dynamic inflow model based on vortex transport and frequency domain identification is proposed and compared favorably to existing strategies. The vortex lifting law is used to generate a succinct model for loads that fits into the systems representation and replaces the commonly used table-data approach. A simplified dynamic model suitable for control analysis is derived and validated against a standard tool in wind-turbine analysis.

The system model developed in the first part of the thesis is used for a small-signal stability analysis invoking passivity tools in the second part. It is shown that floating wind turbines are stable under quite general conditions as long as no pitch control is applied. If collective blade pitch is used for the sole purpose of setpoint control of the angular velocity, destabilization is shown to be inevitable. An examination of the energy flow within the wind turbine system motivates a novel "energy shaping" control strategy. Existing control strategies are also examined in the new paradigm. A case study of a representative 5MW wind turbine is performed. The resonance phenomena is demonstrated under realistic conditions. A number of control strategies are tested and compared. The "energy shaping" control strategy is shown to perform well and eliminates the control-induced resonance. Justification for the results are given based on the theory developed in the thesis.

Acknowledgements

The research borne out in this thesis was carried out at the Norwegian University of Science and Technology in Trondheim (NTNU). The work was supported by the Centre for Ships and Ocean Structures (CeSOS) at the Norwegian University of Science and Technology through the Research Council of Norway (NFR) and its Centres of Excellence funding scheme, project no. 146025/V30. Funding was also provided by the Norwegian Research Centre of Offshore Wind Technology (NOWITECH) through the project 193823/E20.

I owe a debt of gratitude to the many exceptional individuals encountered during my ph.d. work. Thank you Thor Inge Fossen for your open-door policy, patience and can-do attitude. It was a rewarding experience to study under your supervision.

The somewhat protracted research period brought me into teaching quite inadvertently. I wish to extend my sincere thanks to Tor-Arne Johansen for letting me substitute in your course Linear Systems Theory. I have enjoyed that experience immensely. This fall will see my fourth semester as lecturer. My superb TAs Mark Haring and Kristoffer Gryte have kept the ship steady throughout, thank you. Thanks are also extended to Morten Breivik who facilitated other rewarding teaching opportunities. On his behest, I have had the pleasure of compiling a new course on control theory, now in its third year. Thanks goes to Øyvind Stavdahl for giving me a stimulating problem in Neurophysiology and also motivating words. I would be remiss to forget the friendly and capable administrative staff at Tyholt and ITK, you have made my life easier and this is much appreciated.

A multitude of new friends were made in the past years. To the occupants of the wind turbine room Jabus and Mahmoud; please forgive my voluminous digressions on vortex dynamics. To the CeSOS crew Dominik, Tassos, Roberto, Christian, Luca and others, thanks for the enjoyable late night mental resets at Solsiden and beyond.

The person to whom I am most singularly indebted is Edith. I could not have gone this far without your support. Can you believe it? Seven years, two wonderful children and our own home (despite the ph.d.). I look forward to continuing our journey together. Finally, thanks to my father who taught me persistence.

Contents

1. Introduction

Developments in the last decades have made it clear that wind turbines will be one of the major technologies in the effort to provide clean energy. An encouraging read is found in [1]. In 2015 wind power supplied more new power generation than any other technology. The total installed capacity in 2015 was 433 GW of which no less than 17% was added in the same year. This growth is expected to continue in the coming years.

A host of challenges have arisen as an increasing number of turbines are erected throughout the world. Some examples are noise from turbine parks, visual pollution and lack of space. Offshore wind power will help alleviate many of these problems. An offshore wind turbine's noise will not reach the shore and there is plenty of space in which to situate them.

In the year 2015 a total of 3.4 GW of offshore generating capacity was installed in the form of 419 new turbines. This brought the total offshore generating capacity to 12 GW. Due to the need for supports of fixed or floating type, the purchase price of offshore wind turbines will inevitably be higher than their onshore counterparts. The need for additional electric infrastructure also adds to the investment. But, the greater initial investment is offset by higher average wind speeds and lower turbulence when compared to conditions on land [2].

A new approach to offshore wind turbines has been to dispense with the need for fixed foundations altogether; accomplished by attaching the turbines to floating hulls anchored to the seabed. This technology will extend the area turbines can be deployed as one will be far less constrained by the sea-depth.

Several concepts currently exist, see Figure 1.1 for a number of examples. Few of these have made their way to the prototype stage. An exception is the HYWIND turbine, a concept that utilizes a spar-buoy type hull to provide buoyancy. The first prototype is at the time of writing in operational deployment outside Karmøy. It would appear that the testing has been successful, a 30 MW park is planned for 2017 [3].

1.1. Control-induced resonance

The introduction of floating platforms represents a challenge in the design of automatic control. Some particular problems seemingly specific to floating operation have arisen, most notably a *control-induced resonance phenomena*. Control-induced resonances in floating wind turbines were first described in Nielsen et al. [4]. The resonances took the form of severe oscillations in platform surge and

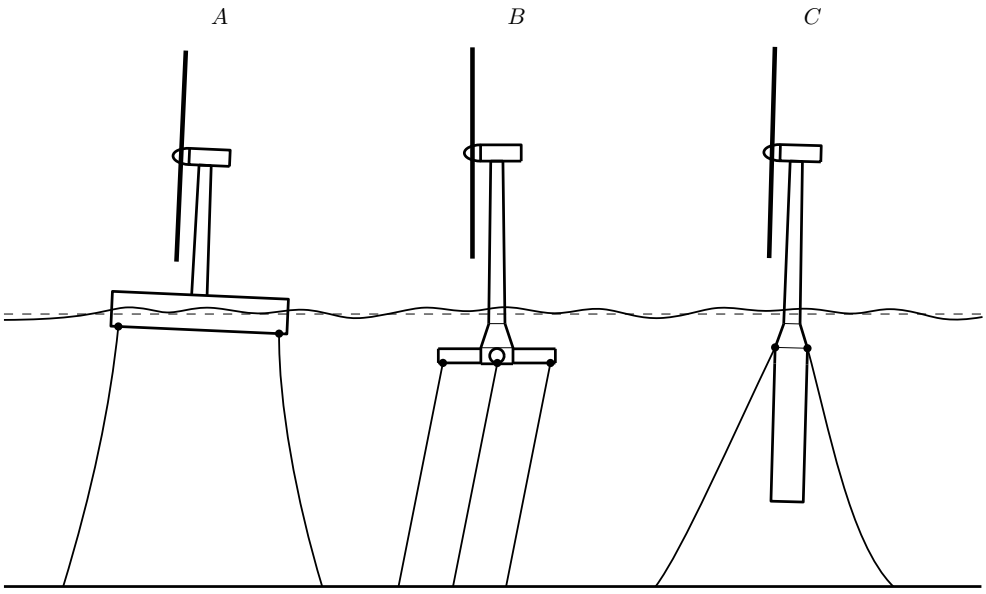

Figure 1.1.: Some concepts for floating foundations [2]. A: Barge platform, B: Tension Leg Platform, C: Spar-Buoy.

pitch and were seen to occur when the wind turbine was operating at high wind speeds where pitch control was active.

Above a certain wind speed, the available wind energy exceeds the maximum generating capability of the turbine and pitch control is applied to limit the uptake of wind power. The resonances were thus seen to stem from an unfortunate interaction between a power-limiting pitch control and a floating foundation. Specifically, pitch control was seen to induce negative damping in surge and pitch[1] for the floating platform. The resonance phenomena was thus linked to the naïve application of a pitch-controller designed for land-based turbines to a floating turbine.

The authors of this first report managed to counteract the resonances using feedforward from the platform pitch with validation from both experiment and simulation. Following Nielsen et al. [4], several subsequent papers addressed the resonance problem and proposed improved control strategies.

In [5] the pitch controller was intentionally made slower to limit interaction with the floating foundation. This was done by placing the regulator bandwidth below the resonance frequencies of the system. The rigid body resonance frequencies of a floating wind turbine are placed well below the peak of the wave spectrum[2]. An inevitable consequence is natural frequencies of motion with rather long periods, a distinguishing feature of floating operation. Although this less aggressive control was somewhat successful in ameliorating the reso-

[1]The wind direction falls along the surge direction.
[2]This is done to limit wave-excited resonances.

Figure 1.2.: HYWIND is towed into place. Photo: Øyvind Hagen, Statoil.

nances, the controller was no longer able to satisfactorily govern the rotor speed, nor was it able to provide adequate power quality.

In [6] a variety of methods were levied on the resonance problem, including a tower acceleration feedback, pitch-to-stall operation as well as controller "de-tuning"[3]. None of the applied methods provided truly satisfactory performance.

Linear multivariable control techniques have been successfully applied to the problem of dampening the resonances and a benchmark exercise may be found in Namik and Stol [7]. These authors subsequently derived methods for individual pitch control in [8].

Recent work has shown that more complex controllers do not necessarily yield the best performance. Indeed, in [9, 10] a simple algorithm referred to as *variable power collective pitch control* achieved good overall performance based on simple heuristic arguments.

The most sophisticated methodology to appear so far is perhaps the nonlinear model predictive controller appearing in Schlipf et al. [11]. While effective, the approach requires significant computational resources and does not seem readily applicable in todays turbine systems.

One of the most interesting documents related to the instability phenomena is the patent described in Skaare and Nielsen [12]. Here, a simple control system injecting damping through an augmented angular velocity reference is described. One may speculate that the methodology described therein has been a key factor in the successful testing of HYWIND. This method will be examined closely in Chapter 5.

[3]This notion implies a reduction of controller bandwidth.

1.2. Motivating example

A simple explanation for the control-induced resonance problem can be furnished by an argument from conservation of energy. The wind turbine rotor is equipped with a rotational kinetic energy described by

$$\mathcal{K}(\Omega) \triangleq J\Omega^2/2 \tag{1.1}$$

The rate of change of this internal energy is equal to the difference between the absorbed wind power P and the power dissipated in the generator[4] $E = Q_E\Omega$, viz.

$$\dot{\mathcal{K}} = P - E \tag{1.2}$$

Under somewhat idealized conditions, the absorbed wind power will assume the form

$$P = F(w_{\text{air}} - \dot{x}) \tag{1.3}$$

Here F represents the backwards thrust and $w \triangleq w_{\text{air}} - \dot{x}$ the relative flux though the rotor disk. This is a simple statement of power (P) being equal to effort (F) times flow ($w_{\text{air}} - \dot{x}$). An energy balance can now be used to model the dynamics of the rotor as

$$J\Omega\dot{\Omega} + E \approx F(w_{\text{air}} - \dot{x}) \tag{1.4}$$

The chief utility of this equation is that it connects the force to the angular velocity and power production whilst sidestepping most of the complexities of the aerodynamics. Note that the force F and airflow w_{air} can always be assumed to be positive for wind engineering applications. Be aware that the energy balance used above is only an approximation, it will be shown that dissipation mechanisms absent from (1.4) play a small but non-negligible role.

As will now be demonstrated, (1.4) is capable of recreating the resonance phenomena. Existing research suggests that two conditions must be met for the control-induced resonance phenomena to materialize. The conditions and their implications for (1.4) are itemized below.

1. The angular velocity is constant, or nearly so. This implies that the kinetic energy satisfies $\dot{\mathcal{K}} \simeq 0$.

2. The electrical power extraction is constant, or nearly so. This implies that the electrical power satisfies $E \simeq E_0$ where E_0 is constant.

As mentioned above, the resonance phenomena materializes when pitch control is utilized. Pitch control is often used for setpoint regulation of the angular velocity Ω. The primary objective is to avoid overspeed and maintain steady operation at high wind speeds. Effective setpoint regulation implies that the

[4]The shaft torque Q_E accounts for heat losses and frictional dissipation in the gearbox. This means that $E > P_E$ where P_E represents the electrical power of the generator.

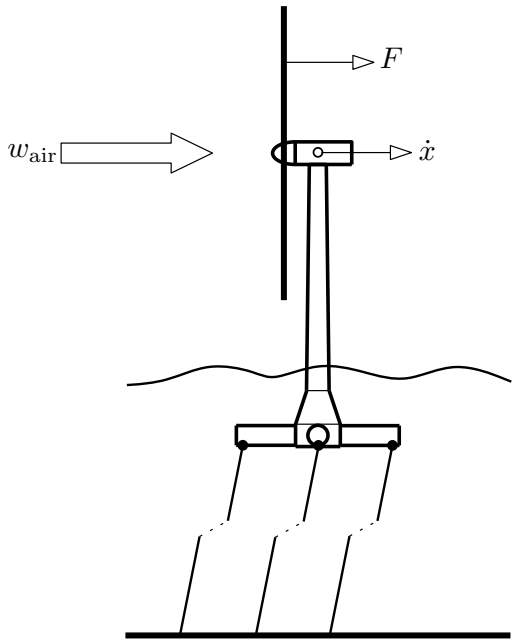

Figure 1.3.: First approximation of a floating wind turbine.

angular velocity remains in the vicinity of a constant reference for a well functioning control implementation, that is $\dot{\mathcal{K}} \simeq 0$. Whilst pitch is used to regulate the angular velocity, torque control is used to regulate the power. When the available wind power exceeds the capacity of the wind turbine generator, a typical control objective is to extract a nearly constant electrical power with little fluctuations. Essentially, this amounts to a control-induced power saturation. A consequence, again contingent on an effective implementation, is that the electrical power reduces to a constant $E \simeq E_0$.

It appears that the simultaneous control objectives of setpoint regulation and power saturation are the main culprits behind control-induced resonance. If the preceding reasoning is correct, an appropriate specialization of (1.4) capable of reproducing control-induced destabilization should read as

$$E_0 \approx F(w_{\text{air}} - \dot{x}) \tag{1.5}$$

Solving for the force yields the nonlinear model

$$F \approx \frac{E_0}{w_{\text{air}} - \dot{x}} = \frac{E_0}{w_{\text{air}}} + \frac{F}{w_{\text{air}}}\dot{x} \tag{1.6}$$

Inspection of (1.4) reveals that the pitch enters through the force F being absent elsewhere. The preceding equation therefore identifies the force generated by a pitch controller realizing perfect setpoint regulation.

The floating platform exemplified in Figure 1.3 can be modeled notionally as a driven harmonic oscillator

$$\ddot{x} + 2\zeta\omega_n\dot{x} + \omega_n^2 x = m^{-1}F \tag{1.7}$$

Here, m represents the effective inertia of the platform, ω_n the undamped natural frequency whereas ζ denotes the damping factor. Combining equations reveals the core of the problem; negative damping has been introduced through ill-designed automatic control.

$$\ddot{x} + \left(2\zeta\omega_n - \frac{F}{mw_{\text{air}}}\right)\dot{x} + \omega_n^2 x = \frac{E_0}{mw_{\text{air}}} \tag{1.8}$$

It is possible to extract more insight from the preceding equation. The steady-state displacement of the nacelle follows from the formula

$$\bar{x} = \frac{\bar{F}}{m\omega_n^2} \tag{1.9}$$

The bar symbol here indicates equilibrium values for the displacement and thrust. An approximate effective damping factor follows as

$$\zeta_{\text{eff}} = \zeta - \zeta_{\text{cid}}, \quad \zeta_{\text{cid}} = \frac{\bar{x}\omega_n}{2\bar{w}} \tag{1.10}$$

The destabilizing effect is seen to scale linearly with the resonance frequency and surge displacement, but inversely with the airspeed.

	First res. ω_n [rad s^{-1}]	Nacelle disp. $\bar{x}$ [m]	ζ_{cid}
Land	2.04	0.2	0.012
Spar	0.20	6.6	0.039
TLP	0.16	11.2	0.052

Table 1.1.: Control-induced destabilization of a representative 5 MW wind turbine [13] quantified by a negative damping factor. The table compares the effective negative damping associated with a fixed foundation, a spar buoy and a tension leg platform.

The damping factor due to control-induced destabilization ζ_{cid} is a dimensionless number. It can therefore be used to quantify how susceptible various platform designs are to the destabilization phenomena. Some rough estimates are given in Table 1.1 which shows the 1st resonance frequency ω_n (pitch for the spar platform, surge for the TLP) in nacelle displacement $\bar{x}$ at a wind speed of 17 m s^{-1} for a selection of platform designs. The numbers for the land-based design are found in [13]. The numbers for the floating designs are based on model tests found in Goupee et al. [14]. Floating support structures experience significant deflections in pitch, so the nacelle deflection is based on the formula $\bar{x} = \bar{X} + \bar{\theta}h$ where $\bar{X}$[m] describes surge at the free surface, $\bar{\theta}$[rad] the pitch and $h = 90$ m the nacelle height over the still water line (SWL). The wind speed

is used to estimate the flow rate $\bar{w}$. Based on these numbers it appears that floating wind turbines will suffer more from control-induced destabilization than their land-based counterparts. But, fixed-base wind turbines are also destabilized. The difference is that the negative damping is less likely to manifest itself as outright instability. It is interesting that ζ_{cid} is such a small number even for the floating designs. Control-induced destabilization is a subtle phenomena and the system's intrinsic damping must be low before concern is warranted.

1.3. A sketch solution

The energy-based methodology used in Section 1.2 to demonstrate the control-induced resonance problem can also be used to identify a solution. Sufficient conditions for destabilization were identified as a fixed kinetic energy $\dot{\mathcal{K}} = 0$ and a constant power extraction $E = E_0$. These conditions can be removed by permitting suitable variations in $\dot{\mathcal{K}}$ and E. A very simple way of doing this is to let the power vary as

$$E(\Omega) = \frac{\Omega}{\Omega_0} E(\Omega_0) \tag{1.11}$$

Here, Ω_0 is the desired setpoint for angular velocity. The wind turbine system can subsequently be forced onto a stable manifold given by

$$\dot{\mathcal{K}} + E(\Omega) - E(\Omega_0) + F\dot{x} = 0 \tag{1.12}$$

Returning to (1.4), one arrives at

$$E(\Omega_0) \approx F w_{\text{air}} \tag{1.13}$$

The force can now be extracted as

$$F = \frac{E(\Omega_0)}{w_{\text{air}}} \tag{1.14}$$

Comparison to (1.6) reveals that the destabilizing feedback from $\dot{x}$ is gone and the problem is apparently solved.

Chapter 5 will demonstrate that the preceding "solution" is correct in principle but that a higher feedforward from $\dot{x}$ is warranted due to the vortical wake discussed in Chapter 3. The idea presented here is but one way of avoiding control-induced destabilization. However, it appears that most existing methodology can be boiled down to different means of achieving variations in the kinetic energy and extracted power. Indirect methods such as controller detuning [6] achieves this by impairing the disturbance rejection in Ω so that $\dot{x}$ can propagate through to $\dot{\mathcal{K}}$. Direct methods such as the one found in the HYWIND patent [12] actively regulates Ω to achieve a result similar to (1.12). This will be demonstrated in Chapter 5.

1.4. Research agenda

Primary research questions

The research described in this work aims to answer the following primary questions. All addressing control-induced resonance and how to avoid it, even reverse it.

Question 1: *What are the necessary conditions for destabilization and what is the magnitude of the problem?* Answering this question will confine the scope of the problem and focus efforts where they are needed.

Question 2: *What is the efficacy of previously described solutions and how do they compare?* Answering this question will permit recommendations to be made about the best control strategy but also provide a benchmark for improved methods.

Question 3: *Can improved control strategies be found and described?* There is no reason to suppose that the optimal solution to control-induced resonance has been identified. Improved control strategies may extend the life-span of existing installations and/or improve power delivery. On a more speculative note, less conservative and hence less expensive platform designs could perhaps be considered with improved stabilization methods. The possibility of *reversing* the control-induced resonance phenomena through active damping injection is considered as part of this question.

Although the questions raised above are aimed primarily at floating designs, the numbers in Table 1.1 indicate that their resolution could have application to land-based designs as well.

Scope

In order to make headway, a number of simplifying assumptions and approximations will be made. The most central ones are itemized below.

Assumption 1: *The relative flow through the rotor plane is purely axial*[5]*.* This approximation neglects a variety of effects such as (1) rotor pitch and yaw offset with respect to the incoming wind, (2) wake swirl and (3) nonzero *rotor* pitch, yaw, sway, heave and roll rates. An itemized justification for these omissions is given below.

1. Pitch offset is small by design and can be expected to stay small enough to be negligible even for floating platforms. The yaw offset is actively sought removed by automatic nacelle control, hence negligible.

[5]The axis in question is given by the rotor's angular momentum vector.

2. Wake swirl describes the fluid's reaction to an applied torque and gives a rather small effect in modern wind turbines.
3. The neglect of rotor pitching is justified in Figure 1.4 where it is argued that the effects of platform pitch are well represented by an effective rotor surge motion. The dominant forcing F will take place normal to the rotor disk hence justifying omission of the remaining degrees of freedom.

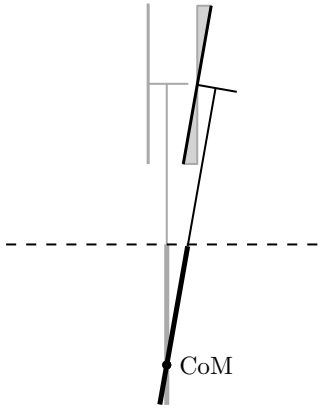

Figure 1.4.: Floating wind turbines can be expected to have a center of mass located well below the nacelle. The small shaded area on the right indicates that platform pitching is well approximated by a simple horizontal displacement of the rotor.

Assumption 2: *The rotor/drivetrain are inelastic.* Table 1.1 is based partially on results given in [13]. This report also describes frequencies associated with blade bending modes for the 5 MW wind turbine in question. The lowest frequency mode associated with blade deformation is the 1st asymmetric flapwise yaw and pitch at $\omega = 4.19\,\mathrm{rad\,s^{-1}}$. This is more than one order of magnitude higher than the platform modes described in Table 1.1 and suggests that blade elastics and the motion of the floating platform can be considered time-scale separated and hence amenable to individual treatment. The assumption of an inelastic drivetrain is more tenuous but adopted for reasons of simplicity.

Assumption 3: *The platform and tower's deformation/displacement are well described by linear elasticity theory and linear hydrodynamics.* Linear elasticity theory can be assumed to hold under the assumption of small structural motion. Linear hydrodynamics discards higher order wave loading and viscous drag and also misrepresents the forces induced by large amplitude motion. Nonlinear effects are important in the horizontal motion of moored structure and in severe sea states [15], both salient for floating wind turbines. However, a nonlinear description is too complicated in the present setting.

The assumptions and simplifications detailed above are extensive. This could lead to concern that the modeling will result in crude approximations and over-simplified representations. However, experimental validation and general predictive power will indicate that this is not so. The reader will find that the remaining physics are quite daunting in their own right.

The preceding list itemized simplifications used to facilitate the production of results. The nature of the results will also have a limited scope.

Limitation: *Small signal analysis.* The bulk of the analysis and the attendant results are based on first order perturbation analysis around steady equilibrium points.

1.5. Solution approach

The general approach used to resolve the primary research questions is briefly recounted below. It will be necessary to introduce novel models at some stages of the analysis. This gives rise to a set of *secondary research questions*. Some context is now given to motivate these problems while introducing key facets of the general solution strategy.

The energy balance (1.4) will serve as a cornerstone in the analysis undertaken below. After all, it led to an immediate solution of the resonance problem in Section 1.3, albeit in a conceptual form. But, the approximation given in (1.4) glossed over a number of conceptual difficulties.

- What constitutes the energy transfer mechanism converting the product $P = wF$ into $E = Q_E\Omega$?
- Are there other effects that contribute to the overall balance, such as dissipative mechanisms?
- Where does the blade pitch control enter the scene?
- The airflow w_{air} must necessarily be disturbed by the presence of the power-extracting wind turbine; what are the appropriate physics for this effect?

These fundamental questions must be resolved if the energy balance (1.4) is to be used. This is possible, and another cornerstone can be laid; flipping (1.4) on its head produces the formulae

$$F = \frac{J\Omega\dot{\Omega} + E}{w} \quad \Rightarrow \delta F = -\frac{\bar{F}}{\bar{w}}\delta w + \frac{J\bar{\Omega}\delta\dot{\Omega} + \delta E}{\bar{w}} \tag{1.15}$$

The first order perturbation shown on the right hand demonstrates that the energy balance can be construed as a dynamic system taking flow perturbations δw, changes in the angular velocity $\delta\Omega$ and generator power δE into a force

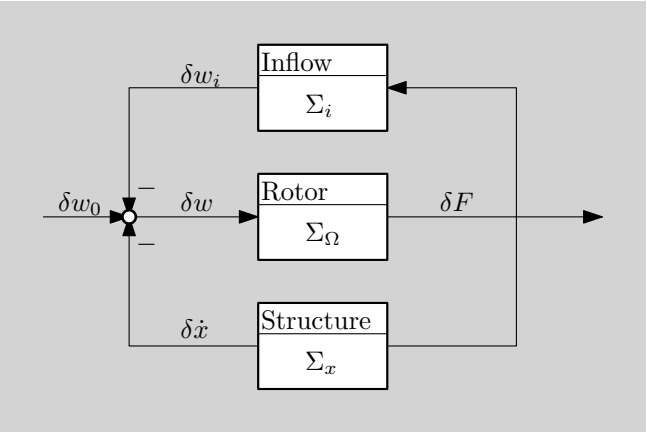

Figure 1.5.: The floating wind turbine as a feedback structure. Here Σ_Ω corresponds to the equations given in (1.15). The wind-speed w_0 serves as an exogenous input.

perturbation δF. The flow perturbation will be considered as the *input* while $\delta\Omega$ and δE are construed as the effect of internal dynamics. Interpreting δF as an *output* gives rise to the rotor subsystem illustrated in Figure 1.5. One can assume that the major contributor to platform motion is the thrust force. A hydroelastic module taking δF as input and generating a nacelle motion $\delta\dot{x}$ as output can thus be used to represent the platform mechanics. As will be shown, the disturbance in the airflow is well modeled by a dynamic system taking force perturbations into inflow perturbations δw_i. The emerging picture is shown in Figure 1.5.

The chief benefit of a modular model is that it permits abstraction from the underlying details. One can therefore redirect one's focus to properties of a more general nature. In stability analysis two such properties have acquired special significance, namely $\mathcal{L}_p$-gain and passivity. Interconnected plants, such as the one depicted in Figure 1.5, permits the use of these properties through the famous small-gain theorem and/or a suitable passivity theorem.

The motivating example in Section 1.2 suggests that the control-induced resonance phenomena arises due to unintended energy transfer (negative damping) into the platform system. In control theoretical parlance this implies a net positive supply rate over the terminals $(\delta\dot{x}, \delta F)$. Combining this insight with the feedback structure shown in Figure 1.5 suggests that a natural theoretical framework for studying the control-induced resonance problem is furnished by *passive systems* and its frequency domain counterpart of *positive real systems* [16]. Passivity theory can be used to make very general statements about interconnected systems subject to the properties of the constituent subsystems. While it is possible to conduct the analysis on a case-by-case basis using standard tools from linear control theory, the generality afforded by the passive interconnection theorems is very attractive.

Passivity based analysis of wind turbines is previously described in the literature. Monroy et al. [17] utilizes passivity tools to regulate the generator of a

wind turbine. Another example of a work focusing on the electrical subsystem is Fernández et al. [18]. In Valenciaga et al. [19] a passivity based algorithm was used to regulate wind power in a hybrid wind/solar generating system. A common denominator in these and other works is a reliance on coefficient models (see Chapter 2) for the aerodynamics and a focus on the electrical components of the wind turbine system.

Models with properties salient for passivity based analysis will be sought for each of the subsystems in Figure 1.5. This includes the aerodynamic theory which has not been treated in this manner before. Previously described theory can be used to describe the floating structure. It is well known that floating platforms may be modeled as passive systems, see e.g. Fossen [20]. In order to limit the scope of the thesis, the electrical subsystem will be described only notionally. However, the cited works indicate that this model component is compatible with the present approach.

With a suitable model at hand, passivity tools can be employed to propose control strategies for the floating wind turbine. A well developed theory facilitates this task, see e.g. Brogliato et al. [16], Khalil [21] and Van der Schaft [22].

Secondary research questions

Additional physics must be introduced in order to facilitate a passivity based analysis of the wind turbine system. The main questions that must be addressed are itemized below.

Question 4: *Can the platform subsystem taking force into nacelle motion be represented as a passive system?* Note that this question includes the impact of hydrodynamic forces.

Question 5: *How can the inflow w_i be modeled dynamically*[6] *and what are the passivity properties of the resulting system?* Answering this question will permit a passivity based examination of the full wind turbine system. New science will also result since the passivity properties of the inflow system does not seem to have been addressed in the literature. It should be noted that simplified wind turbine analysis usually relies on the quasistatic assumption, stipulating that the inflow w_i will arrive at its equilibrium value instantaneously, see e.g. Bianchi et al. [23]. A successful resolution of Question 5 will therefore allow an assessment of this ubiquitous assumption.

Question 6: *How can the energy balance be realized with an explicit parametric model?* Answering this question will permit quantitative analysis, including the positing of various physical bounds and equalities. This problem will turn out to be closely related to Question 5.

[6] A solution to the static modeling problem is well known.

Note that Question 5 has been addressed quite extensively in the literature where a broad variety of models can be found. However, existing methods do not seem suitable in the present setting. Simple model such as the acceleration potential methods in Van Bussel [24] or Peters and HaQuang [25] seem to under-predict the time-constants associated with the wind turbine inflow. On the other hand, more accurate models such as Øye's vortex model makes excellent predictions but is ill suited for analysis purposes. The new model presented here combines the benefits of the cited works whilst exhibiting clear passivity properties. It also dovetails nicely with other aspects of the new theory. Justification for these statements can be found in Chapter 3 and Chapter 4.

1.6. Outline with key results

An outline of the thesis is given by chapter below.

1 - Introduction

The introduction provides background on the problem of control-induced resonance in floating wind turbines. It is shown that the underlying physics are well captured by a simple energy balance. A tentative control strategy is proposed. The scene is set for the main thrust of the thesis; passivity based analysis of a turbine model in the guise of an interconnected structure.

Novel results

1. The energy balance $\dot{\mathcal{K}} + E = Fw$ is used to (1): identify conditions for the control-induced resonance phenomena and (2): demonstrate a new approach to the stabilization of floating wind turbines.

2 - Rudiments of Wind Engineering

This chapter introduces some basic concepts used in the modeling of wind turbines. The control task is described and some basic solutions are presented. Necessary background for Chapter 3 is also given. Limitations inherent in standard engineering models used for control design are discussed.

Contributions

Merz and Pedersen [26] provides an in-depth look at practical implementation of wind turbine control systems with a special emphasis on structural dynamics.

3 - Dynamic Vortex Theory

This chapter utilizes Joukowsky's rotor and the vectorial vortex lifting law to reduce the wind turbine's aerodynamic loading equations to a lossless *circulatory interconnection structure* shown below.

$$\begin{bmatrix} F_c \\ Q_c \end{bmatrix} = \frac{\rho A N}{2\pi} \begin{bmatrix} 0 & -\Gamma \\ \Gamma & 0 \end{bmatrix} \left(\begin{bmatrix} w_0 \\ 0 \end{bmatrix} - \begin{bmatrix} w_i \\ 0 \end{bmatrix} - \begin{bmatrix} \dot{x} \\ \Omega \end{bmatrix} \right)$$

The inflow generated by the wake is treated in a dynamic setting by combining concepts from classical hydrodynamics (vortex rings) and signals analysis (impulse response). It is shown that the theory reduces exactly to Rankine-Froude momentum theory at steady state. Analogues are also struck with other rotor theories. A reduced time is introduced to permit a frequency domain analysis of the inflow dynamics. The underlying physics in Øye's vortex model are given a firm theoretical basis. Frequency domain identification is utilized to derive a state space representation of the vortical wake. A first order model is derived as a low frequency limit of the general theory and compared to existing models of similar structure. Secondary research question 5 is resolved in this chapter.

Novel results

1. The feedback structure inherent in vortex based rotor models is uncovered.
2. A new analytical dynamic inflow model is derived based on conservation of momentum and vortex ring considerations.
3. A central, but hitherto unknown object referred to as the wake admittance $\mathcal{Q}$ is uncovered and interpreted.
4. The passivity properties of the inflow model are established.
5. A high fidelity lumped nonlinear state-space realization is proposed and validated against the exact model.
6. An exact low frequency limit of the general theory is derived and given the form of a first order nonlinear ODE.

Contributions

Pedersen [27] describes the theoretical basis and key results in this chapter.

4 - Engineering model

This chapter serves to connect the idealized DVT model of Chapter 3 with practical applications. Drag and tip loss corrections are introduced to represent dissipative effects. The $\Gamma\Delta$-parametrization of the wind turbine loading equations is presented. This method permits existing table data to be converted for

use in the vortex-theoretical paradigm. An equivalent airfoil method is used to compress two-dimensional table data into one-dimensional curves with a clear physical interpretation. Interestingly, wind turbines are shown to be equipped with a region of linear lift as well as global stall limits. The results in Chapter 3 and Chapter 4 are validated against experimental data from the Tjæreborg wind turbine. Finally, simplifications are made that result in a nonlinear parametric rotor model with only two tuning parameters. This model is validated against results from a BEMT[7] engineering code. Secondary research question 6 is resolved in this chapter.

Novel results

1. A new $\Gamma\Delta$-parametrization is proposed that can condense two dimensional coefficient data into equivalent one dimensional lift and drag curves.

2. A nonlinear parametric rotor model is derived. The model is shown to be capable of representing VPVS[8] wind turbines over the full operational envelope.

Contributions

Pedersen and Fossen [28] describes many of the key ideas presented in this chapter. However, the paper also illustrates how the methodology can be extended to six degrees of platform motion.

5 - System Analysis

The models developed in the thesis are gathered in the form of a feedback structure and a passivity based stability analysis is conducted. The stability of wind turbines in open-loop[9] is given a general characterization using properties of the parametric model of Chapter 4. An indirect analysis utilizing concepts from classical control theory is used to examine closed-loop dynamics. The inevitable destabilization associated with feedback control using pitch actuation is demonstrated and discussed. A simulation case study is furnished to illustrate predictions of the theory. By virtue of the model, a simple fix for existing control algorithms can be proposed in the form of an *energy shaping* reference signal. This control law reverses control-induced destabilization for any wind turbine satisfying the underlying approximations and simplifications in the feedback model. The soundness of the new method is demonstrated through a case study of a large wind turbine mounted on a floating platform. Comparisons are made to other methods appearing in the literature. Research questions 1-3 find their resolution in this chapter.

[7]Blade element momentum theory.
[8]Variable speed, variable pitch
[9]Implying the absence of collective blade pitch control.

Novel results

1. A wind turbine is analyzed as a feedback structure using passive systems theory.
2. Open loop stability is demonstrated for VPVS wind turbines mounted on elastic support structures.
3. The control-induced resonance problem is identified as an inevitable consequence of setpoint regulation using collective pitch actuation.
4. An energy shaping control algorithm is proposed that reverses the control-induced resonance phenomena.

6 - Conclusions

A - Hydroelastic model

This chapter employs the hydrodynamic analysis in Damaren [29] along with a structural model based on classical mechanics to show that a linear hydroelastic model of the floating platform can be expected to obey passivity. Secondary research question 4 is resolved in this chapter.

1.7. Symbols and Conventions

Symbol	Units	Description
x	m	Nacelle (tower top) horizontal displacement
F	N	Aerodynamic thrust force
Q	N m	Aerodynamic torque
P	W	Aerodynamic shaft power ($\Omega Q = P$)
Ω	rad s^{-1}	Angular velocity of the rotor
$\mathcal{K}$	J	Kinetic energy of the rotor
Q_E	N m	Generator shaft torque ($\Omega Q_E = E$)
E	W	Generator shaft power
w_0	m s^{-1}	Wind speed
w_i	m s^{-1}	Inflow
w	m s^{-1}	Relative axial flux ($w = w_0 - w_i - \dot{x}$)
w_{air}	m s^{-1}	Airflow ($w = w_0 - w_i$)
J	kg m^2	Rotor moment of inertia
Γ	m^2 s^{-1}	Circulation
Δ	m s^{-1}	Dissipation factor
ρ	kg m^{-3}	Air density
N		Number of blades
R	m	Rotor radius
ℓ	m	Length scale ($2BR/3$)
A	m^2	Swept area ($A = \pi R^2$)
p	kg m^{-1} s^{-2}	pressure
L	N	Airfoil lift
D	D	Airfoil drag
a		Inflow factor (w_i/w_0)
λ		Tip speed ratio ($\Omega R/w_0$)
C_T		Thrust coefficient
C_Q		Torque coefficient
C_P		Power coefficient
B		Tip loss factor
J_n		Bessel function of the first kind
$\mathcal{Q}$		Wake admittance
s		Laplace variable
σ		Reduced Laplace variable
μ		Inertia coefficient
β	rad	Collective pitch angle
u	rad	Bias corrected pitch input ($\beta - \beta_*$)
V	m s^{-1}	Onset flow
α	rad	Angle of incidence
ϕ	rad	Inflow angle

Some frequently used monikers are given below.

$()_*$	Point of optimal power extraction
$()^+$	Upper limit
$()^-$	Lower limit
$()_p$	Tip loss corrected
$\bar{()}$	Equilibrium point
$\delta()$	Perturbation

For matrices, the following symbols will be utilized

$\boldsymbol{M} \succ 0$	Positive definite
$\boldsymbol{M} \succeq 0$	Positive semidefinite

Averaging convention The relative flow w is used in an averaged sense. Nominally, the aerodynamic flux through the rotor is spatially nonuniform. Let the underlying axial flux through the rotor be decomposed as

$$\hat{w}(r, \theta, t) = w(t) + \tilde{w}(r, \theta, t) \tag{1.16}$$

Here, the term $\tilde{w}(r, \theta, t)$ absorbs variations across the blade radius r and azimuthal angle θ. The averaged flow used in the model is defined as a weighed integral taken over the blade radii of the turbine blades. Let the i'th blade be located at the azimuthal angle $\theta(t) = \theta_i(t)$. For N blades, the following convention applies.

Definition 1.1 (Averaged flux)**.**

$$w(t) \triangleq \frac{1}{AN} \sum_i^N \int_0^R \hat{w}(r, \theta_i, t)\ 2\pi r dr \tag{1.17}$$

An immediate corollary is that the perturbation term satisfies

$$0 = \frac{1}{AN} \sum_i^N \int_0^R \tilde{w}(r, \theta_i, t)\ 2\pi r dr \tag{1.18}$$

This notational convention will also be used for other distributed quantities such as pressure and the axial blade/platform deformation.

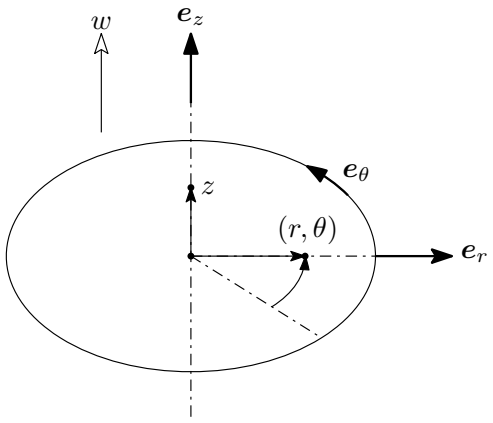

Figure 1.6.: Cylindrical coordinate system. The notion of "axial" is a shorthand for *parallel to* $\boldsymbol{e}_z$.

2. Rudiments of Wind Engineering

This chapter serves the dual purpose of introducing the basic theory of wind turbine aerodynamics whilst furnishing some important relations to be used in the following chapters. Analysis tools such as Rankine-Froude Momentum theory are recounted with an eye to developments in Chapter 3. Modeling practice in wind engineering is discussed. A brief exposition of wind turbine control systems is also given.

2.1. Introduction

Wind turbines are devices designed to convert the linear momentum of the wind into a shaft torque so that power may be extracted via a generator. The aerodynamic theory of wind turbines is customarily divided into two problems.

The inner problem details the aerodynamic force production over the blades subject to the relative flow impinging on the foil sections.

The outer problem examines how the ambient flow reacts to the applied loading in the form of a modification to the relative flow.

In keeping with wind engineering conventions, let the *inflow* enter the airflow as a negative feedback, viz.

$$\hat{w}_{\text{air}}(r,\theta,t) = \hat{w}_0(r,\theta,t) - \hat{w}_i(r,\theta,t) \tag{2.1}$$

Here, $\hat{w}_i$ denotes the inflow whereas $\hat{w}_0$ denotes the wind speed. The hat signifies that distributed fields are considered, see Section 1.7 for details on the notational convention.

The inner problem is usually treated using Prandtl's lifting line approximation, permitting each section along the span to be treated in isolation with a two-dimensional foil model. The outer problem is typically solved with momentum theory or vortex theory, even CFD sees application.

2.2. The wind resource

The wind field exhibits significant spatial and temporal variability. An idea of the temporal variability can be gleaned from Figure 2.1 which shows the

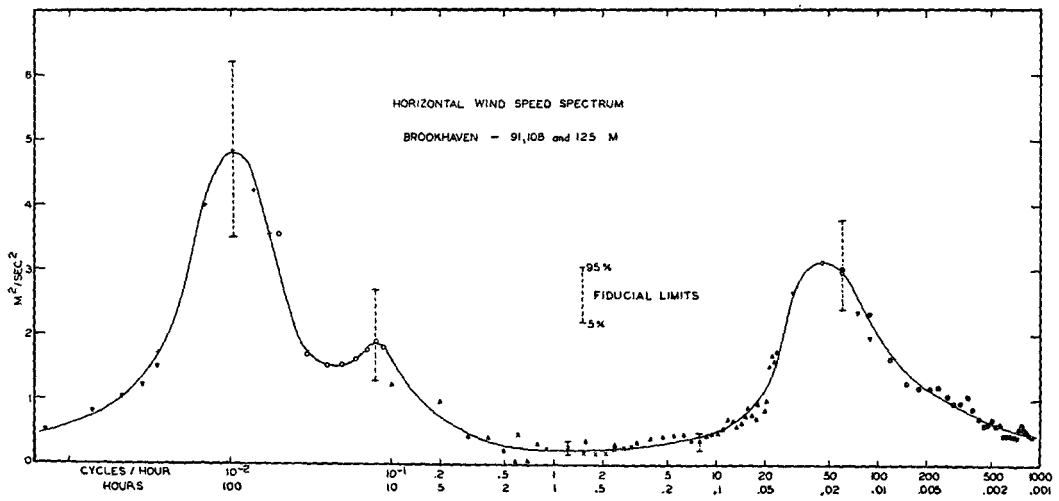

Figure 2.1.: A power spectrum of the horizontal wind speed measured at Brookhaven National Laboratory at about 100m. Facsimile from Van der Hoven [30].

power spectrum of the wind speed garnered from measurements at Brookhaven National Laboratory.

The peak at low frequencies is the so-called synoptic peak associated with long-term variations in the weather systems. (This peak is located at a period of about 4 days). Diurnal variations give rise to the second peak in the curve. A band-gap is evident at variations with hourly periods and is followed by the last *turbulent* peak. The gap separating the diurnal and turbulent peaks means that one can construe the wind speed as the superposition of a slowly varying component w_0^{mean} and an additive turbulent component w_0^{turb}. On time-scales salient for automatic control and simulation it is permissible to write

$$w_0(t) = w_0^{\text{mean}} + w_0^{\text{turb}}(t)$$

Note that the preceding equation describes an averaged flux defined in accordance with (1.17).

There are a multitude of models aimed at describing the turbulent power spectrum, see e.g. Burton et al. [31]. Assuming a point measurement, the von Karman Spectrum is often recommended [32]. This spectrum may be represented by shaped white noise $v(t)$, as done in Welfonder et al. [33]. Spectral factorization gives the representation shown below.

$$\mathcal{S}_K(\omega) = G(\jmath\omega)G(-\jmath\omega)\mathcal{S}_v(\omega), \quad G(\jmath\omega) = \frac{\sigma\sqrt{\frac{0.475L}{w_0^{\text{mean}}}}}{\left(1+\frac{\jmath\omega L}{w_0^{\text{mean}}}\right)^{5/6}} \tag{2.2}$$

Here, σ is the turbulence intensity and L is the length scale. Realization of the fractional filter $G(s)$ allows realistic time-domain simulations of the turbulent

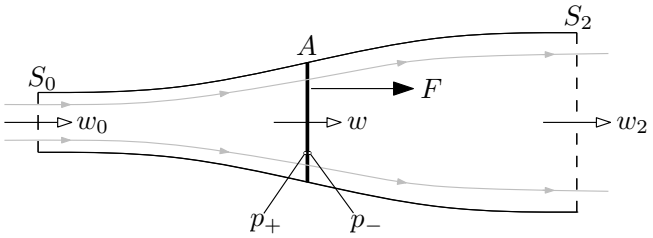

Figure 2.2.: The wind turbine's slipstream.

wind speed given appropriate constants.

$$w_0(t) = w_0^{\text{mean}} + \int_0^t g(t-\tau)v(\tau)\ d\tau, \quad g(t) = \mathcal{L}^{-1}\{G(s)\} \tag{2.3}$$

The von Karman model provides reasonable accuracy at frequencies well below the rotational frequency of the turbine when construed as a description of the *effective* wind speed [32]. At higher frequencies, the blades sample the spatially nonuniform wind field which gives rise to periodic peaks [34]. Rotational sampling requires a significantly more elaborate model and falls beyond the scope of this thesis. One must however be cognizant of this phenomena when designing control algorithms.

2.3. Rankine-Froude theory

Figure 2.2 shows the modeling setup used to derive Rankine-Froude momentum theory [35], a ubiquitous tool in the analysis of the *outer problem*. Rankine-Froude theory is based on two important ideas. The first is that of the *actuator disk* which abstracts the details of the rotor's blade loading into a pressure jump Δp over a permeable disk. This pressure jump is often modeled as constant at a given radial station, implying that the azimuthally discontinuous loading imparted by a finite number of blades is to be treated in an averaged sense. The second key idea is the *streamtube* which permits a control volume analysis to be undertaken. The streamtube divides the flow field into an outer ambient part and an inner slipstream which is perturbed when a loading is imparted at the actuator disk.

A simple variety of momentum theory is now derived using elementary tools. In keeping with the assumptions of momentum theory, the distributed flow-field assumes the following form

$$\hat{w}(r) = w + \tilde{w}(r) \tag{2.4}$$

That is, the problem assumes azimuthal symmetry and steadiness. Furthermore, nonuniformities in the wind speed are neglected so that $\hat{w}_0(r) = w_0$. Finally, rotor motion is neglected implying that $\hat{w}(r) = \hat{w}_{\text{air}}(r)$. The aim is to identify

the averaged inflow w_i at the disk given a uniformly applied thrust F. It turns out that an assumption of optimal loading is useful in this quest.

The control volume admits a flux over three distinct surfaces. The first is located far upstream and is denoted by the subscript 0. Subscript 2 indicates a second control surface located far downstream. The rotor disk is placed between these two stations and is indicated by the subscript 1. This subscript will be suppressed to avoid clutter.

Some key relations are used to establish the theory. Bernoulli's theorem can be used to relate pressures between stations 0 and 1 and stations 1 and 2. Assuming that the pressure perturbation induced by the rotor decays quickly one has

$$\frac{1}{2}\rho w_0^2 = \frac{1}{2}\rho \hat{w}(r)^2 + q(r) + \hat{p}_+(r) \tag{2.5}$$

$$\frac{1}{2}\rho \hat{w}(r)^2 + \hat{q}(r) + \hat{p}_-(r) = \frac{1}{2}\rho \hat{w}_2(r)^2 \tag{2.6}$$

Here $\hat{p}_+(r)$ and $\hat{p}_-(r)$ denote the pressures at the front and back faces of the rotor, respectively. The dynamic pressure associated with non-axial flow at the rotor is denoted by $\hat{q}(r)$. Solving for the nonuniform pressure jump yields

$$\Delta\hat{p} \triangleq \hat{p}_+ - \hat{p}_- = \frac{1}{2}\rho(w_0 - \hat{w}_2)(w_0 + \hat{w}_2) \tag{2.7}$$

Invoking conservation of mass furnishes the relation

$$\rho S_0 w_0 = \rho A w = \rho S_2 w_2 \tag{2.8}$$

Furthermore, conservation of momentum can be used to yield the equality

$$\rho \int_{S_0} w_0^2 \, dS - \rho \int_{S_2} \hat{w}_2^2 \, dS = \int_A \Delta\hat{p} \, dS = F \tag{2.9}$$

Combining the two conservation laws gives rise to the following relation.

$$F = \int_{S_2} w_2 w_0 - \hat{w}_2^2 \, dS = \rho A w(w_0 - w_2) - \rho \int_{S_2} \tilde{w}_2^2 \, dS \tag{2.10}$$

Optimality now enters the picture and an argument from Johnson [36] is invoked. The energy balance in the control volume reads as

$$\begin{aligned} P = \frac{1}{2}\rho \int_{S_0} w_0^3 \, dS - \frac{1}{2}\rho \int_{S_2} \hat{w}_2^3 \, dS &= \frac{1}{2}\rho \int_{S_2} w_2 w_0^2 - \hat{w}_2^3 \, dS \\ &= \frac{1}{2}\rho S_2 (w_0 - \hat{w}_2)(w_0 + \hat{w}_2) w_2 - \frac{1}{2}\rho \int_{S_2} (3w_2 - \tilde{w}_2)\tilde{w}_2^2 \, dS \end{aligned} \tag{2.11}$$

It is seen that the aerodynamic power P is maximized when the far wake flow perturbation is uniform, i.e. $\tilde{w}_2 = 0$. Proceeding with an assumption of optimality implies a uniform far wake flow perturbation $\hat{w}_2 = w_2$. From (2.7) it is

seen that this also implies a uniform pressure jump so that $\Delta\hat{p} = \Delta p$. The net force $F = A\Delta p$ follows from (2.7) or (2.10) as either

$$F = \frac{1}{2}\rho A(w_0 - w_2)(w_0 + w_2) = \rho A w(w_0 - w_2) \tag{2.12}$$

The last equality identifies the averaged flow at the rotor w as an average of the flow at the upstream and downstream stations.

$$w = \frac{1}{2}(w_0 + w_2) \tag{2.13}$$

Gathering results and recalling that $w = w_0 - w_i$ produces a solution to the outer problem in the form of the static inflow model

$$F = 2\rho A w w_i \tag{2.14}$$

The aerodynamic power follows from

$$P = F(w_0 - w_i) \tag{2.15}$$

It is possible to elaborate on the preceding analysis by considering pressures acting on the sides of the slip-stream but this does not affect the result [37]. While it is tempting to assume that the inflow at the disk is constant with $\hat{w}_i(r) = w_i$ this is not the case [38]. Distributed momentum theory, a key ingredient in BEMT[1], replicates the preceding analysis but now over concentric annular streamtubes permitting a distributed inflow to be obtained. However, as shown in [38] this approach fails to accurately describe the inflow distribution under heavy load whereas the simple model developed above holds true subject to the assumption of optimality.

High loading

It is important to note that Rankine-Froude momentum theory has a limited region of validity. This is most readily seen by computing the far wake radius which follows from conservation of mass.

$$R_2 = R\sqrt{\frac{w_0 - w_i}{w_0 - 2w_i}} \tag{2.16}$$

The model clearly ceases to be valid for inflows $w_i \geq w_0/2$ where the streamtube acquires a radius R_2 which is no longer meaningful. This situation occurs at very high thrust loadings satisfying[2]

$$F > \frac{1}{2}\rho A w_0^2 \tag{2.17}$$

When this bound is exceeded the flow through the rotor will reverse sign and the system will enter a so-called propeller brake state [41]. This situation is

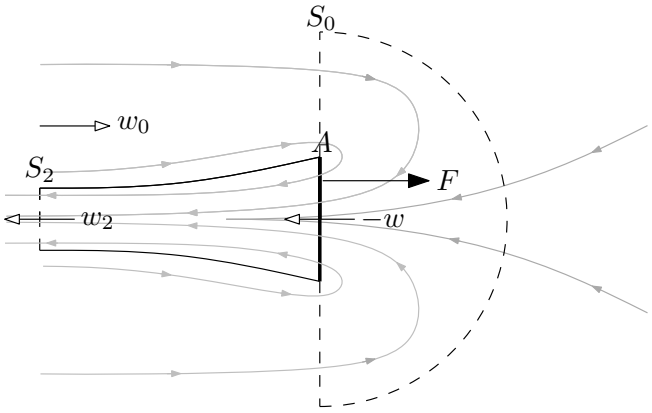

Figure 2.3.: The wind turbine's slipstream for over-unity thrust loadings.

depicted in Figure 2.3. The propeller brake state evidently requires a different control volume. Wilson and Lissaman [41] furnishes an appropriate extension of (2.14) as

Model 2.1 (Rankine-Froude inflow relation)**.**

$$F = 2\rho A|w|w_i \tag{2.18}$$

A pair of dimensionless numbers known respectively as the thrust coefficient and inflow factor are defined below.

$$C_T \triangleq \frac{F}{\frac{1}{2}\rho A w_0^2}, \quad a \triangleq \frac{w_i}{w_0} \tag{2.19}$$

Note that (2.17) corresponds to over-unity thrust coefficients. Using the dimensionless numbers (2.18) reduces to the simple form

$$C_T = 4|1 - a|a \tag{2.20}$$

Experiment indicates that Rankine-Froude momentum theory fails for high thrust loadings as evidenced by Figure 2.4. The failure of the theory at high loadings is due to the ambiguity imposed by the flow directions in the near and far wake when $1/2 < a < 1$. In this interval the near and far wake airflows have opposing directions rendering a control volume analysis tenuous. Practice reveals that over-unity thrust loadings also result in potentially unstable flows through the disk, not readily gleaned from the static inflow relations [36]. Fortunately, these problems are usually not relevant for the variable-speed variable-pitch wind turbines considered herein.

[1] Blade element momentum theory [39].

[2] With equality, this corresponds to the drag of an impermeable circular disk of radius A [40].

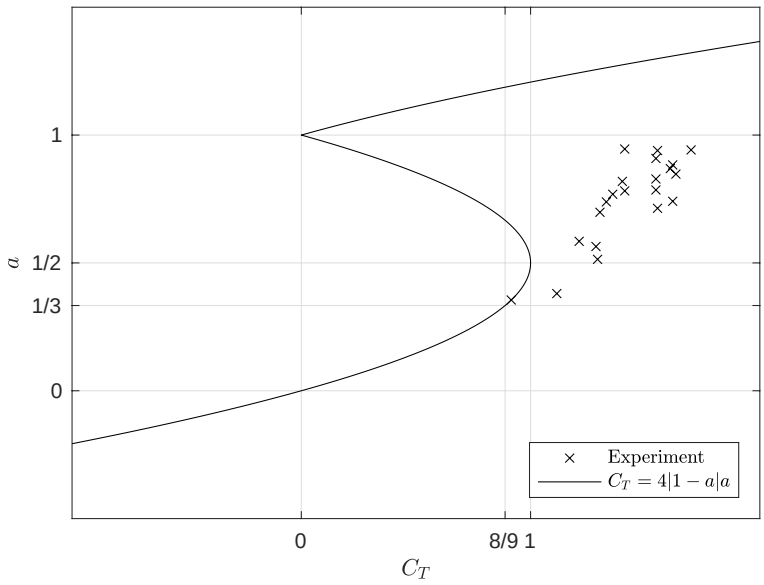

Figure 2.4.: Static inflow relation. Note the failure of the theory at high thrust coefficients. The point of optimal power extraction is located at $a^* = 1/3$ and $C_T^* = 8/9$ which is within the region of validity. Experimental data from Burton et al. [31].

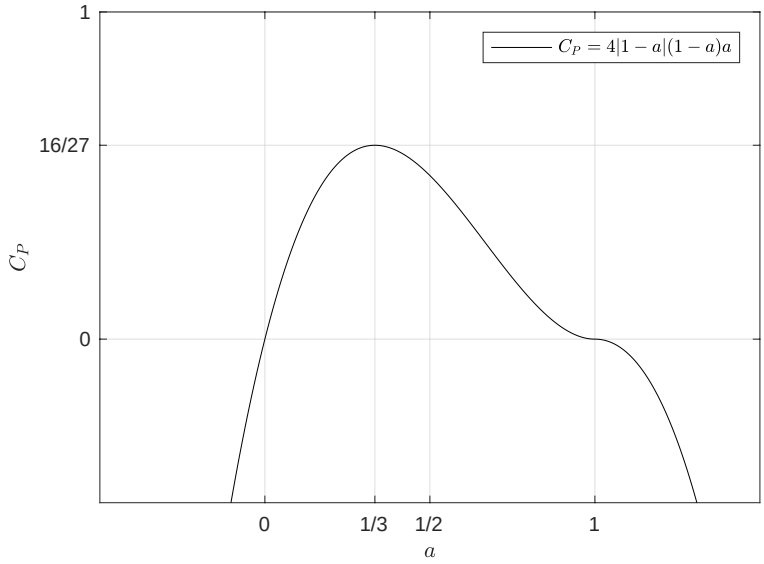

Figure 2.5.: The power coefficient. An optimum is found at $a^* = 1/3$ where the Betz-limit is realized as $C_P = 16/27$. Negative values of C_P corresponds to propellering where power is transferred to the fluid.

The section on Rankine-Froude theory is concluded with the definition of a power coefficient

$$C_P \triangleq \frac{P}{\frac{1}{2}\rho A w_0^3} = 4|1-a|(1-a)a \tag{2.21}$$

The optimal power for a given wind speed is found at the inflow $a^* = 1/3$ where

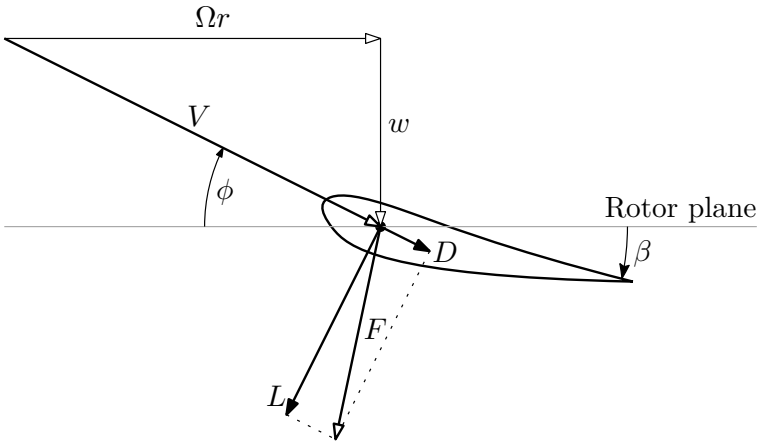

Figure 2.6.: Cross-section of the lifting line showing an airfoil section located at the radial station r producing lift L and drag D. A collective pitch β may be used to modify the blade's angle, in turn modifying the angle of incidence at the sectional foils.

$C_P = 16/27$. This is known as the Betz-limit. A well designed turbine will produce a thrust so that the inflow stabilizes around this value, i.e. $C_T = 8/9$. This also implies that a wind turbine can be assumed to remain in the well-defined region defined by $a < 1/2$ and $C_T < 1$. However, care must be exercised at the low wind speeds and high thrust coefficients associated with turbine startup, see Figure 5.6.

2.4. Blade element theory

The inner problem detailing the aerodynamic force production over the blades is often solved with blade element theory (BET). The N blades are modeled as lifting lines where it is assumed that each blade section along the span acts as a two dimensional airfoil. The three dimensional finite wing effects are captured by the inflow w_i. Figure 2.6 shows a diagram of a foil section at the radial station r. The inflow angle ϕ and onset velocity V are given by

$$\phi = \tan^{-1}\left(\frac{w}{\Omega r}\right), \quad V = \sqrt{w^2 + (\Omega r)^2} \tag{2.22}$$

Note that axial swirl is neglected here. This effect requires additional physics and gives rise to a small flow perturbation in the azimuthal direction.

Airfoil theory predicts the blade loads

$$L = \frac{1}{2}\rho c C_l(\alpha) V^2, \quad D = \frac{1}{2}\rho c C_d(\alpha) V^2 \tag{2.23}$$

where C_l and C_d are the foil section's lift and drag coefficients. The angle of incidence is found from

$$\alpha = \phi - \beta - \theta \tag{2.24}$$

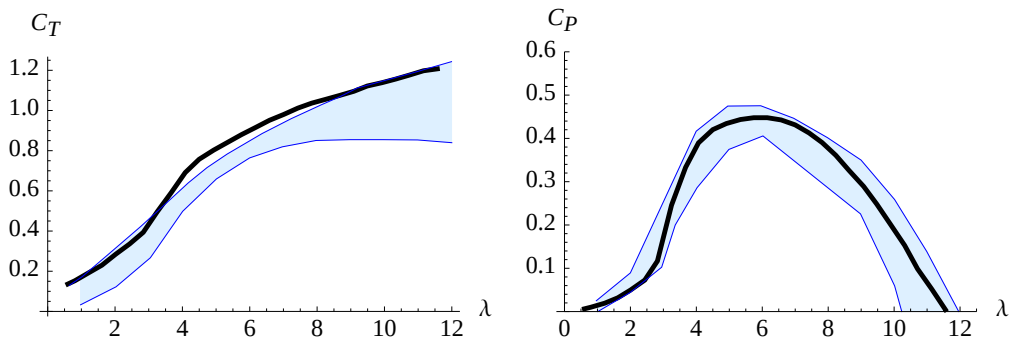

Figure 2.7.: Experimental and simulated thrust and power coefficients from a blind study performed by Krogstad and Eriksen [42]. The shaded region indicates the range of predictions, discarding outliers.

Here θ describes the blade twist and β denotes the collective pitch deflection. The differential thrust and torque on a blade can then be given by

$$dT = (L\cos(\phi) + D\sin(\phi))\ dr \tag{2.25a}$$

$$dQ = (L\sin(\phi) - D\cos(\phi))\ rdr \tag{2.25b}$$

Solving (2.25) subject to (2.23) in combination with a distributed form of momentum theory (2.14) allows the loads on the turbine to be identified for a given wind speed w_0, angular velocity Ω and pitch angle β. This procedure constitutes blade element momentum theory (BEMT) and gives rise to models on the form shown below in (2.26). Note that the distributed inflow $\hat{w}_i$ must be found in the process of determining the loads, all other variables being given. Being a dependent variable, the inflow is absorbed into the final loading expression. The model developed in Chapter 3 will extricate the inflow from the load, necessary in the transient setting.

2.5. Modeling practice

The dynamics of a wind turbine are highly complex and involves aerodynamics, structural mechanics, electromechanics as well as other disciplines. If floating designs are considered, one must also contend with hydrodynamics. It is important to note that there is not one "correct" way of modeling a wind turbine. Blind test studies have on several occasions revealed the shortcomings of a variety of distinct aerodynamic models [42, 43]. Wind turbine aerodynamics are very complex and the best one can hope for is a good approximation to the true physics. Figure 2.7 gives a good idea of the achievable performance.

Detailed analysis is customarily done with numerical engineering tools such as FAST [44] or HAWC2 [45]. Such models usually apply the blade element momentum theory (BEMT) to obtain aerodynamic forces and moments. The BEMT used in these codes is in essence similar to the theory described above.

The forces may subsequently be coupled to a structural and electromechanical model. Numerical engineering models often have tens or hundreds of states and employ complex numerical routines. As such, these tools are essentially "black boxes" which are difficult to utilize for model based control or in cases where an analytical model is desired. Some of these tools may output a linearized dynamic model. But, wind turbine dynamics are nonlinear and several locally linear models may be required to cover the operational envelope.

A pragmatic and very prevalent approach in control development is to express the steady power, thrust and torque in coefficient form

$$P = \frac{1}{2}\rho A C_P(\lambda, \beta) w_0^3 \tag{2.26a}$$

$$F = \frac{1}{2}\rho A C_T(\lambda, \beta) w_0^2 \tag{2.26b}$$

$$Q = \frac{1}{2}\rho A R C_Q(\lambda, \beta) w_0^2 \tag{2.26c}$$

These expressions all consist of a dimensional scaling given in terms of the air density $\rho[\mathrm{kg\,m^{-3}}]$, swept area $A[\mathrm{m^2}]$ and averaged wind speed $w_0[\mathrm{m/s}]$ multiplied by a dimensionless coefficient. The power, thrust and torque coefficients (C_P, C_T, C_Q) depend on the collective pitch deflection β and the dimensionless tip speed ratio (TSR) defined below.

Definition 2.1 (Tip speed ratio)**.**

$$\lambda \triangleq \frac{\Omega R}{w_0} \tag{2.27}$$

Even though the coefficient models strictly speaking only apply to steady operation, they are often used as quasistatic approximations in dynamic models. The dimensionless coefficients can be obtained as table-data from a BEMT-based wind turbine performance tool such as Aerodyn [46] or WT-perf [47]. Coefficient models may be used in the form of a numerical lookup table or one may derive a curve-fit to the tables for easier analysis. See Figure 2.8 for a graphical representation of such table-data.

The coefficient form of turbine forces given in (2.26) is quite convenient. Due to their prevalence it appears prudent to justify why this format is *not* used in the thesis. Coefficient models are encumbered by certain drawbacks when applying control theory and some of these are itemized below.

1. The aerodynamics of a wind turbine are not steady and exhibit significant dynamics on timescales relevant for automatic control.

2. The tables treat thrust and torque separately while they are in fact highly coupled.

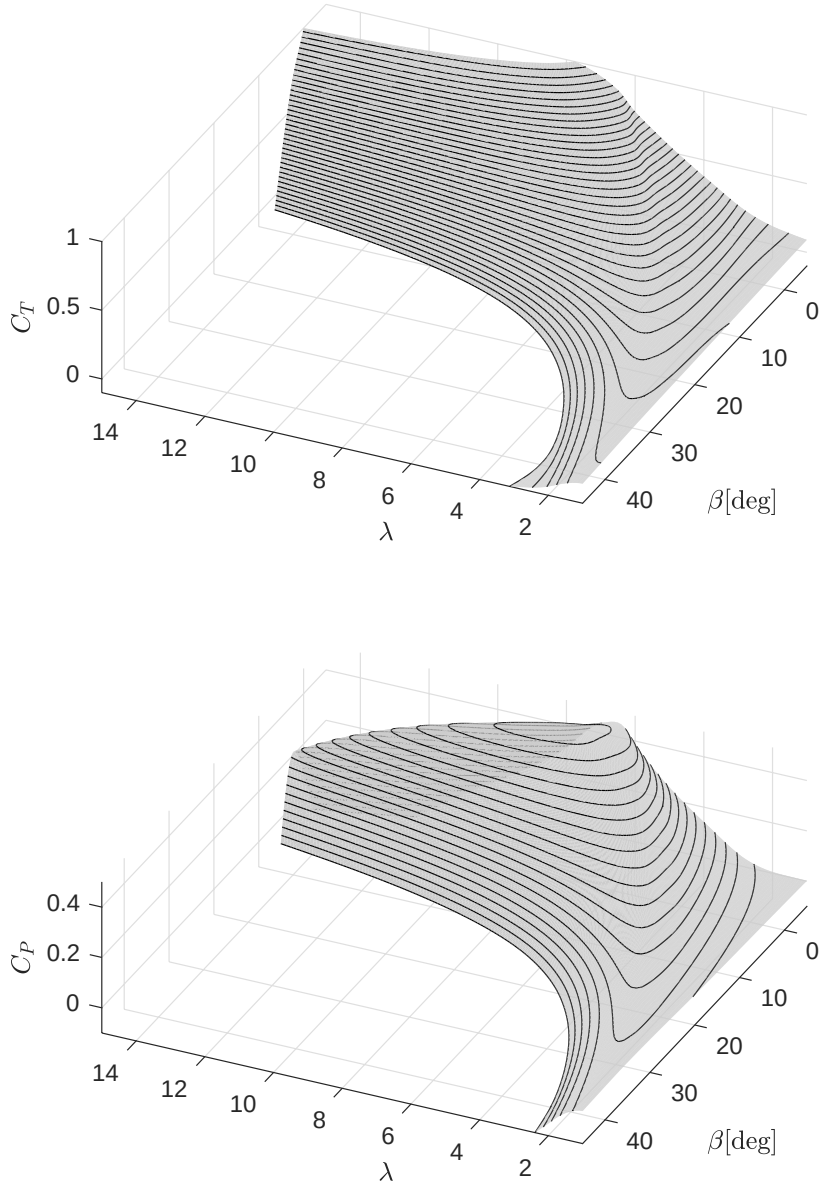

Figure 2.8.: Power and thrust coefficients for a pitch controlled wind turbine. The specific turbine shown in the plot is a 5 MW variable-speed variable-pitch type representative of modern machines [13]. The power coefficient C_P is tacitly assumed to have a unique optimum, verified in this example.

3. Coefficient data obscure the physics and uncertainties inherent in the aerodynamic model used to produce them. As such, they inherit the black-box nature of their origin.

4. Additional arguments to the coefficients are not practical as this would require tables of dimension larger than two. Advanced actuator systems such as individual pitch are difficult to model in terms of coefficient tables.

The model developed in the following chapters finds much of its utility in extricating the various physical phenomena from each other. This facilitates incorporation of dynamic effects and other generalizations.

2.6. Automatic control

The ultimate purpose of a wind turbine is to convert aerodynamic power into electrical power, preferable in the most effective manner possible. Automatic control can facilitate this objective by regulating the blade pitch and/or the regulator torque. Not all wind-turbines use pitch control and not all wind turbines permit variations in the angular velocity. Broadly speaking, variable speed operation permits better power absorption at low to intermediate wind speeds. Variable pitch is used to limit the power absorption at high wind speeds. A brief taxonomy is given below.

FSFP (Fixed speed, fixed pitch): This type of wind turbine is usually based around a synchronous generator turning at a speed nearly proportional to the line frequency. A linearized generator torque characteristic can be given as [23]

$$Q_E(\Omega) = k_g(\Omega - \Omega_s) \tag{2.28}$$

Here k_g is a large constant and Ω_s denotes the synchronous speed. The absence of pitch regulation forces the designer to rely on passive stall regulation to avoid overload. While this design is robust and simple, the increased loads and reduced power capture has rendered the FSFP type unattractive for large utility grade wind turbines.

FSVP (Fixed speed, variable pitch): Here, pitch control is used to improve upon the passive power limiting used in FSFP designs. A key benefit is that the system can be dimensioned less conservatively due to reduced loads. An additional benefit for pitch to feather designs is more predictable behavior as a consequence of attached blade flow. Pitch to stall variations are also possible, but suffer from less predictable and higher thrust loads. Note that the power output of the FSVP type is not much higher than for the FSFP design [31].

VSVP (Variable speed, variable pitch): Variable speed operation allows the wind turbine to extract more power. As will be discussed below, an angular velocity proportional to the wind speed optimizes power extraction. Since the wind speed is variable, optimality requires a variable angular velocity. Other benefits include less acoustic noise at low wind speeds and a "flywheel" effect smoothing loads on the drivetrain [31]. Variable speed operation can be realized by more complex generator types which often require automatic control for their operation. Herein, it is assumed that

is is possible to directly realize a torque command $Q_E(t)$ given to the generator. Modern power electronics can be assumed fast enough to render this assumption tenable [23]. VPVS is the design most likely to serve in a floating installation and will therefore be the main focus herein.

2.6.1. Maximum power point tracking (MPPT)

The power coefficient of a well designed turbine is equipped with a unique optimum located at $\lambda = \lambda_*$ and $\beta = \beta_*$. The maximal power is thus extracted at $C_P^* = C_P(\lambda_*, \beta_*)$. See Figure 2.8.

One of the primary purposes of a control system is to facilitate optimal power extraction by placing β and λ at the optimal values. Evidently, a fixed pitch $\beta = \beta_*$ is suitable when tracking the point of maximum power. The tip-speed-ratio is a dynamic quantity $\lambda = \lambda(t)$ given by the angular velocity $\Omega(t)$, radius R and wind speed $w_0(t)$. While $w_0(t)$ is beyond the control of the engineer, $\Omega(t)$ can be manipulated in a variable-speed turbine through the use a generator capable of exerting a torque $Q_E(t)$ on the shaft. Ideally, the angular velocity should be directly proportional to the wind speed, viz.

$$\Omega = \frac{\lambda_*}{R} w_0 \tag{2.29}$$

The wind speed cannot be measured reliably motivating the use of an indirect method. Assuming steady operation so that the electrical and aerodynamic power are balanced, the model given in (2.26) applies.

$$\bar{E} = \bar{P} = \frac{1}{2}\rho A C_P(\bar{\lambda}, \beta_*)\bar{w}_0^3 \tag{2.30}$$

Suppose now that the $E(t)$ has been chosen such that an optimal angular velocity is found.

$$\bar{\lambda} = \lambda^* = \frac{R\Omega_*}{\bar{w}_0} \tag{2.31}$$

At steady state, this implies the equality

$$E_* = b\Omega_*^3, \quad b \triangleq \frac{1}{2}\rho A C_P^* \left(\frac{R}{\lambda^*}\right)^3 \tag{2.32}$$

Under steady and optimal conditions the electrical power can be given as a cubic function in Ω. Letting the electrical power follow from

Definition 2.2 (MPPT control law)**.**

$$E(\Omega) = b|\Omega|\Omega^2 \tag{2.33}$$

furnishes an "optimal" nonlinear torque control strategy. The stability and efficacy of this elegant control strategy is examined in Johnson et al. [48] who

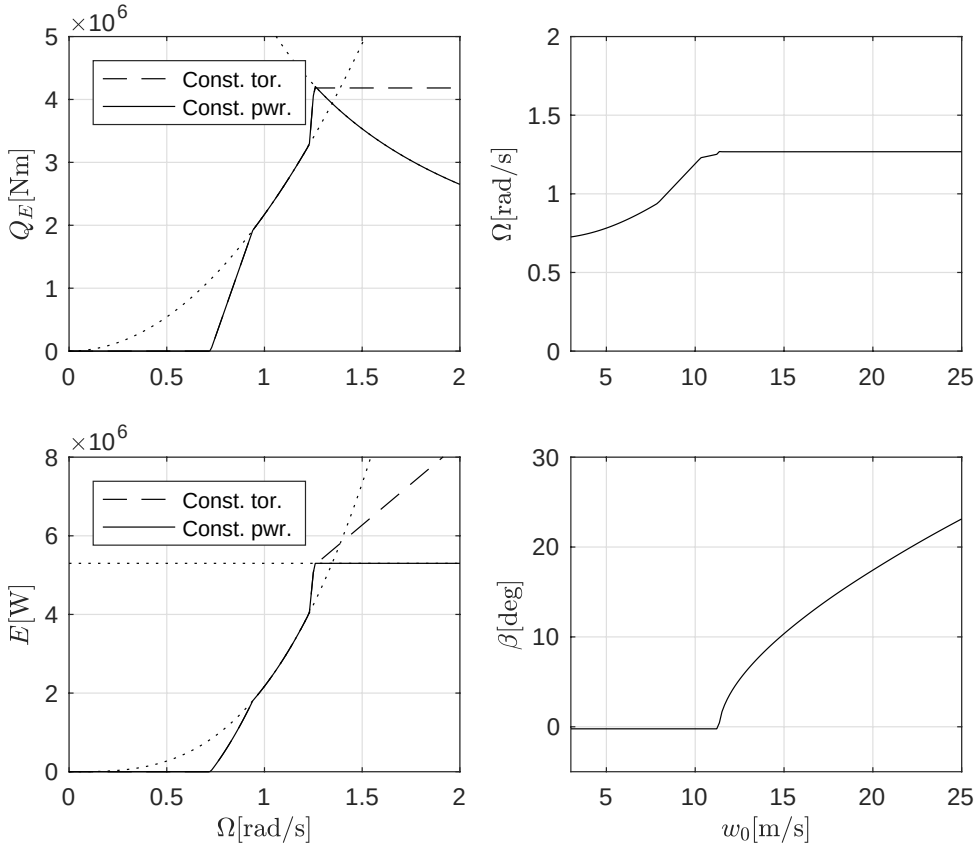

Figure 2.9.: *Left*: Electrical torque and power for a representative 5 MW wind turbine. Note that the mechanical power exerted by the generator exceeds the name plate rating. Inefficiencies will reduce the shaft power at 5.3 MW to an electrical power of 5 MW. The figure shows both constant power and constant torque strategies. The former yields smoother power delivery but comes with a penalty of reduced overall stability. *Right*: The equilibrium angular velocity and pitch deflection parameterized in the wind speed w_0. The pitch increases with the wind speed to limit the absorbed wind power. This is achieved indirectly through setpoint control of Ω.

demonstrate local asymptotic stability around the optimal tip-speed-ratio. While it is possible to elaborate on the cubic control law (2.33) large improvements do not seem to materialize. See Bossanyi [49] for a discussion. The main challenge in maximum power point tracking is in fact obtaining an accurate real-time estimate of the optimizing variables λ_* and β_*. While numerical simulation of the wind turbine aerodynamics furnish a good initial guess, experiments or online optimization should be used to arrive at the true values.

2.6.2. Power/torque saturation

Above a certain wind speed the rotor will produce more aerodynamic power or torque than the electrical componentry and geartrain can safely handle. This

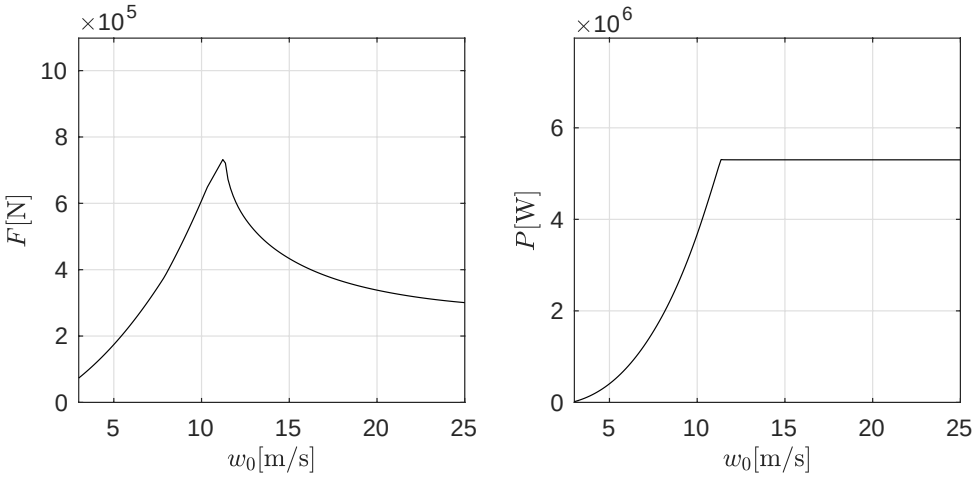

Figure 2.10.: Thrust and wind power parameterized in the wind speed w_0. A saturated power gives rise to a decreasing thrust as the wind speed increases, viz. $F \sim P/w_0$. This effect is realized by pitch control.

implies that the absorbed shaft power $E(t)$ must be limited. It is also important to limit the angular velocity Ω due to aeroelastic and transonic issues. While it is possible to achieve this through direct alterations in the rotor's angular velocity Ω using the generator torque Q_E, this forces the engineer to relinquish independent control of the electrical power production. Pitch control provides another avenue for speed control and is implemented on most offshore wind turbines. Having pitch control and torque control at one's disposal allows independent control of Ω and E. Modified regulators must be used in the power/torque limited operating regime. Let E^+ denote a roof on the allowed shaft power exerted by the generator, the so-called rated power. Power limiting is achieved by simple saturation

$$E(\Omega) \leq E^+ \tag{2.34}$$

The electrical torque $Q_E = E/\Omega$ may in certain cases serve as a more appropriate or convenient limiting variable. The following strategy can be used in these cases

$$E(\Omega) \leq Q_E^+ \Omega \tag{2.35}$$

Figure 2.9 shows how these limits affect the schedule $E(\Omega)$. The aerodynamic power must be limited in concert with the electrical power. This is typically achieved by placing the angular velocity at a constant setpoint Ω_0 through the use of pitch control. A constant rate of rotation implies that the electrical and aerodynamic power are balanced.

Pitch control of the angular velocity can be tackled well with simple PI-regulation. A variation appearing frequently in the literature [50, 13] involves gain-scheduling $g(\beta)$ parameterized in the pitch itself. The pitch sensitivity varies significantly with the wind speed rendering some form of schedule an

attractive option. This leads to a regulator on the form

$$\beta(t) = \int_0^t g(\beta(t'))K_P \left(\tilde{\Omega}(t) - T_d^{-1}\dot{\tilde{\Omega}}(t)\right)\, dt', \quad \tilde{\Omega}(t) = \Omega_0(t) - \Omega(t) \tag{2.36}$$

The pitch servo system is subject to dynamics on its own. Leithead and Connor [51] suggest a simple first order filter model with time-constant T_β relating the commanded pitch to the physical one, viz.

$$\frac{\beta}{\beta_c}(s) = \frac{1}{T_\beta s + s} \tag{2.37}$$

Sometimes, this model includes saturations on the rate reflecting physical limitations in the servo mechanism. Assuming that the time constant T_β is fast permits the simplification $\beta = \beta_c$.

The power optimizing strategy (2.33) places the turbine close to the optimal operating point where the power coefficient's partial derivatives w.r.t. to λ and β vanish.

$$\frac{\partial C_P(\lambda,\beta)}{\partial \lambda}(\lambda_*, \beta_*) = \frac{\partial C_P(\lambda,\beta)}{\partial \beta}(\lambda_*, \beta_*) \simeq 0 \tag{2.38}$$

This entails that the pitch sensitivity will be limited when operating close to the optimum. A transition regime aimed at increasing the pitch sensitivity in the vicinity of a power limit sees frequent use. The transition control should aim at reducing the tip-speed ratio to a suboptimal value $\lambda < \lambda_*$. This can be achieved through a variety of methods. One option is adding a simple linear ramp with slope b_1 to the optimal control (2.33).

$$E(\Omega) = \begin{cases} b\Omega^3 & \Omega < \Omega_0 \\ b\Omega^3 + b_1(\Omega - \Omega_0) & \Omega \geq \Omega_0 \end{cases} \tag{2.39}$$

See Figure 2.9 for an illustration. Other refinements to the schedule $E(\Omega)$ also appear, such as a startup region aimed at acquiring a given angular velocity.

3. Dynamic Vortex Theory

This chapter develops new theory for unsteady aerodynamics on a rotor disk. Old concepts such as the Joukowsky rotor are combined with control theoretical tools to produce a new loading/inflow model. The model will be validated successfully against experimental data in Chapter 4. A range of hitherto unknown properties of wind turbine aerodynamics are uncovered. For the first time, passivity tools are brought to bear on dynamic wake problem. The model is given a time domain realization using frequency domain identification. A simplified model exact in the low frequency limit is also furnished.

Dynamic vortex theory will now be used to give a unified treatment of the most important aerodynamic effects and phenomena in the wind turbine. This departs from the conventional introductory approach given in Chapter 2 where momentum theory was used. It will however be shown that momentum theory has a neat analogue in vortex theory. Vortex theory will prove ideally suited as dynamic wake effects are examined and clarify the underlying physics in some well known engineering approximations.

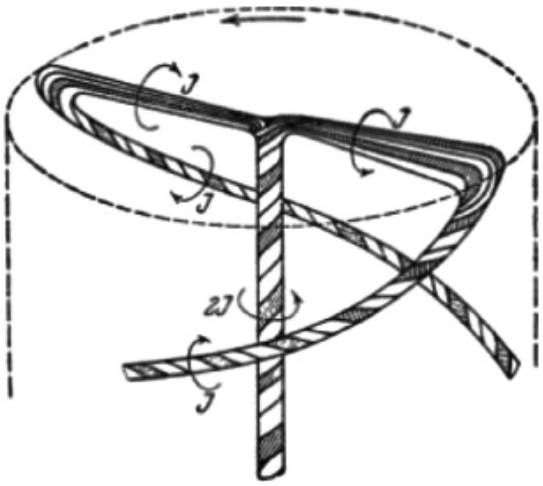

Figure 3.1.: The Joukowsky rotor. From Joukowsky [52].

The general idea of a vortex based rotor theory is shown in Figure 3.1. The blades, equipped with constant circulation Γ, shed vorticity into the wake in keeping with the Helmholtz laws of vortex motion. The shed vorticity will in turn induce a flow at the rotor in keeping with the Biot-Savart law [53].

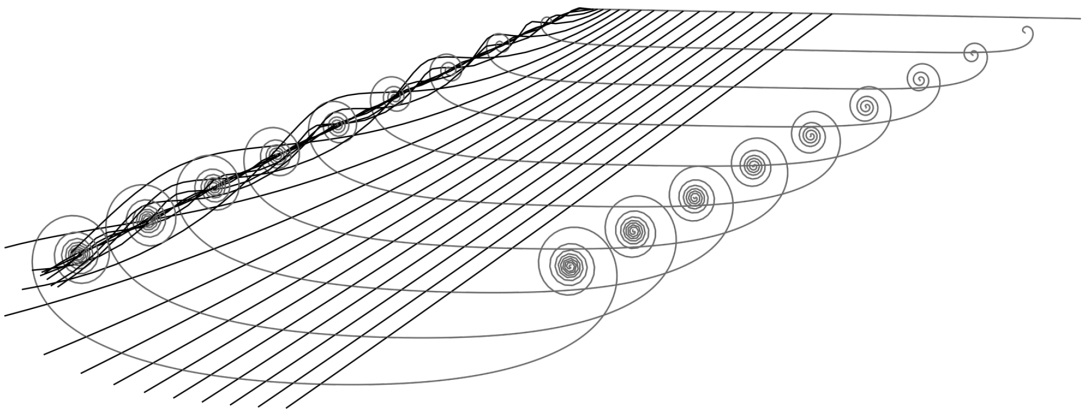

Figure 3.2.: Vortex shedding off a lifting line with an elliptical lift distribution. Note that the trailing vortices quickly roll up into concentrated tip vortices. The computation is based on Krasny [55].

It should be noted that vortex theory can be extended to allow modeling of radially varying circulation. The simplified scheme outlined above is known as the *Joukowsky rotor*. This construct provides a fair model of the blade loading in an efficient wind turbine. Constant circulation can actually be argued to be optimal in terms of power extraction which is of course the aim of good wind turbine design [54]. It is well known that lifting surfaces produces wakes that quickly rolls up into concentrated tip vortices as shown in Figure 3.2. This serves as an additional justification for Joukowsky's construction.

The vortex theory of wind turbines and propellers dates back to the beginning of the 20th century with pioneers such as Joukowsky [52]. Although the theory is very attractive in many respects, the considerable complexities associated with helical vortex filaments have limited practical applications. It is only in recent years that routine numerical evaluations of rotors modeled with vortices have been made possible. See e.g. Okulov and Sørensen [54]. At present, most engineering analysis is performed with the mathematically simpler momentum theory. However, many refinements such as tip-loss corrections [56] ultimately derive from vortex theory, being in some sense the more fundamental approach. The reader is referred to Okulov et al. [57] and van Kuik et al. [58] for an interesting historical overview of these theories.

3.1. Circulatory loading

The N blades on the rotor are modeled as lifting lines $\boldsymbol{l}$. Lifting lines can be used to represent high aspect ratio wings with superb accuracy, see e.g. Phillips and Snyder [59]. The lift on the blades is computed with the Kutta-Joukowsky theorem. Circulatory lift arises when a bound vortex filament is forced to undergo motion relative to the fluid. The most convenient formulation for a wind turbine is the vectorial variation furnished by Saffman [60]. An

element of the lifting line $\boldsymbol{l}$ will contribute the force shown below.

Model 3.1 (Vectorial vortex lifting law [60])**.**

$$d\boldsymbol{f} = \rho \boldsymbol{u}_{rel} \times \Gamma d\boldsymbol{l} \tag{3.1}$$

Note that the differential lift is normal to the relative flow by construction. Lift is therefore a lossless force since $d\boldsymbol{f} \cdot \boldsymbol{u}_{\text{rel}} = 0$; a property with significant consequences, both mathematically and physically.

The straight lifting lines are described differentially by $d\boldsymbol{l} = \boldsymbol{e}_r dr$ in a cylindrical coordinate system[1] (r, θ, z) capped by the rotor disk at $z = 0$. See Figure 1.6 for an illustration. The relative flow at the rotor disk will be modeled by

$$\boldsymbol{u}_{\text{rel}}(r, \theta, t) = \boldsymbol{e}_z \hat{w}(r, \theta, t) - \boldsymbol{e}_\theta \Omega(t) r \tag{3.2}$$

In the present setting tangential inflow can be assumed negligible and is therefore omitted. Radial inflow has no effect on the loading, being directed parallel to the lifting lines; its omission is of no consequence. The use of a purely axial inflow can therefore be expected to yield reasonable results. See Okulov and Sørensen [54] for a detailed analysis including tangential inflow, albeit in a steady setting.

Using (3.1) and (3.2) the circulatory thrust and torque can be computed by integrating the Kutta-Joukowsky force over the lifting lines and subsequently summing over the blades. The local force is on the i'th blade is readily derived as

$$\begin{aligned} d\boldsymbol{f}(r, \theta_i, t) &= \rho \Gamma(t)(\boldsymbol{e}_z \hat{w}(r, \theta_i, t) - \boldsymbol{e}_\theta \Omega(t) r) \times \boldsymbol{e}_r dr \\ &= \rho \Gamma(t)(\boldsymbol{e}_\theta \hat{w}(r, \theta_i, t) + \boldsymbol{e}_z \Omega(t) r) dr \end{aligned} \tag{3.3}$$

The identities shown below were used to arrive at this result.

$$\boldsymbol{e}_r \times \boldsymbol{e}_\theta = \boldsymbol{e}_z, \quad \boldsymbol{e}_\theta \times \boldsymbol{e}_z = \boldsymbol{e}_r, \quad \boldsymbol{e}_z \times \boldsymbol{e}_r = \boldsymbol{e}_\theta \tag{3.4}$$

The circulatory thrust can now be obtained by integrating the *normal* force over the lifting lines, viz.

$$F_c(t) = \sum_i^N \int_0^R \boldsymbol{e}_z \cdot d\boldsymbol{f}(r, \theta_i, t) = \rho \Gamma(t) \sum_i^N \int_0^R \Omega(t) r dr = \frac{\rho A N}{2\pi} \Gamma(t) \Omega(t) \tag{3.5}$$

Note that the thrust is aligned with $\boldsymbol{e}_z$ in keeping with wind engineering conventions. Before proceeding to compute the torque, recall that the averaged axial flux was defined by

$$w(t) \triangleq \frac{1}{AN} \sum_i^N \int_0^R \hat{w}(r, \theta_i, t)\ 2\pi r dr \tag{3.6}$$

[1] A coordinate system spinning *with* the rotor is utilized here.

The circulatory torque can be obtained by integrating the *tangential* force over the lifting lines, viz.

$$Q_c(t) = \sum_i^N \int_0^R r\boldsymbol{e}_\theta \cdot d\boldsymbol{f}(r,\theta_i,t)$$
$$= \rho\Gamma(t)\sum_i^N \int_0^R \hat{w}(r,\theta_i,t)rdr = \frac{\rho AN}{2\pi}\Gamma(t)w(t) \quad (3.7)$$

Note well that the torque depends on the *averaged* flow; the nonuniform part drops out of the integral. A summary of the preceding results is given below.

Model 3.2 (Circulatory loading)**.**

$$F_c(t) = \frac{\rho AN}{2\pi}\Gamma(t)\Omega(t) \qquad \textit{(Circulatory thrust)} \quad (3.8a)$$
$$Q_c(t) = \frac{\rho AN}{2\pi}\Gamma(t)w(t) \qquad \textit{(Circulatory torque)} \quad (3.8b)$$

The loading equations can be arrayed on a special form which will be referred to as the circulatory interconnection structure.

$$\begin{bmatrix} F_c \\ Q_c \end{bmatrix} = \frac{\rho AN}{2\pi}\begin{bmatrix} 0 & -\Gamma \\ \Gamma & 0 \end{bmatrix}\left(\begin{bmatrix} w_0 \\ 0 \end{bmatrix} - \begin{bmatrix} w_i \\ 0 \end{bmatrix} - \begin{bmatrix} \dot{x} \\ \Omega \end{bmatrix}\right)$$
(Circulatory interconnection structure) (3.9)

The right hand side is to be understood as being composed of an exogenous input w_0, taking away negative feedbacks from the wake w_i and motion described by $\dot{x}$ and Ω. Circulation connects the axial subsystem (F_c, w) with the rotating subsystem $(Q_c, -\Omega)$ in a lossless manner

$$F_c w + Q_c(-\Omega) = 0 \quad (3.10)$$

Circulation is central to wind turbines and propellers because it acts as the conduit between rotational and translational motion. For wind turbines, circulation takes wind power $F_c w$ losslessly into shaft power $Q_c\Omega$. Propellers utilize the same principle to turn shaft power, generated by a motor of some kind, into propulsive power.

Joukowsky rotors with fast spinning blades will, in an averaged sense, produce a uniform pressure jump Δp over the rotor plane. The normal blade force predicted by (3.3) reads as

$$df_n = \boldsymbol{e}_z \cdot d\boldsymbol{f} = \rho\Gamma\Omega r dr = \frac{F_c}{AN}\, 2\pi r dr \quad (3.11)$$

The last equality is obtained by inserting (3.8). Note here that the normal lift force assumes the form of a triangular distribution in r. Averaging is done by

dividing the blade force by the annular area at r. With $dA = 2\pi r dr$ the pressure jump due to N blades reduces to a constant

$$\Delta p = N\frac{df_n}{dA} = \frac{F_c}{A} \tag{3.12}$$

An optimally loaded turbine with uniform Δp can thus be realized with a fast spinning Joukowsky rotor. The result that constant circulation leads to optimal loading is remarkably robust. Significantly more elaborate models points to the same fact [54].

3.2. Inflow dynamics

Helmholtz' vortex laws dictate that vortex filaments cannot terminate in the fluid but must form closed loops. As a consequence, vorticity will be shed at the blade tips. Once shed into the fluid, the filaments will propagate away from the rotor frozen into the relative flow. As the turbine spins, the filaments will generate the helical wake structure shown in Figure 3.1. Higher angular velocities will lead to a tighter winding whilst an increased relative speed w will have the opposite effect. The filaments in the wake will induce a flow w_i at the rotor that depends on the helical pitch and the vortical intensity of the filaments producing the wake. When extracting power, this effect acts to reduce the effective flow through the rotor. This topic will be dealt with in more detail below. For now, it suffices to say that the inflow generated by the wake can be as a large as 50% of the wind speed w_0 in normal operation; a highly significant effect.

The averaged inflow $w_i(t)$ is now identified in the dynamic setting where momentum theory (2.18) ceases to apply. Although momentum theory does not apply in the unsteady problem, a close examination of its underpinnings will provide the impetus behind a new vortex-based theory.

It is possible to connect momentum theory with vortex theory by paying close attention to the streamtube used in the derivation of Rankine-Froude theory (2.14). Consider Figure 2.2. The streamtube separates the retarded flow within the slipstream from the undisturbed exterior flow. Evaluating the steady-state axial flow velocity over a control surface coplanar with S_2 one has

$$w_2(r) = \begin{cases} w_0 - 2w_i & r < R_2 \\ w_0 & r > R_2 \end{cases} \tag{3.13}$$

The discontinuity at the streamtube's perimeter $r = R_2$ arises due to the presence of vorticity. Let $\boldsymbol{n} = \boldsymbol{e}_r$ denote a unit vector normal to the surface of the streamtube and pointing outwards. Saffman [60] provides a formula for the velocity jump over a vortex sheet of intensity $\boldsymbol{\gamma}$, viz.

$$[\boldsymbol{u}]_2^1 = \boldsymbol{\gamma} \times \boldsymbol{n} \tag{3.14}$$

The notation $[\cdot]_2^1$ is used to signify a jump over a surface. Here side 1 is exterior to the wake whilst side 2 represents the inner face. By dotting both sides with the unit vector in the axial direction (oriented downstream) one may recover the wake vorticity as

$$\boldsymbol{e}_z \cdot [\boldsymbol{u}]_2^1 = w_0 - (w_0 - 2w_i) = 2w_i = \boldsymbol{e}_z \cdot (\boldsymbol{\gamma} \times \boldsymbol{e}_r) = -\gamma_\theta \tag{3.15}$$

Here θ denotes the azimuthal variable in the polar coordinate system used to describe the cylindrical wake. Vorticity is solenoidal, and being azimuthal it acquires the form of a distribution of vortex rings forming the streamtube, see Figure 3.3. The vorticity in the tube is transported downstream with a velocity equal to the average of the two sides of the tubular sheet. This is a well known property of vortex sheets [60].

Model 3.3 (Vortex transport velocity)**.**

$$w = \frac{w_0 + (w_0 - 2w_i)}{2} \tag{3.16}$$

Physically, this implies that a smooth slipstream is generated by continuous generation of vorticity at the disk. A key approximation is now introduced to aid in the examination of *time-varying* vorticity generation.

Assumption 3.1 (Rigid wake assumption)**.** *The vortex loops are assumed to retain their radius R as they are transported downstream. All loops in the wake are assumed to translate at the same rate $w(t)$.*

The rigid wake assumption is a crude approximation to the true physics. The wake must in fact expand as shown in (2.16) and the transport velocity will undergo a transient close to the disk before arriving asymptotically at the value given in (3.16). The two items in Assumption 3.1 are in fact both somewhat dubious, but *in combination* they result in a precise vortical analogue of momentum theory. Two wrongs therefore make a right in this special case.

The dynamic inflow model will depend on the *time-varying* transport velocity $w(t)$ through (3.19). The stationary value is given in (3.16), but extending this result to the dynamic setting requires additional reasoning. Assumption 3.1 dictates that the transport velocity should be the same for all vortex loops in the wake. The wind speed $w_0(t)$ dominates $w(t)$ and the vortices will indeed all move at this rate in the absence of inflow. This means that the contribution from $w_i(t)$ is of lesser (but still crucial) importance. Elaborations on the role of the inflow on the transport velocity could be made. However, practice has revealed that this leads to needless complications and no clear answers. Comparison to experimental data will justify the modeling choice.

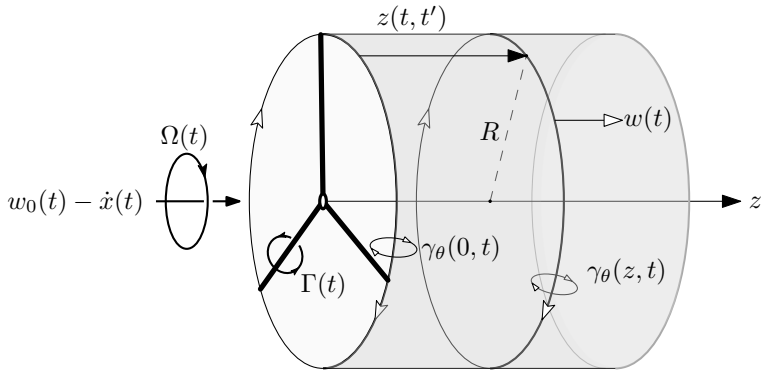

Figure 3.3.: The rotor with the trailing vortex tube. The high-aspect ratio rotor blades idealize to *lifting lines* $\boldsymbol{l}$ with circulation Γ.

3.2.1. An argument from conservation of momentum

A circular vortex loop encircling an area A is equipped with an impulse I given by the formula

$$I = \rho A \gamma_\theta \tag{3.17}$$

Here γ_θ denotes the intensity of the filament bounding A [61]. The impulse I is defined in the *downstream* direction. Suppose now that the thrust is applied in an impulsive fashion at $t = t'$ so that $F(t) = \delta(t - t')$. The inflow due to such an impulse, the wake's impulse response, is now sought. Conservation of momentum dictates that $dI/dt = -F^2$ so the filament's intensity acquires the form

$$\gamma_\theta^\delta(t) = -\frac{\Theta(t - t')}{\rho A} \tag{3.18}$$

Here, $\Theta(t)$ denotes Heaviside's step function. The filament will progress downstream after having been created at the rotor disk covering the distance[3]

$$z(t, t') = \int_{t'}^{t} w(t'')\ dt'' \tag{3.19}$$

A concentrated circular vortex loop of radius R located at z will produce a time-varying and radially nonuniform inflow at the disk which can be given by [62]

$$\hat{w}_i^\delta(r, t) = -\frac{R\gamma_\theta^\delta(t)}{2} \int_0^\infty l J_1(lR) J_0(lr) e^{-l|z(t,t')|}\ dl \tag{3.20}$$

Azimuthal symmetry permits omission of θ argument. Here J_n denotes the Bessel function of the first kind. There are other representations for the flow induced by circular vortex loops, but (3.20) will turn out to be a very suitable

[2]The thrust F acting on the rotor is balanced by a thrust on the fluid $-F$, hence the sign.
[3]The distance is taken relative to the rotor disk, so the inclusion of $\dot{x}$ captures the effect of the rotor moving away/towards the vortex loop.

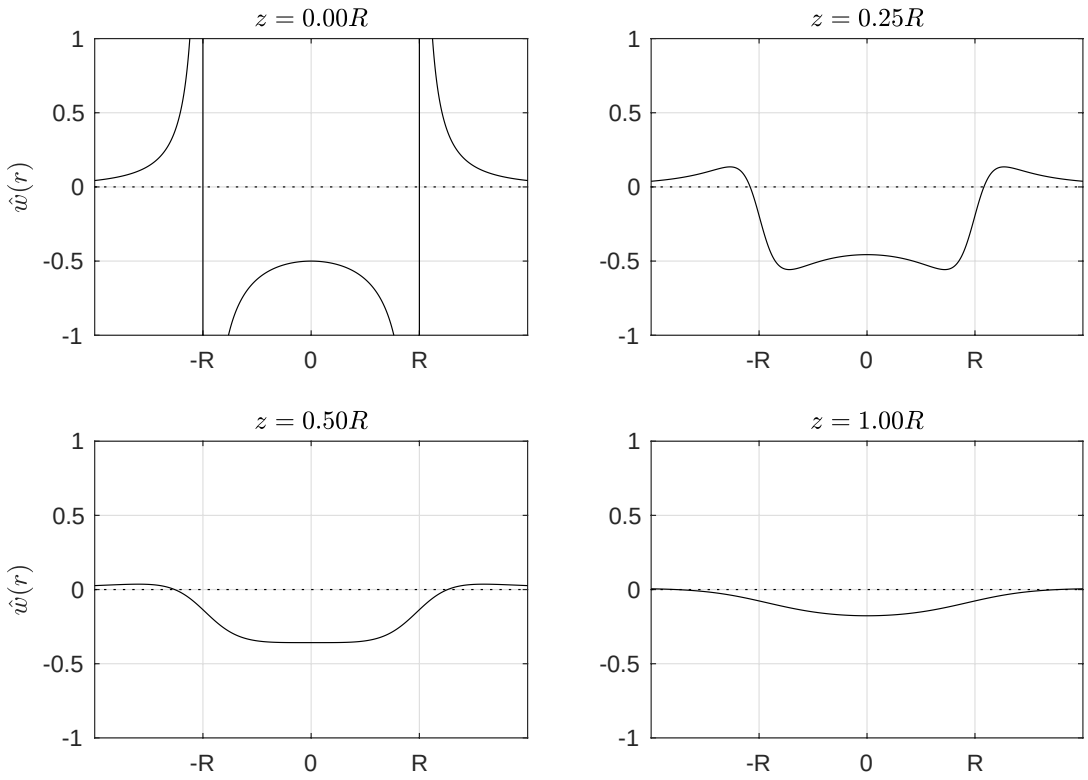

Figure 3.4.: The axial flow induced by a propagating vortex loop. Note that the inflow decays quickly as the vortex proceeds downstream.

formula for the present purpose. Utilizing the definition of the averaged flow (1.17) along with (3.18) and (3.20) leads to an expression for the impulsively generated averaged inflow

$$w_i^\delta(t) = \frac{\Theta(t-t')}{\rho A} \int_0^\infty J_1(lR)^2 e^{-l|z(t,t')|}\, dl \tag{3.21}$$

This is the wake's *impulse response*. A dynamic inflow model describing the averaged inflow can now be furnished by convolution, viz.

Model 3.4 (Dynamic inflow)**.**

$$w_i(t) = \int_0^t G(t,t')F(t')\, dt' \qquad \textit{(Dynamic inflow relation)} \tag{3.22a}$$

$$G(t,t') \triangleq \frac{\Theta(t-t')}{\rho A} \int_0^\infty J_1(lR)^2 e^{-l|z(t,t')|}\, dl \qquad \textit{(Vortical impulse response)} \tag{3.22b}$$

3.2.2. Connection to momentum theory

It is important that the convolution model (3.22) corresponds to Rankine-Froude momentum theory at steady state. Let the thrust be constant and assume that the transport velocity has arrived at a stationary value so that

$$|z(t,t')| = |w|(t-t') \tag{3.23}$$

Integrating the impulse response over time yields

$$\lim_{t\to\infty} \int_0^t G_w(t,t')\ dt' = \frac{1}{2\rho A|w|} \tag{3.24}$$

It therefore follows that the steady inflow must be equal to

$$w_i = \frac{F}{2\rho A|w|} \tag{3.25}$$

Rankine-Froude momentum theory (2.18) is thus recovered *exactly* as the equilibrium of the model. One may be surprised that the simplification of vortex tubes with constant radius and uniform transport velocity could lead to the well known equations of momentum theory. Furthermore, it is curious that one must use the near-field tube radius, but far-wake transport velocity. In Johnson [36] the near field density is used which gives a result that does not correspond to momentum theory. Miller [63] examines the case of a uniformly loaded rotor and points out that fundamental contradictions must be tolerated if one is to produce momentum theory from vortex theory. If the wake is transported with the flow, the neglect of wake expansion juxtaposed with a factor two increase in induced flow directly violates conservation of mass. Despite these concerns, the present scheme compares well with experiment. A case study is given in Chapter 4.

3.2.3. Connection to Joukowsky theory

The theory derived above can also be related to Joukowsky's rotor model where vorticity is shed into the wake. A lifting line with constant circulation exhibits a discontinuity at the blade tips (and roots) and here gives rise to a concentrated vortex filament of intensity Γ. All vorticity is therefore shed at the extremities of the lifting line. In the present model the root filament is neglected, implicitly assuming that tangential inflow is slight. If the vorticity is shed in a sufficiently smooth manner at the root and a high tip speed ratio $\lambda = \Omega R/w_0$ is assumed, this simplification is justifiable. The tip vortex sheds into a helical filament, a situation treated in mathematical detail by Okulov and Sørensen [54]. The present model differs from their more elaborate variety by approximating the helical vortex filaments, with the associated computational complexities, as closed loops of vorticity smeared onto a vortex tube where they form a continuum. In

a certain sense, this is equivalent to examining a rotor of infinitely many blades [56]. Once shed, the vortex loops proceed downstream at the velocity w.

During a time interval Δt each lifting line on the rotor sheds a tip vortex of length $\Delta\ell = \Omega R\Delta t$. The collective strength of these vortices is $N\Gamma$. Each segment of vorticity is distributed onto a cylindrical surface $\Delta\mathcal{S} = 2\pi Rw\Delta t$ where $w(t)$ represents the speed by which vorticity is emitted into the wake at the disk's edge. The relative flux is considered positive in this section.

The density of azimuthal vorticity immediately downstream of the rotor at $z = 0$ is at time t

$$\gamma_\theta(0,t) = -\frac{\Delta\ell}{\Delta\mathcal{S}}N\Gamma(t) = -\frac{N\Gamma(t)\Omega(t)}{2\pi w(t)} = -\frac{F_c(t)}{\rho A w(t)} \tag{3.26}$$

where (3.8) has been used. As time passes, the circular vortex elements will propagate downstream covering a distance given in (3.19). Relating distance traveled to elapsed time yields the time-varying azimuthal vorticity distribution along the tube in terms of a time-delay

$$\gamma(z,t) = \gamma(0,t') \tag{3.27}$$

This expression captures the fact that the vortex element at z retains the intensity it had when it was shed at time $t = t'$. Utilizing (3.20) yet again, now as an integral over the entire wake, yields the inflow

$$\hat{w}_i(r,t) = -\frac{R}{2}\int_0^\infty\int_0^\infty \gamma_\theta(z,t)lJ_1(lR)J_0(lr)e^{-l|z|}\,dl\,dz \tag{3.28}$$

The averaged inflow follows as

$$w_i(t) = -\int_0^\infty\int_0^\infty \gamma_\theta(z,t)J_1(Rl)^2e^{-l|z|}\,dl\,dz \tag{3.29}$$

Changing variables from space to time is accomplished by noting that (3.19) differentiates as

$$\frac{dz}{dt'} = -w(t') \tag{3.30}$$

The integration limits change as $z \to \infty \Rightarrow t' \to -\infty$ and $z = 0 \Rightarrow t' = t$. Applying the change of variables theorem noting (3.27) and (3.26) leads to

$$\begin{aligned} w_i(t) &= -\int_{-\infty}^t\int_0^\infty w(t')\gamma_\theta(0,t')J_1(Rl)^2e^{-l|z(t,t')|}\,dl\,dt' \\ &= \int_{-\infty}^t\left[\frac{1}{\rho A}\int_0^\infty J_1(Rl)^2e^{-l|z(t,t')|}\,dl\right]F_c(t')\,dt' \end{aligned} \tag{3.31}$$

This reproduces the previous result given in (3.22a)-(3.22b). The lower integration limit in the convolution integral can be set to zero by assuming that no

thrust is produced before $t = 0$. Note that this procedure indicates that one should only use the circulatory loading when computing the inflow, a contention also espoused in Wilson and Lissaman [41]. Momentum theory suggests that the full thrust is to be used. The practical difference between these two approaches is slight and since use of the full thrust will lead to a simpler model, momentum theory is followed.

3.3. The wake admittance

Having derived the basic model (3.22a)-(3.22b), the discussion now turns to its physical implications along with an examination of some salient properties. The *wake admittance* $\mathcal{Q}$ will be a central quantity in this pursuit. The relative flux $w(t)$ is assumed positive in this section.

The impulse response (3.22b) is time-varying which complicates analysis. It will be convenient to introduce a *reduced time* to get around this difficulty, viz.

Definition 3.1 (Reduced time)**.**

$$\tau(t) \triangleq \frac{1}{R}\int_0^t w(t')\ dt' \tag{3.32}$$

The differential relationship to physical time is here given by

$$\frac{d\tau}{dt}(t) = \frac{w(t)}{R} > 0 \tag{3.33}$$

The transport velocity is assumed positive, so the inverse function theorem guarantees that an inverse map $t(\tau)$ exists. It will however not be necessary to furnish this function explicitly. Another consequence is that an increase in physical time implies an increase in reduced time and vice-versa.

The distance traveled in physical time is given by (3.19) as

$$z(t, t') = \int_{t'}^t w(t'')\ dt'' \tag{3.34}$$

In reduced time, this transport distance simplifies to

$$z(\tau, \tau') = R(\tau - \tau') \tag{3.35}$$

The vortices will be carried away with one rotor radius R per reduced time unit. Changing variables from t to τ in the convolution model (3.22a)-(3.22b) simplifies matters greatly. Let $l' \triangleq Rl$ be used to simplify the improper integral and define the *wake admittance function* as

Definition 3.2 (Wake admittance function)**.**

$$\mathcal{Q}(\tau) \triangleq 2\Theta(\tau)\int_0^\infty J_1(l')^2 e^{-l'\tau}\ dl' \tag{3.36}$$

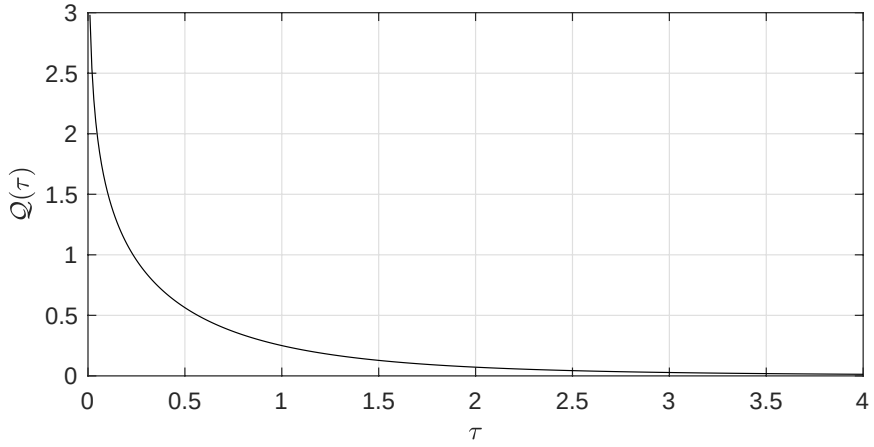

Figure 3.5.: Plot of the reduced impulse response (3.36).

The notion of admittance is borrowed from electrical engineering. Here, $\mathcal{Q}$ describes how a force (voltage) is turned into a flow (current). One may proceed to verify that the dynamic inflow model (3.22) now reduces to

$$w_i(\tau) = \int_0^\tau \mathcal{Q}(\tau - \tau') \frac{F(\tau')}{2\rho A w(\tau')} \, d\tau' \tag{3.37}$$

A comparison to (3.26) reveals that the underlying dynamics can be understood in terms of vortex shedding, as for the stationary Joukowsky rotor. The Laplace transform of $\mathcal{Q}(\tau)$ will be of interest but cannot be computed explicitly. It is however possible to obtain a semi-analytical result on the form

$$\mathcal{Q}(\sigma) = 2 \int_0^\infty \frac{J_1(l')^2}{\sigma + l'} \, dl' \tag{3.38}$$

Here σ is a reduced Laplace variable. The complex expansion of σ will be denoted

$$\sigma = \varrho + j\varpi \tag{3.39}$$

A frequency-domain model follows as

$$w_i(\sigma) = \mathcal{Q}(\sigma) \int_0^\infty \frac{F(\tau)}{2\rho A w(\tau)} e^{-\sigma\tau} \, d\tau \tag{3.40}$$

See Figure 3.8 for a graphical illustration of the frequency response. The meaning of the reduced Laplace variable can be elucidated by noting that the imaginary term corresponds to the dimensionless period $\Lambda \triangleq 2\pi/\varpi$. This period is measured in reduced time. Assuming a constant transport velocity, the corresponding period in physical time $\mathcal{T}$ is seen to be

$$\Lambda = \frac{w}{R}\mathcal{T} \tag{3.41}$$

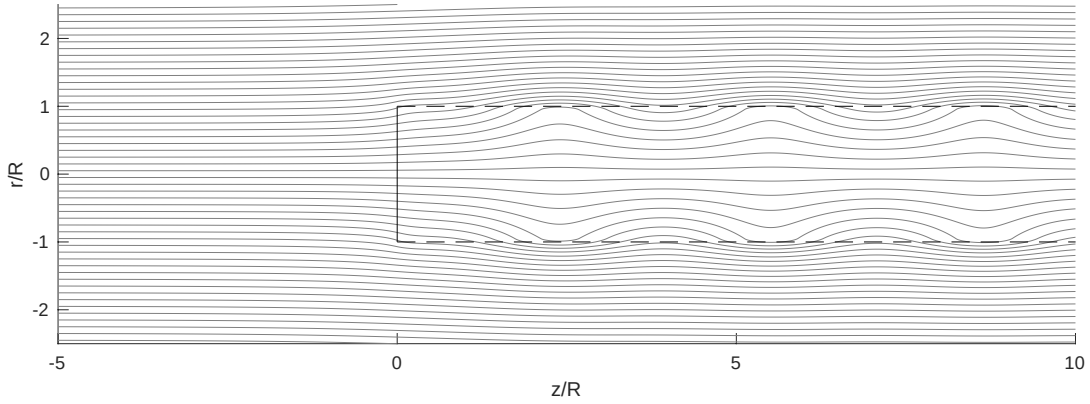

Figure 3.6.: The effect of sinusoidal load variations occurring at the reduced frequency $\varpi = 2$ superimposed with a steady mean flow. The flow field shown in the figure is complex, only the real part is shown. As time proceeds, the flow field perturbations will travel downstream in a wave-like manner with propagation velocity w. The frequency response of the averaged inflow is obtained by extracting the complex flow at the disk. (The black line signifies the rotor plane and the dashed line outlines the tubular wake).

A reduced unit period therefore corresponds to the time it takes for a vortex to cover one rotor radius; frequencies $\varpi/2\pi$ assume the meaning of inverse wavelengths Λ for the wake perturbations. A visual explanation can be found in Figure 3.6.

A cursory examination of Figure 3.8 and Figure 3.7 reveals that the wake acts as a low-pass filter on the thrust. The wake is seen to be equipped with infinitely many stable poles, quite expected being a distributed parameter system. An immediate implication is that one cannot find a realization given in terms of a finite number of states. It should be noted that distributed parameter systems are quite common in aerodynamics, a salient example being Theodorsen's function [64].

3.3.1. Technical Properties

The wake admittance function (3.36) is equipped with a number of useful properties germane to simulation and control. An examination of $\mathcal{L}_p$-gain establishes input-output stability. Passivity will be used for stability analysis in Chapter 5.

$\mathcal{L}_p$-stability.

It is now be shown that the $\mathcal{Q}$-filter is finite-gain $\mathcal{L}_p$-stable. Define the following reduced-time input and output for notational brevity

$$y(\tau) \triangleq w_i(\tau), \quad u(\tau) \triangleq \frac{F(\tau)}{2\rho A w(\tau)} \tag{3.42}$$

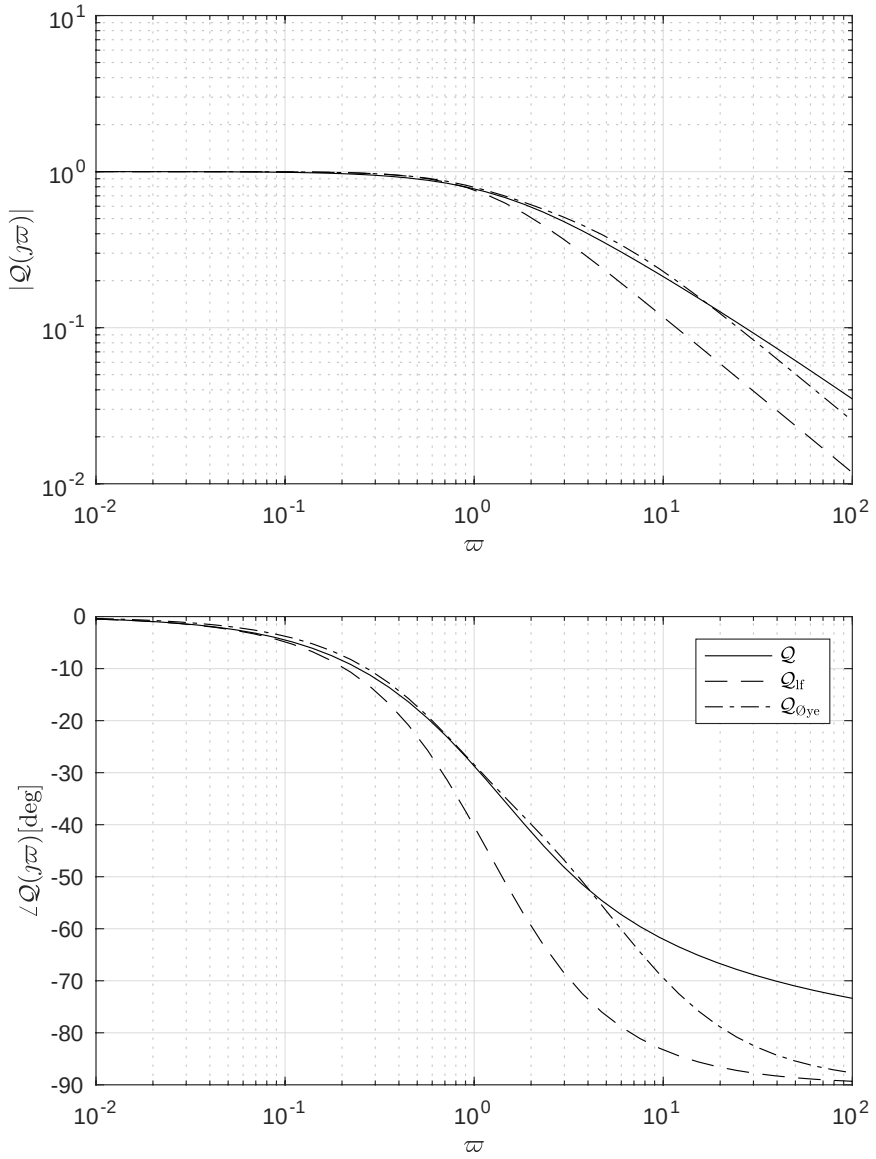

Figure 3.7.: Bode diagram of the wake admittance function $\mathcal{Q}(\sigma)$. A first order low frequency approximation (3.71) and the Øye model (3.81) are also shown.

Note that the output appears in $w(\tau) = w_0(\tau) - y(\tau) - \dot{x}(\tau)$. This implies a nonlinear relationship between the input and output. The simplified notation gives rise to the following integral equation obtained from (3.37).

$$y(\tau) = \int_0^\tau \mathcal{Q}(\tau - \tau')u(\tau')\, d\tau' \tag{3.43}$$

The impulse response satisfies the important property

$$\|\mathcal{Q}\|_{\mathcal{L}_1} = \int_0^\infty |\mathcal{Q}(\tau)|\, d\tau = 2\int_0^\infty \frac{J_1(l')^2}{l'}\, dl' = 1 \tag{3.44}$$

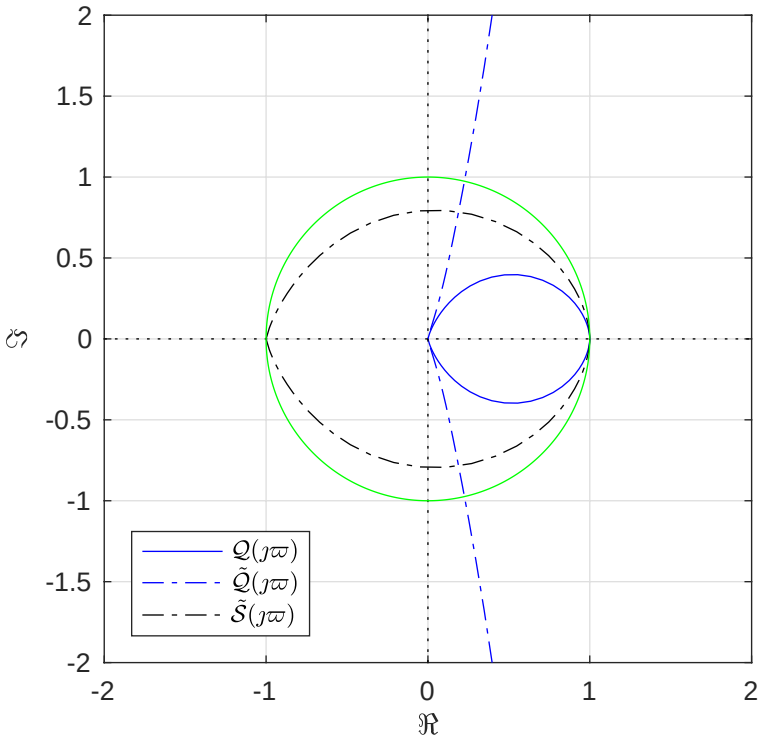

Figure 3.8.: A Nyquist diagram of the wake admittance function (3.38), the modified variation (3.48) and the associated scattering function (3.50). The DC-gain is found at $\mathcal{Q}(0) = 1$.

Following Khalil [21, Example 5.2] this implies finite-gain stability so that

$$\|y\|_{\mathcal{L}_p} \leq \gamma \|u\|_{\mathcal{L}_p}, \quad \gamma = 1 \tag{3.45}$$

The $\mathcal{L}_p$-gain is therefore unity. Since $\mathcal{Q}(\tau) \geq 0$ the DC-gain is seen to be unity also. Input-output stability is thus established.

Passivity

A Laplace domain representation with (3.38) reads as

$$y(\sigma) = \mathcal{Q}(\sigma)u(\sigma) \tag{3.46}$$

The OSP[4] property for a SISO system is defined by the following inequality [16, Definition 2.1] valid for $\tau \geq 0$.

$$\int_0^\tau y(\tau')u(\tau')\, d\tau' \geq \varrho \int_0^\tau y^2(\tau')\, d\tau' - \beta \tag{3.47}$$

Here, $\varrho > 0$ is a positive constant whilst $\beta \geq 0$ is nonnegative [65]. The $\mathcal{Q}$-filter is equipped with a significant excess of output passivity (quantified by ϱ) which

[4]Output Strict Passivity

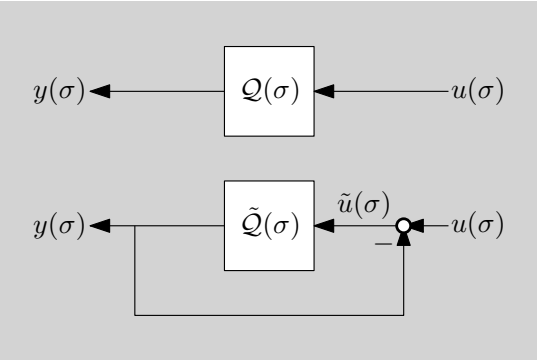

Figure 3.9.: Modification of the input recovers the wake dynamics on a modified form.

can be extracted through a redefined output, viz.

$$\tilde{u}(\sigma) \triangleq u(\sigma) - y(\sigma), \quad y(\sigma) = \tilde{\mathcal{Q}}(\sigma)\tilde{u}(\sigma), \quad \tilde{\mathcal{Q}}(\sigma) \triangleq \frac{\mathcal{Q}(\sigma)}{1 - \mathcal{Q}(\sigma)} \tag{3.48}$$

See Figure 3.9 for an illustration. Physically, $\tilde{u}$ corresponds to the imbalance in the applied force and the momentum flux, as seen from

$$2\rho A w(\tau)\tilde{u}(\tau) = F(\tau) - 2\rho A w(\tau) w_i(\tau) \tag{3.49}$$

The modified wake filter $\tilde{\mathcal{Q}}(\sigma)$ is passive, equivalently *positive real* (PR). An argument from Brogliato et al. [16] is invoked to show this. The *scattering function* associated with the modified filter is given by

$$\mathcal{S}(\sigma) \triangleq \frac{\tilde{\mathcal{Q}}(\sigma) - 1}{1 + \tilde{\mathcal{Q}}(\sigma)} = 2\mathcal{Q}(\sigma) - 1 = 2\int_0^\infty \frac{J_1(l')^2}{\sigma + l'}\, dl' - 1 \tag{3.50}$$

The following identity is now put to use

$$2\int_0^\infty \frac{J_1(l')^2}{l'}\, dl' = 1 \quad \Rightarrow \mathcal{S}(\sigma) = -2\int_0^\infty \frac{\sigma J_1(l')^2}{l'(\sigma + l')}\, dl' \tag{3.51}$$

Note well that $\mathcal{S}(\varrho + \jmath\varpi)$ is analytic for $\varrho > 0$. The scattering function is also real for $\varpi = 0$. The amplitude of the scattering function can be computed and bounded in the following manner

$$|\mathcal{S}(\varrho + \jmath\varpi)| = 2\int_0^\infty \sqrt{\frac{\varrho^2 + \varpi^2}{(\varrho + l')^2 + \varpi^2}} \frac{J_1(l')^2}{l'}\, dl' \leq 2\int_0^\infty \frac{J_1(l')^2}{l'}\, dl' = 1 \tag{3.52}$$

Gathering facts proves that the scattering function is *bounded real* [16, Definition 2.24]. It can now be concluded that the modified filter $\tilde{\mathcal{Q}}(\sigma)$ is passive (positive real) using the result in Brogliato et al. [16, Theorem 2.26]. Visual inspection of Figure 3.8 corroborates this finding. It has thus been shown that

$$\int_0^\tau y(\tau')\tilde{u}(\tau')\, d\tau' = \int_0^\tau y(\tau')(u(\tau') - y(\tau'))\, d\tau' \geq 0 \tag{3.53}$$

With $\tilde{\mathcal{Q}}$ passive, an immediate implication is that $\mathcal{Q}$ is output strictly passive (OSP). The preceding inequality is equivalent to the definition of OSP given in (3.47) setting $\varrho = 1$ and $\beta = 0$. The results of the preceding discussion are itemized below.

Proposition 3.1 (Properties of the wake system)**.**
The wake system can be described by the equivalent representations shown below.

$$y(\tau) = \int_0^\tau \mathcal{Q}(\tau - \tau')u(\tau')\ d\tau', \qquad \mathcal{Q}(\tau) = 2\Theta(\tau)\int_0^\infty J_1(l')^2 e^{-l'\tau}\ dl' \tag{3.54}$$

$$y(\sigma) = \mathcal{Q}(\sigma)u(\sigma), \qquad \mathcal{Q}(\sigma) = 2\int_0^\infty \frac{J_1(l')^2}{\sigma + l'}\ dl' \tag{3.55}$$

It is equipped with the following properties:

$\mathcal{L}_p$-stability

$$\|y\|_{\mathcal{L}_p} \geq \gamma \|u\|_{\mathcal{L}_p}, \quad \gamma = 1 \tag{3.56}$$

Output strict passivity

$$\int_0^\tau y(\tau')u(\tau')\ d\tau' \geq \varrho \int_0^\tau y^2(\tau')\ d\tau' - \beta, \quad \varrho = 1,\ \beta = 0 \tag{3.57}$$

Unit DC-gain

$$\lim_{\sigma \to 0} \mathcal{Q}(\sigma) = 1 \tag{3.58}$$

Strict properness

$$\lim_{\sigma \to \infty} \mathcal{Q}(\sigma) = 0 \tag{3.59}$$

These results will be important when finding a time domain realization of the inflow dynamics. Also, the possibility of finding analytical evidence of passivity is very encouraging since this work is preoccupied with that particular property.

The preceding results are set in reduced time. Changing variables with (3.33) in (3.53) permits the following inequality.

$$\frac{1}{R}\int_0^t y(t')\tilde{u}(t')w(t')\ dt' = \frac{1}{R}\int_0^t y(t')(u(t') - y(t'))w(t')\ dt' \geq 0 \tag{3.60}$$

Inserting the definitions in (3.42) shows that

$$\frac{1}{2\rho A R}\int_0^t w_i(t')\left(F(t') - 2\rho A w(t')w_i(t')\right)\ dt' \geq 0 \tag{3.61}$$

Concluding, the wake system is *output strictly passive* from input $F(t)$ to output $w_i(t)$ and *passive* if the following modified input is used

$$\tilde{F}(t) \triangleq F(t) - 2\rho A w(t)w_i(t) \tag{3.62}$$

The unit DC-gain of the wake system implies the steady state relationship $\bar{y} = \bar{u}$. This indicates that $\tilde{F} = 0$ describes the equilibrium in accordance with Rankine-Froude momentum theory (2.18).

3.4. Realization

The properties demonstrated in Proposition 3.1 suggests that the wake admittance filter $\mathcal{Q}(\sigma)$ can be equipped with a finite-dimensional strictly proper and output strictly passive approximation on the form

$$\mathcal{Q}(\sigma) \simeq \boldsymbol{c}(\sigma\mathbb{I} - \boldsymbol{A})^{-1}\boldsymbol{b} \tag{3.63}$$

This approximation corresponds to the reduced-time-invariant state dynamics described by

$$\frac{d\boldsymbol{x}}{d\tau}(\tau) = \boldsymbol{A}\boldsymbol{x}(\tau) + \boldsymbol{b}u(\tau), \quad y(\tau) = \boldsymbol{c}\boldsymbol{x}(\tau) \tag{3.64}$$

The input and output are defined by $u = F/2\rho Aw$ and $y = w_i$.

The system matrices $\boldsymbol{A}$, $\boldsymbol{b}$ and $\boldsymbol{c}$ are identified through frequency domain fitting of $\mathcal{Q}(j\varpi)$ using the methodology described in Gustavsen and Semlyen [66]. The Matrix Fitting Toolbox [67] is capable of forcing properties such as passivity and strict properness on the fit making it ideal for the present purpose. Figure 3.10 shows that it is possible to obtain approximations of a quality that is, to all intents and purposes, perfect.

The linear system can be pulled back to physical time by using (3.33) and the inverse function theorem in the following manner

$$\begin{aligned}\frac{d\boldsymbol{x}}{d\tau}(\tau) = \left(\frac{d\boldsymbol{x}}{dt}(t) \circ t(\tau)\right)\frac{dt}{d\tau}(\tau) &= \left(\frac{d\boldsymbol{x}}{dt}(t) \circ t(\tau)\right)\left(\frac{d\tau}{dt}(t) \circ t(\tau)\right)^{-1} \\ &= \left(\frac{R}{w(t)}\frac{d\boldsymbol{x}}{dt}(t)\right) \circ t(\tau)\end{aligned} \tag{3.65}$$

The result is an LTV wake admittance filter that is readily implemented in a digital simulation

$$R\dot{\boldsymbol{x}}(t) = w(t)\boldsymbol{A}\boldsymbol{x}(t) + w(t)\boldsymbol{b}u(t), \quad y(t) = \boldsymbol{c}\boldsymbol{x}(t) \tag{3.66}$$

The nonlinear dynamics in (3.22a)-(3.22b) can now be given on a lumped form. Having used (3.37) as an intermediate step, the inflow dynamics can be given on the practical form shown below.

Model 3.5 (Passive realization)**.**

$$2\rho AR\frac{d\boldsymbol{x}}{dt}(t) = 2\rho A|w(t)|\boldsymbol{A}\boldsymbol{x}(t) + \boldsymbol{b}F(t), \quad w_i(t) = \boldsymbol{c}\boldsymbol{x}(t) \tag{3.67}$$

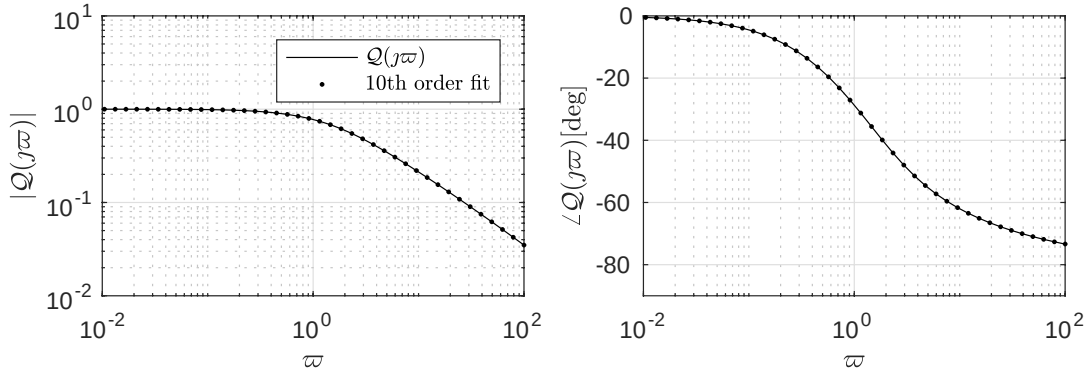

Figure 3.10.: The wake admittance function compared to a 10th order rational fit.

Here, the absolute value of w is used in accordance with (2.18). Repeating the preceding developments assuming $w(t) < 0$ will show that this is correct. Note that the model is nonlinear and not only time-varying since the output appears in the state dynamics through $|w(t)| = |w_0(t) - w_i(t) - \dot{x}(t)|$.

3.4.1. Low frequency approximation

It turns out that the modified wake filter (3.48) can be represented well by a simple integrator at low frequencies

$$\tilde{\mathcal{Q}}(\sigma) \simeq \frac{1}{\mu\sigma}, \quad \sigma \ll 1 \tag{3.68}$$

The appropriate time constant μ is identified through the following limiting procedure

$$\mu \triangleq \lim_{\sigma\to 0} \frac{1}{\sigma\tilde{\mathcal{Q}}(\sigma)} = \lim_{\sigma\to 0} \frac{1 - 2\int_0^\infty J_1(l')^{\,2}/l' \; dl' + 2\sigma\int_0^\infty J_1(l')^{\,2}/l'^2 \; dl'}{2\int_0^\infty J_1(l')^{\,2}/l' \; dl'} = \frac{8}{3\pi} \tag{3.69}$$

The parameter μ plays the role of a dimensionless "virtual inertia".

Definition 3.3 (DVT inertia coefficient)**.**

$$\mu_{\mathrm{DVT}} \triangleq \frac{8}{3\pi} \tag{3.70}$$

Since $\mathcal{Q} = \tilde{\mathcal{Q}}(1 + \tilde{\mathcal{Q}})^{-1}$ a low frequency approximation for $\mathcal{Q}$ is given by the low-pass filter

$$\mathcal{Q}_{\mathrm{lf}}(\sigma) = \frac{1}{\mu\sigma + 1} \tag{3.71}$$

A graphical illustration of this approximation is given in Figure 3.7. Realizing the filter (3.71) on the form (3.64) gives the following scalar system matrices

$$A = -\frac{1}{\mu}, \quad b = \frac{1}{\mu}, \quad c = 1 \tag{3.72}$$

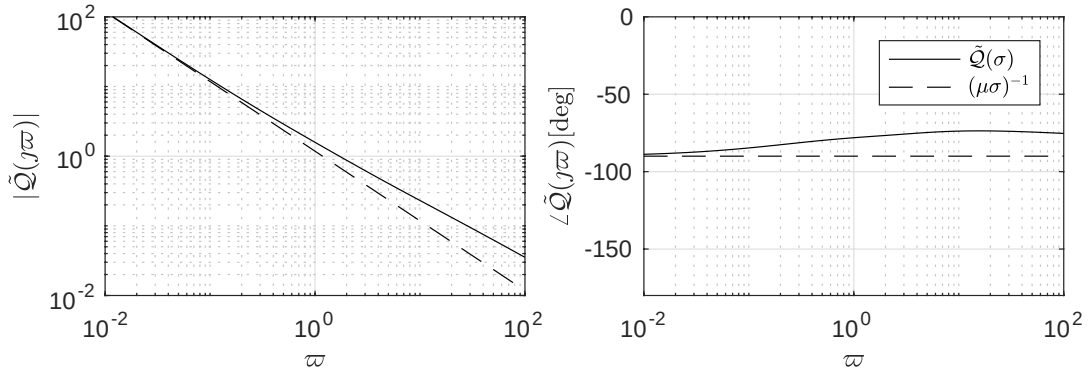

Figure 3.11.: The balance filter $\tilde{\mathcal{Q}}(\sigma)$ acts, in essence, as an integrator.

At low frequencies (3.67) is therefore well approximated by the scalar model

Model 3.6 (Low frequency approximation)**.**

$$2\rho AR\mu\dot{w}_i(t) + 2\rho A|w(t)|w_i(t) = F(t) \tag{3.73}$$

This low frequency approximation will be useful when making comparisons to existing work in the field and for simplified stability analysis. A Bode-diagram comparing the low-frequency model to the distributed plant is shown in Figure 3.7 and a comparison of the step responses is shown in Figure 3.12.

Remark 3.1. *The balance function $\tilde{\mathcal{Q}}(\sigma)$ serves as the loop transfer function in the feedback diagram Figure 3.9. Comparing the low-frequency approximation to the true dynamics in Figure 3.11 shows that $\tilde{\mathcal{Q}}(\sigma)$ injects additional damping at high-frequencies. This implies that (3.73)* under-predicts *the stabilizing effects of vortex shedding.*

3.5. Comparison to existing work on wake dynamics

It seems prudent to compare the present model (3.22a)-(3.22b), fully realized in (3.67) and approximated in (3.73), to existing work in the field. Two main approaches seem to dominate the science, methods based on an acceleration potential and vortex methods.

3.5.1. Øye's vortex model

The dynamic inflow model developed in this chapter is not unique in being informed by analysis of a vortical wake. Other vortex based inflow models do indeed exist. A notable example is the pragmatic time-domain model proposed in Øye [68]. See also [39]. Here a second order nonlinear filter was employed

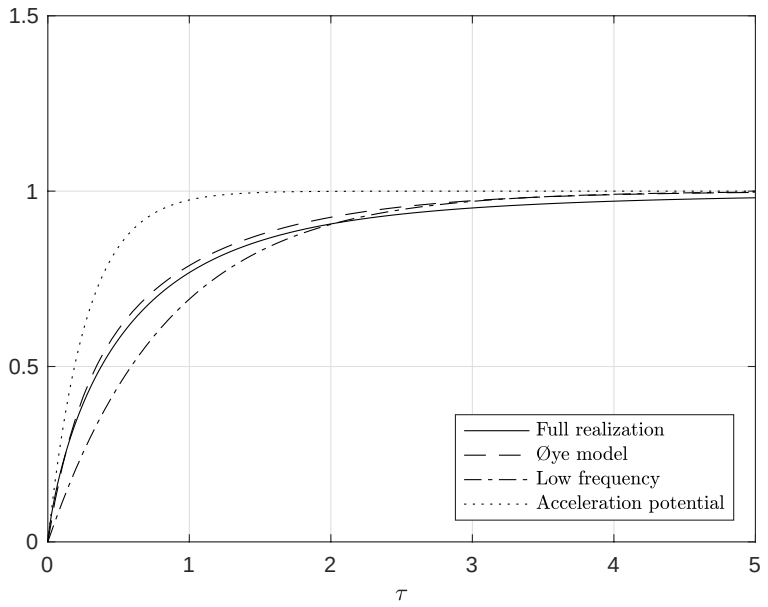

Figure 3.12.: The reduced-time step response of the high order model (3.67) compared to the Øye model (3.74), the low frequency approximation (3.73) and an acceleration potential model using the virtual mass given in (3.84).

to generate a transient response which correlated well to experimental data, whilst being rooted in vortex-based considerations. In Chapter 4 the present model is validated on the very data used to inform the Øye model. It should be noted that little theoretical justification is provided for the filter design. The present analysis, even with its various simplifications, derives from fundamental principles of aerodynamics.

Øye's model can be supplied on the form of a nonlinear filter cascade

$$\tau_1(t)\dot{w}_1(t) + w_1(t) = k\tau_1(t)\dot{w}_i^{\mathrm{qs}}(t) + w_i^{\mathrm{qs}}(t) \tag{3.74a}$$

$$\tau_2(r,t)\dot{\hat{w}}_i(r,t) + \hat{w}_i(r,t) = w_1(t) \tag{3.74b}$$

The time-varying coefficients are given by

$$\tau_1(t) = \frac{1.1}{1-1.3a(t)}\frac{R}{w_0(t)}, \quad \tau_2(r,t) = (0.39 - 0.26(r/R)^2)\tau_1(t), \quad k = 0.6 \tag{3.75}$$

In order to allow comparison to the present model, the form of Øye's filter will be altered slightly. The quasi-static inflow w_{qs} can be computed by using momentum theory

$$w_i^{\mathrm{qs}}(t) = \frac{F(t)}{2\rho A w(t)} \tag{3.76}$$

Assuming moderate inflow $a < 1/3$ permits the approximation

$$\tau_1(t) \approx \frac{R}{w(t)} \tag{3.77}$$

This allows the system to be represented in reduced time, now as a linear reduced-time-invariant filter cascade

$$\frac{dw_1}{d\tau}(\tau) + w_1(\tau) = k\frac{dw_i^{\text{qs}}}{d\tau}(\tau) + w_i^{\text{qs}}(\tau) \tag{3.78a}$$

$$(0.39 - 0.26(r/R)^2)\frac{d\hat{w}_i}{d\tau}(r,\tau) + \hat{w}_i(r,\tau) = w_1(\tau) \tag{3.78b}$$

The Laplace transform of this system can be used to extract the frequency domain relation

$$\hat{w}_i(r,\sigma) = \frac{1}{(0.39 - 0.26(r/R)^2)\sigma + 1}\frac{k\sigma + 1}{\sigma + 1}\hat{w}_i^{\text{qs}}(\sigma) \tag{3.79}$$

The averaging convention (1.17) is now used to compute the averaged inflow

$$w_i(\sigma) = \left[\frac{1}{A}\int_0^R \frac{1}{(0.39 - 0.26(r/R)^2)\sigma + 1}\, 2\pi r dr\right]\frac{k\sigma + 1}{\sigma + 1}w_i^{\text{qs}}(\sigma) \tag{3.80}$$

Comparison to (3.40) whilst noting (3.76) furnishes Øye's wake admittance function

$$\mathcal{Q}_{\text{Øye}}(\sigma) = \frac{(0.6\sigma + 1)(3.85\log(\sigma + 2.56) - 3.85\log(\sigma + 7.69) + 4.23)}{\sigma(\sigma + 1)} \tag{3.81}$$

The frequency response of this function is shown in (3.7) where it can be compared to the wake admittance function derived herein. The two transfer functions are indeed very similar. The Øye model is heavily informed by empirical data, indicating that the theory developed in this chapter is sound. Experimental validation undertaken in Chapter 4 will bolster this contention.

3.5.2. Acceleration potential models

Inflow models exemplified by a mass-damper system seems to have originated with the work of Carpenter and Fridovich [69] where the effects of rapid blade pitching on a helicopter was examined. Their model is given below.

$$m_a\dot{w}_i + 2\rho A w w_i = F \tag{3.82}$$

The damping term is simply that furnished by Rankine-Froude momentum theory [35]. The novelty in [69] was the addition of an apparent mass term m_a which represents the lag in inflow following a change in thrust. This "mass" was suggested to be 63.7% of a sphere of fluid with radius equal to the rotor.

$$m_a = 0.637 \cdot \frac{4}{3}\rho A R \tag{3.83}$$

The basic mass-damper model was refined by Pitt and Peters [70], who in addition to modeling the effects of forward flight, arrived at the same value for the

apparent mass. The mass was however corrected in later works to the following value [25]

$$m_a = \frac{128}{75\pi}\rho A R \tag{3.84}$$

This family of models are similar to the acceleration-potential method of van Bussel [24] in that they both employ a methodology originating with Kinner [71]. This approach solves a Laplace equation for the pressure in an oblate spheroidal coordinate system permitting separation of variables. The resulting solution (given as a harmonic expansion) is related to the flow field under an assumption of small perturbation flow. Methods of this general class [31, 24] all seem to suggest the added mass (3.84). The mathematics underlying the acceleration-potential method are rather involved, consult [72, 24] for details. It should be noted that later works recommend the added mass from an impermeable disk translating in heave $m_a = \rho(8/3)R^3$ [73].

The methods cited above all derive from variations on the acceleration potential method which is fundamentally different from the present approach. For comparison purposes, the case of light loading and constant wind speed is assumed. A general form of the dynamic inflow equations is then

$$\mu\left(\frac{R}{w_0}\right)\dot{w}_i + w_i = \frac{F}{2\rho A w_0} \tag{3.85}$$

Here, μ represents a dimensionless time-constant. A comparison of the various models in terms of μ is given below

$$\mu_{\mathsf{DVT}} = \frac{8}{3\pi} \simeq 0.85, \quad \mu_{\mathsf{AP}} = \frac{64}{75\pi} \simeq 0.27, \quad \mu_{\mathsf{disk}} = \frac{4}{3\pi} \simeq 0.42 \tag{3.86}$$

It is a matter of some concern that the time constants vary so much; the quantitative behavior of the models differ significantly. See Figure 3.12.

Acceleration potential methods have been extended to permit computation of disk-varying inflow generated by a pressure distribution that is also permitted to vary over the actuator disk. Peters et al. [72] underscores that these generalized variations contain the simple scalar model exemplified by (3.82) and (3.84) as a special case. This implies that the disagreement uncovered above should persist even if more advanced versions of the acceleration-potential method is used.

The theories giving rise to the time constants differ greatly and identifying a single point of disagreement is therefore difficult. The acceleration potential method predicts something akin to an added-mass effect. It is not immediately obvious how a rotor relates to this concept. On the other hand, the present development relies on a very idealized vortex system which fails to satisfy basic laws of vortex motion. However, comparison to experiment in the next chapter will reveal that the present method is superior. As demonstrated, the Øye model also agrees better with the new theory.

3.6. Chapter summary

This chapter can be summarized as follows:

- In Section 3.1 the circulatory thrust $F_c(t)$ and torque $Q_c(t)$ were derived using Joukowsky's rotor construction. The circulatory interconnection structure inherent in Joukowsky's model was identified.

- In Section 3.2 the averaged dynamic inflow $w_i(t)$ was modeled in the vortex paradigm. Adopting a rigid-wake assumption (Ass. 3.1) and employing conservation of momentum, a dynamic wake model (3.22a)-(3.22b) was derived in the form of a convolution integral. Comparison to Rankine-Froude momentum theory was used to identify the correct vortex transport velocity; an important constituent in the model. It was also shown that the new model extends the Joukowsky rotor to the dynamic setting, albeit at the assumption of negligible tangential inflow and using a smeared approximation of the helical filaments.

- The theory derived in Section 3.3 defined and explored the wake admittance function $\mathcal{Q}$, a central but hitherto unexplored quantity in wake dynamics. By expressing the dynamics in reduced time it was possible to bring a frequency domain analysis to bear on the problem, see (3.40,3.38). A range of important properties for $\mathcal{Q}$ were identified in proposition 3.1.

- In Section 3.4 the dynamic wake model was realized as a nonlinear ODE (3.67) using frequency domain identification. A model valid for low-frequency excitations was furnished by (3.73).

- In Section 3.5 comparisons were made to existing models. It was shown in Figure 3.7 and Figure 3.12 that the new model compares well to the Øye model but gives significantly slower transients than models derived using the acceleration potential method.

4. Engineering Model

This chapter describes how dynamic vortex theory can be used in practical applications. Drag and tip-loss corrections are introduced. Explicit forms for the circulation and a drag factor are found with an equivalent airfoil analogy. A method converting existing table data for use in the new scheme is presented. Simplifications are employed to yield a model with only two tuning parameters. The models are validated successfully against experimental data as well as blade element momentum theory.

The preceding chapter developed a dynamic vortex theory central to the thesis. However, the theory was derived in an idealized manner where the circulation Γ could be left undetermined. It will be necessary to provide an explicit representation for the circulation. Furthermore, the model (3.9) was identified as lossless. Added realism will be made possible by the introduction of energy loss mechanisms.

Two important deleterious effects are now introduced into the model, namely *drag* and *tip-losses*. Both effects reduce the efficiency of the idealized and optimal rotor described in Chapter 3. The aim is to bring the model closer to true systems. Effective simulation is made possible by the introduction of an *equivalent airfoil* which provides an explicit form for Γ. After these developments, the model is compared to experimental data and conclusions are made.

4.1. Tip-losses

As discussed in Prandtl [56], the actuator disk rotor model implicitly assumes an infinite number of blades. The main purpose of a tip-loss correction is to bring the model closer to the true situation with a finite blade count. Note that *root-losses* could also be included. But, this effect is far less significant and hence omitted. There are several ways of including tip-losses; a simple but effective approach is used presently.

The constant circulation of the Joukowsky rotor is retained, but it is now assumed that the circulation acts over a reduced span $R_{\text{eff}} = BR$ where the *tip-loss factor* lies in the interval $0 < B < 1$. This is a standard approach in rotorcraft analysis, see Johnson [36]. Recomputing the results in Section 3.1

using a tip-loss factor yields the circulatory loadings

$$F_c(t) = \frac{\rho A B^2 N}{2\pi} \Gamma(t) \Omega(t) \tag{4.1a}$$

$$Q_c(t) = \frac{\rho A B^2 N}{2\pi} \Gamma(t) w(t) \tag{4.1b}$$

The averaged flow (1.17) must also be re-interpreted as tip-losses are introduced.

$$w(r) = \frac{1}{AB^2 N} \sum_i^N \int_0^{RB} \hat{w}(r, \theta_i, t)\ 2\pi r dr \tag{4.2}$$

All things being equal, the chief effect of the tip-loss is to increase the inflow for a given thrust. Re-deriving momentum theory over the reduced effective swept area AB^2 modifies (2.18) in the following manner

$$F = 2\rho A B^2 |w| w_i \tag{4.3}$$

The increase in inflow for a given thrust is apparent. As noted in the introduction, tip-losses have the effect of lowering the theoretically optimal power coefficient. A tip-loss corrected power coefficient is readily obtained as

$$C_P = \frac{F(w_0 - w_i)}{\frac{1}{2}\rho A w_0^3} = B^2 4 |1 - a| (1 - a) a \tag{4.4}$$

Comparison to (2.21) indicates a new *lowered* power optimum $C_P^* = B^2(16/27)$. The optimal inflow remains unchanged at $a_* = 1/3$. Johnson [36] suggest values in the range $0.96 - 0.98$ for rotorcraft applications. Similar values appears to hold for wind turbines, but skewed towards the lower end of this range. For brevity's sake the tip-loss corrected radius and area will be denoted[1] by

Model 4.1 (Tip-loss correction)**.**

$$R_p \triangleq BR, \quad A_p \triangleq \pi R_p^2 \tag{4.5}$$

4.2. The $\Gamma\Delta$-parametrization

Sectional drag forces give a significant contribution to the aerodynamic torque. Also, but to a much smaller degree, the thrust. When these non-circulatory force components are included in the model one has

$$F = F_c + F_d, \quad Q = Q_c + Q_d \tag{4.6}$$

[1] The p stands for Ludvig Prandtl (1875-1953); the originator of the theory describing tip losses.

Rather than attempting to directly integrate the drag over the blades, as is customary in blade element theory, an indirect method is used here. A drag factor Δ is introduced into the circulatory loading model (3.9) to yield the total force F and torque Q, viz.

Model 4.2 (Drag augmented interconnection structure)**.**

$$\begin{bmatrix} F \\ Q \end{bmatrix} = \frac{\rho A_p N}{2\pi} \begin{bmatrix} \Delta & -\Gamma \\ \Gamma & \Delta\ell^2 \end{bmatrix} \begin{bmatrix} w \\ -\Omega \end{bmatrix} \tag{4.7}$$

Here, ℓ[m] represents a length scale introduced for dimensional compatibility. Note that a tip-loss corrected area is used above. Dotting both sides with the generalized velocity vector col$[w,\ -\Omega]$ shows that dissipative effects have been introduced

$$\begin{bmatrix} w \\ -\Omega \end{bmatrix}^T \begin{bmatrix} F \\ Q \end{bmatrix} = \frac{\rho A_p N}{2\pi} \Delta(w^2 + (\Omega\ell)^2) \tag{4.8}$$

An opportune choice for ℓ is furnished by minimizing the difference between $\Omega\ell$ and Ωr over the reduced radius according to the formula

$$\min_{\ell\in[0,R_p]} \int_0^{R_p} (\Omega r - \Omega\ell)^2\ 2\pi r dr \quad \Rightarrow \ell = \frac{2}{3} R_p \tag{4.9}$$

This choice places ℓ at the center of mass of the triangular normal lift distribution associated with constant circulation.

Solving (4.7) for the variables Γ and Δ extracts the relationships

$$\Gamma = \frac{2\pi}{\rho A_p N} \frac{\ell^2 \Omega F + wQ}{w^2 + (\Omega\ell)^2} \tag{4.10a}$$

$$\Delta = \frac{2\pi}{\rho A_p N} \frac{wF - \Omega Q}{w^2 + (\Omega\ell)^2} \tag{4.10b}$$

The drag factor Δ extracts the lossy forces (since $wF_c - \Omega Q_c = 0$) whereas Γ extracts the lossless component (since $\ell^2\Omega F_d + wQ_d = 0$).

The circulation and drag factor have been left undetermined until now. The thrust and torque arise from blade forces which are assumed to react instantaneously to the local flow environment at the rotor disk; the circulation and drag factor should inherit this property. A simplified but credible *static* relationship on the following form is therefore sought

$$\Gamma = \Gamma(\Omega, w, \beta), \quad \Delta = \Delta(\Omega, w, \beta) \tag{4.11}$$

Since the functions are static they must also hold at steady-state, permitting the use of precomputed table-data in their identification. BEMT as introduced in Chapter 2 can be relied on to produce high quality estimates for F and Q

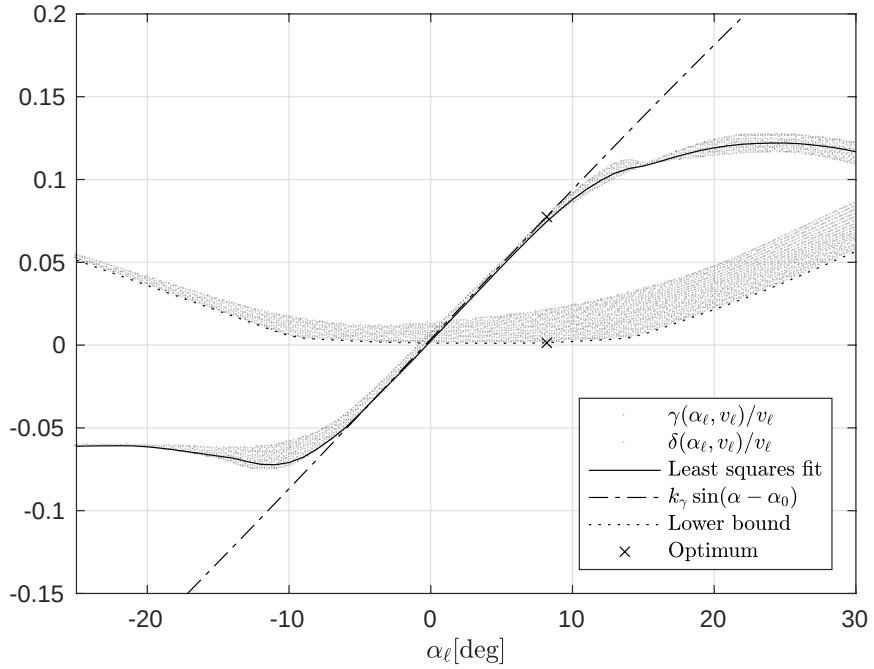

Figure 4.1.: Separation of variables for the circulation and dissipation coefficients. Here, the dots represent table-data transformed by (4.12). The point of optimal power extraction is indicated by a cross. Fits of similar quality can be obtained for other turbine variants. A tip-loss factor of $B = 0.95$ is used for the 5MW variety modeled in the figure.

at steady state. The following discussion assumes that such data are available. The dimensionless forms of (4.10) are given by

$$\gamma \triangleq \frac{\Gamma}{w_0 R} = \frac{\pi}{B^2 N} \frac{\ell_{nd}^2 \lambda C_T + (1-a) C_Q}{(1-a)^2 + (\lambda \ell_{nd})^2} \tag{4.12a}$$

$$\delta \triangleq \frac{\Delta}{w_0} = \frac{\pi}{B^2 N} \frac{(1-a) C_T - \lambda C_Q}{(1-a)^2 + (\lambda \ell_{nd})^2} \tag{4.12b}$$

Here $\ell_{nd} = \ell/R = 2B/3$. The inflow a can be computed by inverting the dimensionless tip-loss corrected inflow relation $4B^2|1-a|a = C_T$. The right hand sides in (4.12) are therefore fully known subject to available table data.

The following variables respectively describe the inflow angle and onset flow at the radial station at $r = \ell$, viz.

$$\phi_\ell \triangleq \tan^{-1}\left(\frac{w}{\Omega \ell}\right), \quad V_\ell \triangleq \sqrt{w^2 + (\Omega \ell)^2} \tag{4.13}$$

The incidence angle of a hypothetical airfoil at ℓ is obtained by subtracting the collective pitch angle.

$$\alpha_\ell = \phi_\ell - \beta \tag{4.14}$$

Let a dimensionless form of the onset flow be denoted

$$v_\ell \triangleq V_\ell / w_0 \tag{4.15}$$

An approximate separation of variables will be used to furnish explicit forms for the dimensionless coefficients γ and δ. The following relationship is assumed

$$\gamma \approx c_\gamma(\alpha_\ell)v_\ell, \quad \delta \approx c_\delta(\alpha_\ell)v_\ell \tag{4.16}$$

There is no rigorous justification for these formulae but practice reveals that they work very well. The notion of an *equivalent airfoil* arises from comparison to the formulae describing the lift and drag on a sectional airfoil of chord c located at ℓ.

$$L = \frac{1}{2}\rho c c_l(\alpha_\ell)V_\ell^2, \quad D = \frac{1}{2}\rho c c_d(\alpha_\ell)V_\ell^2 \tag{4.17}$$

Employing the Kutta-Joukowsky theorem [53] for the lift whilst furnishing an analogous expression for the drag yields the equalities

$$\rho\Gamma V_\ell = \frac{1}{2}\rho c c_l(\alpha_\ell)V_\ell^2, \quad \rho\Delta V_\ell = \frac{1}{2}\rho c c_d(\alpha_\ell)V_\ell^2 \tag{4.18}$$

Ignoring constants gives rise to expression similar to (4.16).

$$\gamma \propto c_l(\alpha_\ell)v_\ell, \quad \delta \propto c_d(\alpha_\ell)v_\ell \tag{4.19}$$

Having separated variables, the circulation and drag factor can be obtained from the formulae shown below.

Model 4.3 (Equivalent airfoil approximation)**.**

$$\Gamma = Rc_\gamma(\alpha_\ell)V_\ell, \quad \Delta = c_\delta(\alpha_\ell)V_\ell \tag{4.20}$$

While this "derivation" is quite unconvincing, the results shown in Figure 4.1 do in fact indicate the wind turbine rotor is well represented by an equivalent airfoil.

The discussion now turns to the question of how to best identify the coefficients $c_\gamma(\alpha_\ell)$, $c_\delta(\alpha_\ell)$ as well as the tip-loss factor B.

The tip-loss factor B : The tip-loss factor is set so as to *maximize the lower bound on* δ. This turns out to give values that correspond well to those found in the literature and ensures that Γ remains as unpolluted as possible by non-ideal effects. An additional benefit of this approach is that it ensures the important bound $\Delta > 0$. The optimization should be done discarding[2] data points where $a > 1/3$.

The circulation coefficient $c_\gamma(\alpha_\ell)$: The coefficient c_γ can be computed as a simple piecewise least-squares curve through the data cloud generated by the right hand side of (4.12a).

[2]Numerical tools agree well when $a \leq 1/3$ but give different results above this value due to the empirical Glauert correction.

Figure 4.2.: The Tjæreborg research turbine. Image from [74].

The dissipation coefficient $c_\delta(\alpha_\ell)$: An opportune choice for $c_\delta(\alpha_\ell)$ has turned out to be a lower bound of the right hand side of (4.12b). This scheme work wells around the optimum and represents the dissipation at high angles of incidence α_ℓ in a qualitatively acceptable manner, see Figure 4.1. The drag factor's approximation is less satisfactory than the one obtained for c_γ. The present scheme does however seem to work well in practice.

The results obtained from this approach can be seen in Figure 4.1.

4.3. Experimental validation

The true test of dynamic vortex theory, augmented with drag and tip-losses through (4.7,4.20), will be in the dynamic setting using the vortex-theoretical inflow model (3.67).

Gathering results implies that the following model should hold for the forces

$$\begin{bmatrix} F \\ Q \end{bmatrix} = \frac{\rho A_p N}{2\pi} \begin{bmatrix} \Delta & -\Gamma \\ \Gamma & \Delta\ell^2 \end{bmatrix} \begin{bmatrix} w \\ -\Omega \end{bmatrix}, \quad \Gamma = Rc_\gamma(\alpha_\ell)V_\ell, \quad \Delta = c_\delta(\alpha_\ell)V_\ell \tag{4.21}$$

The forces depend in turn on the dynamic inflow generated by a tip-loss corrected form of the wake system given in (3.67).

$$R_p \frac{d\boldsymbol{x}}{dt}(t) = |w(t)|\boldsymbol{A}\boldsymbol{x}(t) + \boldsymbol{b}\frac{F(t)}{2\rho A_p}, \quad w_i(t) = \boldsymbol{c}\boldsymbol{x}(t) \tag{4.22}$$

Table 4.1.: The Tjæreborg wind turbine in brief.

Contractor	I/S Elsam
Connected to grid (year)	1988
Hub height	60 m
Rotor diameter	$2R = 61.1\,\mathrm{m}$
Synchronous speed	$\Omega_s = 2.3415\,\mathrm{rad/s}$
Power control	Automatic variable pitch
Blade number	$N = 3$
Rated power	$E^+ = 2.2\,\mathrm{MW}$
Pitch envelope	$-2^\circ \leq \beta \leq 35^\circ$
Generator type	Synchronous induction

The model is compared to experimental data[3] gathered from the instrumented Tjæreborg wind-turbine shown in Figure 4.2. Exhaustive documentation can be found in [74]. Some key characteristics are gathered in Table 4.1.

Time-series data described in [75] is used for comparison. The data describes the mean flap moment $M_{\mathrm{flap}}(t)$, low-speed shaft torque $Q(t)$ and generator shaft power $E(t)$ as the pitch $\beta(t)$ undergoes step changes. Averaging was used to remove noise from $1P$ and $3P$ variations as well as variations in the wind speed. The data used herein therefore represents the mean over $n = 58$ identical experiments. The present model does not predict the mean-flap moment directly, so an indirect measure based on the thrust F is used. The experimental mean flap moment is extracted by averaging over strain-gauges located on each blade. Constant circulation over the reduced span R_p predicts the normal spanwise load distribution

$$f_n(r,t) = \frac{2F(t)}{NR_p^2} r \tag{4.23}$$

Integrating the normal load from the strain-gauge located at $r = R_s = 2.75\mathrm{m}$ to the effective tip at R_p permits the following estimate

$$M_{\mathrm{flap}}(t) \approx \int_{R_s}^{R_p} f_n(r,t)(r - R_s)\, dr = \frac{1}{N}\left[\ell - R_s + \frac{1}{3}\left(\frac{R_s}{R_p}\right)^2 R_s\right] F(t) \tag{4.24}$$

The low-speed shaft torque $Q(t)$ is taken directly from the model. For the present purposes the generator shaft power $E(t)$ will not be of interest. Including this quantity would require additional modeling of the generator but bring little additional insight to the table.

[3]The author wishes to thank M.O.L. Hansen of DTU for providing data.

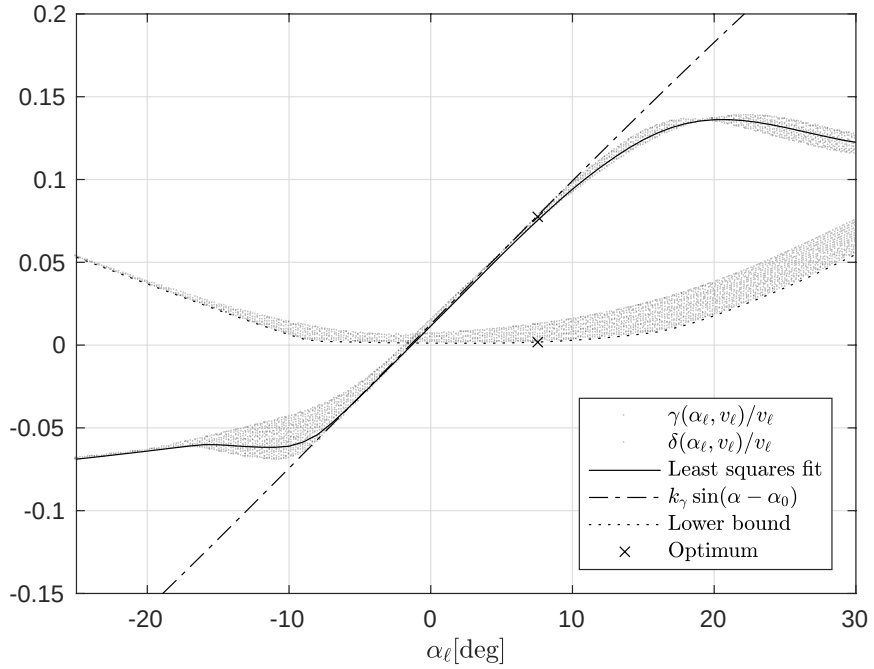

Figure 4.3.: Equivalent coefficients for the Tjæreborg wind turbine at $B = 0.965$.

The model has been tuned by setting the wind speed to $w_0 = 8.8\,\mathrm{m\,s^{-1}}$ rather than the mean wind speed of $w_0 = 8.7\,\mathrm{m\,s^{-1}}$ indicated in [75]. The pitch was also given a bias of $\beta_0 = 0.5°$ and gain increase of 10%. Other than these minor calibrations, no adjustments were made. The equivalent foil coefficients used for validation, along with the tip-loss factor, are shown in Figure 4.3. A standard variation of BEMT has been used to compute the necessary coefficient tables C_Q and C_T used in the identification of the circulation and dissipation coefficients. A 10th order fit was used to obtain the matrices in (3.67). This provides a near-perfect approximation to the underlying distributed dynamics, see Figure 3.10.

The model is compared to experimental data in Figure 4.4. Considering the simple nature of the theory, this is an encouraging result. The blind test data shown in Figure 2.7 indicate that these results are well within standard engineering accuracy for wind turbine load predictions.

The transients in the forces, ultimately arising from wake dynamics, are captured nearly perfectly. The Øye model discussed in Section 3.5.1 was developed in a semi-empirical manner based on data from the Tjæreborg turbine. Since the present model acquits itself very well, an explanation for the similarities shown in Figure 3.7 presents itself. It seems fair to conclude that the dynamic vortex theory developed in the Chapter 3 is physically sound.

A comparison of various inflow models was undertaken in Section 3.5. Here, it was noted that schemes based on the acceleration potential gave very different results than the new theory and also Øye's inflow model. It seems reasonable to

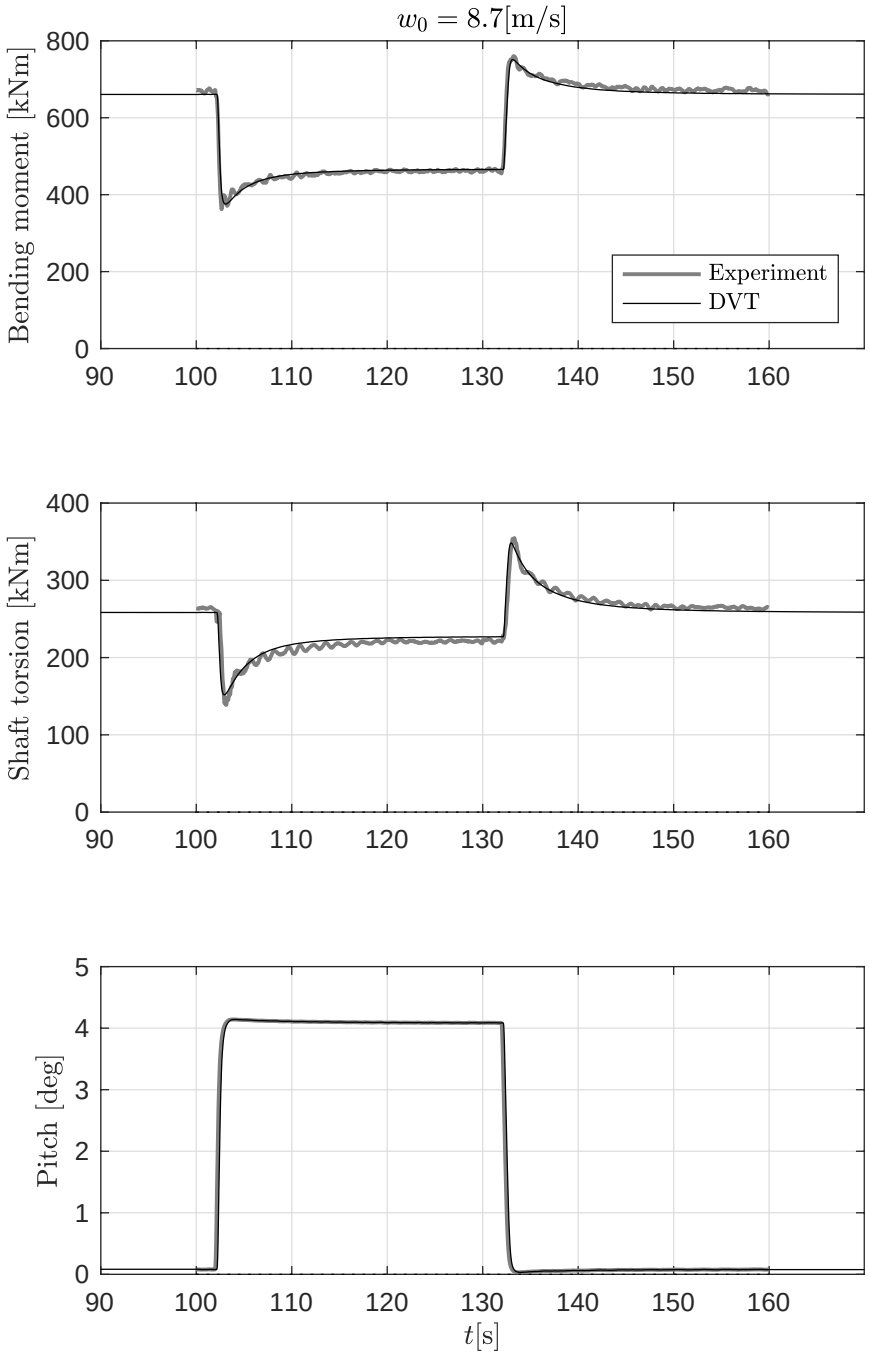

Figure 4.4.: Pitch step experiment performed at the Tjæreborg instrumented wind turbine. The experimental data is obtained by averaging over a number of identical experiments. Note that the transient behavior indicates a LHP zero; this is a dynamic wake effect.

conclude that the new theory provides a better representation of the unsteady aerodynamics. It must be noted that methods based on the acceleration potential have their genesis in helicopter analysis. One may suspect that this type of

theory is better suited for rotorcraft applications.

An indirect validation of the model at steady state is furnished by Figure 4.3 and Figure 4.1. One may argue that if BEMT theory can describe a real wind turbine accurately, so can the present model. An objection would be the deviations in the dissipation coefficient. However, this problem is minor and the drag at optimum loading is indeed well captured.

4.4. Simplification

This section undertakes a series of simplifications aimed at obtaining a parametric model for control studies.

4.4.1. The circulation function

An exceptionally useful approximation for Γ will now be discussed. Comparing the circulation formula in (4.20) to the Kutta-Joukowsky theorem whilst noting the excellent fit, suggests that the entire turbine rotor can be construed as a single airfoil located at the radial station ℓ. Since a well-designed airfoil will approximate an idealized flat-plate at small incidence angles [53], one can infer the small-angle approximation

$$c_\gamma(\alpha_\ell) \approx k_\gamma \sin(\alpha_\ell - \alpha_0), \quad \alpha_\ell \ll 1 \tag{4.25}$$

Astonishingly, a similar approximation also holds for wind turbines. See Figure 4.1 for an illustration of (4.25) and the small-angle flat-plate approximation. Simple trigonometry shows that the circulation reduces to a relation affine in w and Ω but nonlinear in the control β.

$$\Gamma = Rk_\gamma \sin(\alpha_\ell - \alpha_0)V_\ell = Rk_\gamma(\cos(\alpha_0 + \beta)w - \sin(\alpha_0 + \beta)\Omega\ell) \tag{4.26}$$

The parameters in the circulation model can be determined with an optimality argument. It was established in Chapter 2 that the wind turbine extracted a maximum amount of wind power at $C_P^* = C_P(\lambda_*, \beta_*)$. The power coefficient $C_P(\lambda, \beta)$ absorbed the effects of the inflow w_i making it possible to eliminate this variable in the specification of the optimum. However, the present model makes it explicit. It is now assumed that the optimal power coefficient is realized at the optimal inflow $a_* = 1/3$. That is, the maximum amount of shaft power $Q\Omega$ coincides with optimal extraction of power from the atmosphere $F(w_0 - w_i)$. In terms of the tip speed ratio, this implies the steady state equalities

$$w_0 = \frac{\Omega R}{\lambda_*}, \quad w_i = \frac{\Omega R}{3\lambda_*} \tag{4.27}$$

The tip-loss corrected inflow relation (4.3) can be combined with (4.1) to produce the equality

$$ww_i = \frac{N}{4\pi}\Gamma\Omega \tag{4.28}$$

It is here assumed that thrust due to drag is negligible around the optimum and that $w > 0$. The optimal inflow is realized when the circulation assumes the form

$$\Gamma_* = \frac{4\pi R}{3N\lambda_*} w \tag{4.29}$$

This implies the parameters shown below when using the simplified circulation model (4.26).

$$\alpha_0 = -\beta_*, \quad k_\gamma = \frac{4\pi}{3N\lambda_*} \tag{4.30}$$

For notational convenience, let a bias corrected input be defined by

Definition 4.1 (Bias corrected blade pitch)**.**

$$u \triangleq \beta + \alpha_0 = \beta - \beta_* \tag{4.31}$$

Now, let a function proportional to the circulation be defined by

Definition 4.2 (Circulation function)**.**

$$g(\Omega, w, u) \triangleq k(\cos(u)w - \sin(u)\Omega\ell), \quad k = \frac{2\rho A_p R}{3\lambda_*} \tag{4.32}$$

This abbreviated format permits a compact representation of the circulatory force and torque, viz.

$$F_c = g(\Omega, w, u)\Omega, \quad Q_c = g(\Omega, w, u)w \tag{4.33}$$

The point of optimal power extraction is realized at $u = 0$.

4.4.2. Dissipation

The drag factor is well approximated by a simple constant

$$c_\delta(\alpha_\ell) \approx c_0 \tag{4.34}$$

Assuming a high tip speed ratio so that $\Omega\ell/w \gg 1$ permits the following affine approximation of the dissipation factor

$$\Delta = c_0 V_\ell \approx c_0 |\Omega| \ell \tag{4.35}$$

One may proceed to give an estimate of the drag coefficient c_0. Here, a parametrization similar to the optimal control law (2.33) will be more convenient. Recall the control law

$$E(\Omega) = b\Omega^3, \quad b \triangleq \frac{1}{2}\rho A C_P^* \left(\frac{R}{\lambda_*}\right)^3 \tag{4.36}$$

The aerodynamic shaft power predicted by the simplified model reads as

$$P = \Omega Q = \Omega(Q_c + Q_d) = F_c w + Q_d \Omega = \frac{\rho A B^2 N}{2\pi}(w\Gamma\Omega - \Delta(\Omega\ell)^2) \approx \frac{\rho A B^2 N}{2\pi}(w\Gamma\Omega - c_0(\Omega\ell)^3) \quad (4.37)$$

Introduce the drag coefficient C_D via the equality

$$b_d \triangleq \frac{\rho A B^2 N}{2\pi} c_0 \ell^3 = \frac{1}{2}\rho A C_D \left(\frac{R}{\lambda_*}\right)^3 \quad (4.38)$$

Evaluating the power with (4.29) and assuming $\lambda = \lambda_*,\ w_i = w_0/3$ produces the formula

$$C_P^* = B^2 \frac{16}{27} - C_D \quad (4.39)$$

The drag coefficient in (4.38) thus quantifies the difference in the realized power coefficient C_P^* and the one predicted by tip loss corrected momentum theory. Typical wind turbines will see $C_P^* \approx 0.45 - 0.5$. With a tip loss factor of 95% one has the estimate

$$\frac{C_D}{C_P^*} \approx 10 - 20\% \quad (4.40)$$

The approximate dissipation model in torque thus reads as

Model 4.4 (Dissipative torque model)**.**

$$Q_d \approx -b_d \Omega^2, \quad b_d = \frac{1}{2}\rho A C_D \left(\frac{R}{\lambda_*}\right)^3 \quad (4.41)$$

The thrust due to drag is not well modeled by the resulting simplification given by $F_d \propto c_0 \ell |\Omega| w$ which under-predicts the force at high wind speeds. A simple drag model will be used to address this shortcoming

Model 4.5 (Drag force model)**.**

$$F_d = d|w|w, \quad d \triangleq \frac{1}{2}\rho A C_F \quad (4.42)$$

Here, C_F will be found in the range $0.01 - 0.02$. This is an exceedingly small effect compared to C_T which will lie in the interval $0 - 1$. However, predictions at high wind speeds and small incidence angles see a moderate improvement.

4.4.3. Parametric model

The preceding simplifications are aimed at control theoretical developments. However, by fine tuning the estimates a low fidelity wind turbine model suitable for fast simulation is obtained. Gathering results implies that the drag augmented interconnection structure (4.7) can be given the approximate form

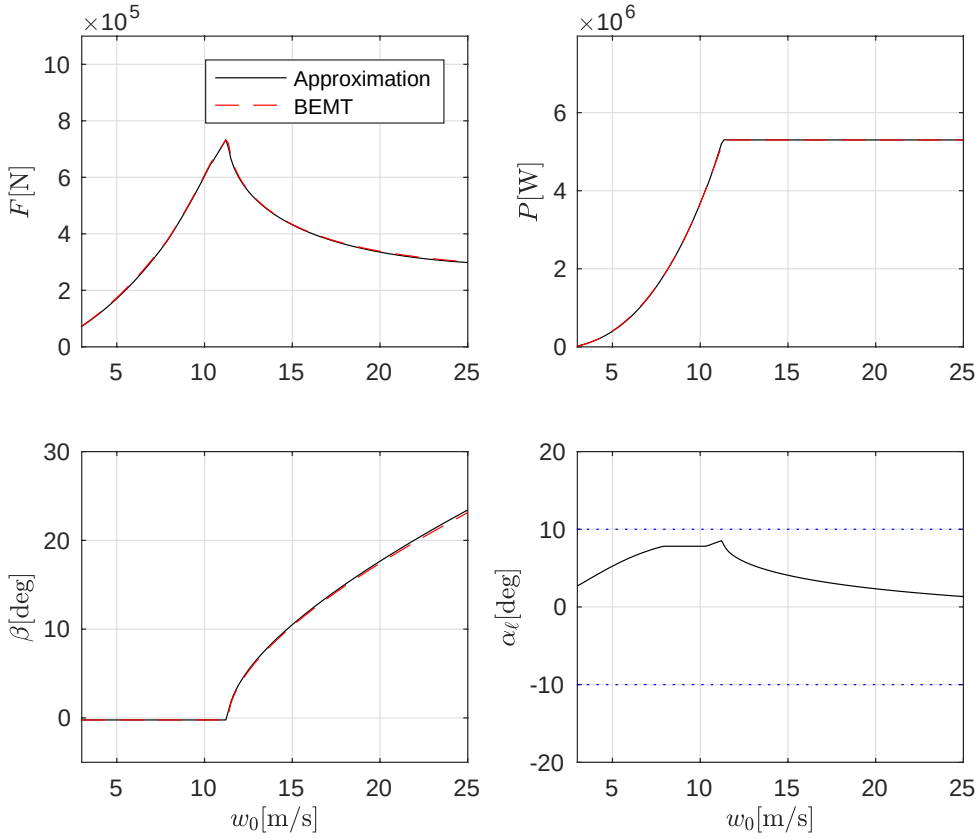

Figure 4.5.: The approximate model (4.43) compared to BEMT data. Here, the steady state thrust, power and collective pitch angle are shown as a function of wind speed. The control structure is similar to the one discussed in Chapter 2. Pitch control is active when $w_0 > 11.5\,\mathrm{m\,s^{-1}}$. The lower right figure shows the AoA at ℓ.

Model 4.6 (Parametric load model)**.**

$$\begin{bmatrix} F \\ Q \end{bmatrix} = \begin{bmatrix} d|w| & -g(\Omega, w, u) \\ g(\Omega, w, u) & b_d|\Omega| \end{bmatrix} \begin{bmatrix} w \\ -\Omega \end{bmatrix}$$

$$g(\Omega, w, u) = k(\cos(u)w - \sin(u)\Omega\ell), \quad \ell = \frac{2R_p}{3} \tag{4.43}$$

The model constants are given by

$$k = \frac{2\rho A_p R}{3\lambda_*}, \quad b_d = \frac{1}{2}\rho A\left(B^2\frac{16}{27} - C_P^*\right)\left(\frac{R}{\lambda_*}\right)^3, \quad d = \frac{1}{2}\rho A C_F \tag{4.44}$$

Finally recall that the bias corrected blade pitch was defined by the difference $u = \beta - \beta_*$. These equations represent an extremely compact model of a wind turbine rotor when used together with the tip-loss corrected low frequency DVT model (3.73) shown below.

$$\mu R_p \dot{w}_i + |w|w_i = \frac{F}{2\rho A_P} \tag{4.45}$$

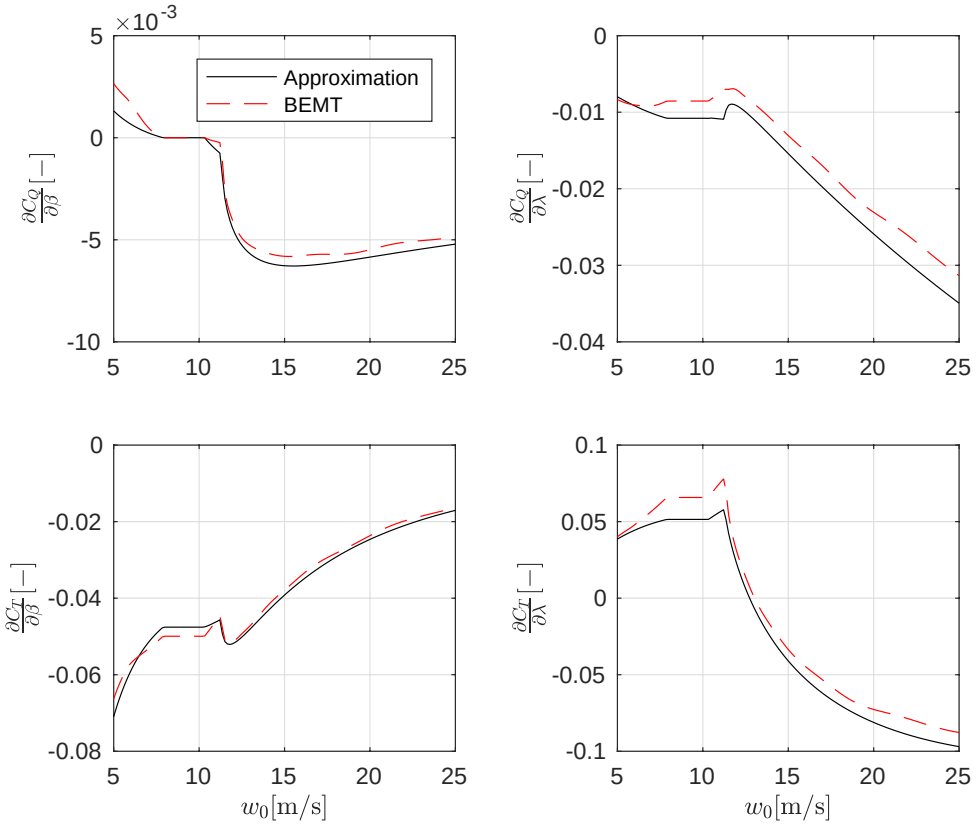

Figure 4.6.: The approximate model (4.43) compared to BEMT data. Gradients of the power and thrust coefficients with respect to the collective pitch angle and tip speed ratio are shown. Pitch control is active when $w_0 > 11.5\,\mathrm{m\,s^{-1}}$.

The model only contains two tuning parameters; the tip-loss factor B and drag coefficient C_F. The optimal point given by $C_P^* = C_P(\lambda_*, \beta_*)$ is assumed to be supplied for the specific wind turbine.

With so many assumptions and simplifications questions may be raised as to the accuracy. Figure 4.5 shows the simple model compared to steady state BEMT calculations for the 5 MW wind turbine examined in Chapter 2. Given the simplicity of the model, superb performance is obtained. The parametric model assumes operation in the linear lift regime. To examine the validity of this assumption, the angle of incidence at the radial station $\ell = 2R_p/3$ is also shown in Figure 4.5. Note that the blades remain well within the linear regime throughout; stall limits based on Figure 4.1 are indicated. Accurate pitch gradients are essential above rated wind speed. Figure 4.6 compares the DC gain w.r.t. to variations in the pitch. The pitch sensitivity is captured very well. A somewhat less ideal result is obtained for the gradients with respect to the tip speed ratio. This is of lesser significance since the generator will typically dominate the total torque gradient.

Note that the model will give significantly less satisfactory results for FSVP

wind turbines. This is due to the crude dissipation model in torque; FSVP wind turbines will turn at a nearly fixed rate of rotation implying that a constant torque $-b_d\Omega_s^2$ is applied to the shaft. Here, the full equivalent airfoil model will perform better. The model (4.43) can therefore only be recommended for VSVP wind turbines.

4.5. Chapter summary

This chapter can be summarized as follows:

- A method of representing dissipative forces was proposed in Section 4.2. An orthogonality argument was used to arrive at the $\Gamma\Delta$-parametrization which represents the thrust and torque on a vectorial format. Importantly, this parametrization makes the difference between lossless and lossy force contributions explicit.

- In Section 4.2 a simplified equivalent airfoil scheme was used to furnish explicit models for the circulation and dissipation factor discussed in Section 4.2. Whilst being approximate in nature, the scheme is capable of representing BEMT data quite well, see Figure 4.1.

- Experimental validation was undertaken Section 4.3 using data obtained from the Tjæreborg research turbine. The excellent match with the model provides strong support for the underlying theoretical framework. The equivalent airfoil model and simplified tip-loss model from Section 4.2 also seemed to acquit themselves well.

- A series of simplifications were performed in Section 4.4. The simplified model with only two tuning parameters was successfully validated against BEMT data. A trustworthy parametric loading model of a VPVS wind turbine was thus obtained.

5. System analysis

This chapter "closes the loop" and examines the interplay of the subsystems detailed in earlier chapters. Several interesting phenomena appear in the interconnected plant. Vortical motion amplification *increases the effect of platform displacements and the* circulatory reversal effect *provokes instabilities. The couplings in the interconnected plant are subtle and nonlinear in nature. A simplified small-signal analysis is undertaken to examine overall stability with and without pitch control. Several interesting lessons ensue. Floating wind turbines are shown to be intrinsically stable with a static collective pitch. On the other hand, dynamic pitch actuation leads to instabilities in the absence of nacelle motion feedforward. These instabilities can be eliminated through the use of energy shaping feedforward control.*

The previous chapters have set the stage for a new and more incisive look at the control-induced destabilization phenomena. It has been argued that circulatory loading and vortex transport are central to a full understanding of wind turbine rotors. These phenomena will also be pivotal in the design of automatic control. A block diagram of the nonlinear plant is shown in Figure 5.1. While simple at first glance, the system exhibits devious and subtle phenomena hindering simple control design. The discussion begins in Section 5.1 with a presentation of the nonlinear models governing the dynamics of the subsystems. Some interesting qualities and phenomena are also highlighted. Small signal representations are developed for a simplified stability analysis. Stability is examined in Section 5.2 and the passivity-based framework used for dynamic analysis is introduced. System stability without pitch control is examined in Section 5.2.2 and the consequences of attempting control of the angular velocity are discussed in Section 5.2.3. There, the pitfall of conventional strategies is highlighted. A solution involving feedforward is presented in Section 5.2.4. The chapter is concluded with a simulation case study found in Section 5.3.

5.1. System model

5.1.1. The rotor subsystem

The rotor subsystem Σ_Ω is the centerpiece of the full model. Here, the parametric load model (4.43) is used under an assumption of rigid shaft dynamics

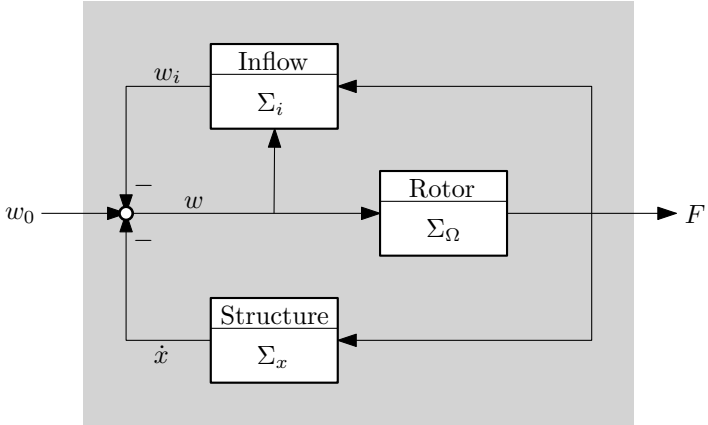

Figure 5.1.: The interconnected wind turbine system.

and a generator torque parameterized in the angular velocity. The simplified representation shown below results.

Model 5.1 (Σ_Ω: Rotor system)**.**

$$J\dot{\Omega} + Q_E(\Omega) + b_d|\Omega|\Omega = g(\Omega, w, u)w, \quad F = g(\Omega, w, u)\Omega \tag{5.1}$$

See Chapter 4 for details on the model constants and note that the very slight thrust due to drag is omitted for simplicity. Since the circulation function will be used frequently it is recounted below.

$$g(\Omega, w, u) = k(\cos(u)w - \sin(u)\Omega\ell) \tag{5.2}$$

The rotor model (5.1) works well for the variable-speed variable-pitch (VPVS) wind turbines examined in this chapter. See Figures 4.5 and 4.6 for a comparison to BEMT data at steady state. For brevity, the following shorthand is used

$$C(\Omega) \triangleq Q_E(\Omega) + b_d|\Omega|\Omega \tag{5.3}$$

The rotor subsystem (5.1) describes how the circulation g acts on the flows w and Ω to produce forces. The circulatory torque $Q_c = gw$ drives the shaft and serves as input to the internal dynamics of the subsystem. The circulatory force $F_c = g\Omega$ generates an output. Note that F_c and Q_c are closely related, a fact not apparent in table-based models like (2.26). The structure of the model is given a graphical form in Figure 5.2.

Premultiplication with Ω in (5.1) recovers the energy balance of Σ_Ω.

$$J\Omega\dot{\Omega} + \Omega C(\Omega) = Fw \tag{5.4}$$

Several interesting observations can be made from this equation. First of all, note that the approximate energy balance from Chapter 1 has been refined with

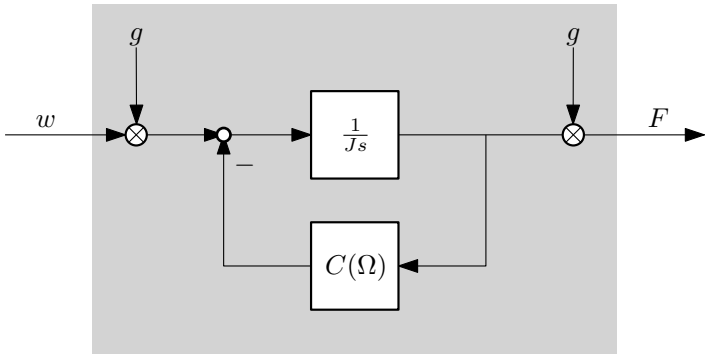

Figure 5.2.: Block diagram of the nonlinear rotor model (5.1). Note the clean structure afforded by vortex theory.

the loss mechanism $b_d|\Omega|\Omega^2$ through (5.3). Secondly, note that the circulation function g is suppressed. As discussed in Chapter 4 the circulatory forces are *lossless*. The energy balance shown above captures this quality; the circulation function g contributes to the energy budget by determining the rate by which energy flows from the atmosphere and hydroelastic system into the shaft system (or vice versa).

It will be convenient to represent the energetics of the rotor subsystem through the variable defined below.

Definition 5.1 (Storage manifold)**.**

$$\sigma \triangleq \frac{1}{2}J\Omega^2 + \int_0^t \Omega C(\Omega)\, dt' \tag{5.5}$$

The storage manifold represents the total energy stored in the rotating mass and that extracted as electricity or dissipated in friction. When $\dot{\sigma} > 0$ energy is absorbed from the surroundings. In other words, σ describes the total energy sequestered in Σ_Ω due to the work on the input/output terminals. Mathematically, one has

$$\dot{\sigma} = Fw \tag{5.6}$$

Operating regimes

The VPVS wind turbine type is examined herein. As discussed in Section 2.6, two distinct operating regimes occur in nominal operation. The rotor subsystem is the only component in the interconnected system that depends explicitly on these regions.

Region I At low wind speeds one seeks to optimize aerodynamic power extraction. This is accomplished by setting the collective pitch β to the optimal value β_* and using the MPPT control law given in (2.33). In summary

$$u = 0, \quad Q_E(\Omega) = b|\Omega|\Omega \tag{5.7}$$

The optimal value for the bias corrected input u is a matter of definition, see (4.31) and discussion for details. The aim of the torque control law is to drive the tip-speed ratio to the optimum $\lambda = \lambda_*$. Achieving this goal implies that the angular velocity Ω tracks the wind speed proportionally so that $\Omega = \lambda_* w_0 / R$.

Region II At high wind speeds two limitations are met. The available wind power scales in a cubic manner with w_0 and can be expected to exceed the electrical generating capacity above some threshold. This implies that the power absorption must be limited. Saturating the generator in power or torque gives rise to the characteristics shown below.

$$Q_E(\Omega) = \begin{cases} E_+/\Omega & \text{Power saturation} \\ Q_E^+ & \text{Torque saturation} \end{cases} \tag{5.8}$$

The former equation is suitable if power quality is of utmost importance. However, power saturation gives rise to instabilities not encountered with torque saturation.

The angular velocity Ω scales linearly with the wind speed in Region I. This property does not hold in Region II with an altered generator schedule. On VPVS turbines collective pitch control is used to drive the angular velocity to a setpoint Ω_0. In practice, this can be achieved with a PI-controller taking the measurements Ω and $\dot{\Omega}$ along with the setpoint Ω_0 into a pitch angle u. In general u will be time-varying and determined by feedback in Region II. More details will be given in Section 5.1.1.

It will be assumed that the wind turbine is operating in either of these regimes and no attention will be paid to the transition between them.

Circulatory reversal

The lossless nature of the circulatory forces gives rise to some quite counterintuitive effects that are central in the design of Region II automatic pitch control. This example aims to show that the problems faced in the design of the controller are intrinsic to the system and not the consequence of poor engineering.

Suppose that the input $w(t)$ assumes the form

$$w(t) = b + \epsilon(t) \tag{5.9}$$

where b is a constant and $\epsilon(t)$ some small variation. Assume that a regulator capable of rejecting the flow disturbance effectively is implemented. This must necessarily be achieved by suitable alterations in g.

Consider Figure 5.3. The signal to the right of the g-multiplier would approximate a constant c_{in} if no disturbances are allowed to affect the shaft dynamics. The circulation necessary to achieve this reads as

$$g(t) = \frac{c_{\text{in}}}{b + \epsilon(t)} \tag{5.10}$$

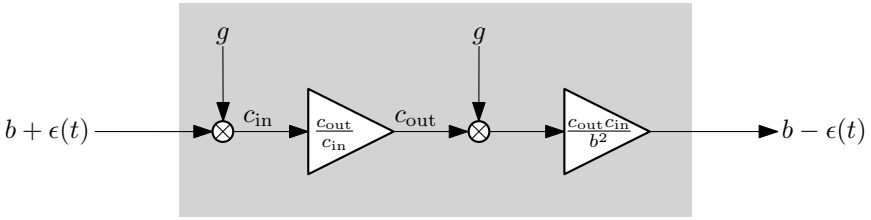

Figure 5.3.: The reversal problem associated with (5.1).

Let the signal entering the second g-multiplier be another constant c_{out}. This would be natural as no disturbances can pass the first multiplier. In Figure 5.3 this is represented by a gain. The force exiting the system reads as

$$F(t) = g(t)c_{\text{out}} = \frac{c_{\text{out}}c_{\text{in}}}{b + \epsilon(t)} \tag{5.11}$$

Summarizing, the circulatory loading associated with perfect disturbance rejection have resulted in the transformation

$$w(t) = b + \epsilon(t) \rightarrow \frac{c_{\text{out}}c_{\text{in}}}{b + \epsilon(t)} = F(t) \tag{5.12}$$

The problem becomes apparent when linearizing the exit signal. A first order expansion in ϵ shows that

$$F(t) \simeq \frac{c_{\text{out}}c_{\text{in}}}{b^2}\left(b - \epsilon(t)\right) \tag{5.13}$$

This example demonstrates one of the counterintuitive properties of circulatory loading systems. Small input perturbations will have their sign flipped at the output if rejected by regulation. All the while, the signal between the multipliers will remain unperturbed. This effect is central to control-induced destabilization. Recall that $w = w_{\text{air}} - \dot{x}$. Replacing b with the airflow and letting ϵ represent small nacelle motions shows that a positive feedback has been generated. This effect is not readily apparent from the nonlinear representation (5.1). However, the small-signal model developed below will make the problem explicit.

Small-signal model

The nonlinear nature of (5.1) is difficult to approach directly and linearization will be used to simplify the problem. To this end, let the model variables be perturbed according to the notational rule

$$\Omega(t) = \bar{\Omega} + \delta\Omega(t) \tag{5.14}$$

Here, $\bar{\Omega}$ signifies a constant operating point. Partial derivatives of g will be given the compact notation

$$g_w = \frac{\partial g}{\partial w}, \quad g_\Omega = \frac{\partial g}{\partial \Omega}, \quad g_u = \frac{\partial g}{\partial u} \tag{5.15}$$

Furthermore, let $\bar{g} = g(\bar{\Omega}, \bar{w}, \bar{u})$.

With these notational conventions, a small-signal representation of the state equation in (5.1) follows as

$$J\delta\dot{\Omega} + [C'(\bar{\Omega}) - \bar{w}\bar{g}_\Omega]\delta\Omega = (\bar{g} + \bar{g}_w\bar{w})\delta w + \bar{w}\bar{g}_u\delta u \tag{5.16}$$

$$C(\bar{\Omega}) = \bar{g}\bar{w} \tag{5.17}$$

Recall here that the effective flow w reads as the sum

$$w = w_0 - w_i - \dot{x} \tag{5.18}$$

The nacelle motion is taken as zero around the operating point so that $\dot{\bar{x}} = 0$. This implies that $\bar{w}$ in (5.16) represents the operating point at $\bar{w} = \bar{w}_0 - \bar{w}_i$.

The output equation in (5.1) is best represented in terms of the energy balance (5.6). This approach is useful since it makes the circulatory reversal explicit. Linearization leads to a meaningful representation for the output perturbation

$$\delta F = -\frac{\bar{F}}{\bar{w}}\delta w + \frac{\delta\dot{\sigma}}{\bar{w}} \tag{5.19}$$

The first term clearly captures the positive force-feedback generated by Σ_Ω. Let $\delta\dot{\sigma} = 0$. Then,

$$\frac{\delta F}{\delta\dot{x}}(s) = 1 \tag{5.20}$$

Note also that the positive feedback can be counteracted. To do this, energy must be absorbed by the rotor system in a coordinated manner so that $\delta\dot{\sigma} \propto \delta w$. However, these variations will force changes in the angular velocity as seen from

$$\delta\dot{\sigma} = J\bar{\Omega}\delta\dot{\Omega} + [C(\bar{\Omega}) + \bar{\Omega}C'(\bar{\Omega})]\delta\Omega \tag{5.21}$$

This insight is crucial to the energy shaping feedforward developed in Section 5.2.4. One may proceed to find the force equilibrium as

$$\bar{F} = \bar{g}\bar{\Omega} = \frac{\bar{\Omega}C(\bar{\Omega})}{\bar{w}} \tag{5.22}$$

Summarizing, a linearized representation of the rotor system (5.1) assumes the form shown below.

$$J\delta\dot{\Omega} + [C'(\bar{\Omega}) - \bar{w}\bar{g}_\Omega]\delta\Omega = (\bar{g} + \bar{g}_w\bar{w})\delta w + \bar{w}\bar{g}_u\delta u, \quad \delta F = -\frac{\bar{F}}{\bar{w}}\delta w + \frac{\delta\dot{\sigma}}{\bar{w}} \tag{5.23}$$

The equilibrium is given by

$$\bar{F} = \bar{g}\bar{\Omega}, \quad C(\bar{\Omega}) = \bar{g}\bar{w}, \quad \bar{F}\bar{w} = \bar{\Omega}C(\bar{\Omega}) \tag{5.24}$$

Closing the loop

It remains to "close the loop" with a pitch regulator so that δu can be determined. Instead of proposing a specific design, an indirect analysis is undertaken where the details of the control system are abstracted into a notion of what a designer *wishes to achieve*. There are many works describing detail engineering on pitch control such as the excellent book Bianchi et al. [23]. Here, the discussion is better served by remaining on a more general level.

Classical systems analysis can be used to characterize the effects of pitch control on the system in terms of the sensitivity function $S(s)$ and the complementary sensitivity function $T(s)$ [76]. The rotor model (5.23) is equipped with the following Laplace domain representation

$$\begin{aligned}\delta\Omega(s) &= G_w(s)\delta w(s) + G_u(s)\delta u(s)\\ G_w(s) &\triangleq \frac{\bar{g} + \bar{g}_w\bar{w}}{Js + C'(\bar{\Omega}) - \bar{w}\bar{g}_\Omega}, \quad G_u(s) \triangleq \frac{\bar{w}\bar{g}_u}{Js + C'(\bar{\Omega}) - \bar{w}\bar{g}_\Omega}\end{aligned} \tag{5.25}$$

Assume that a controller capable of regulating the angular velocity has been found so that the closed loop dynamics of (5.25) acquire a desirable form. A standard feedback controller will take the form

$$\delta u(s) = K(s)(\delta\Omega_r(s) - \delta\Omega(s)) \tag{5.26}$$

The resulting loop-transfer function follows as

$$L(s) = K(s)G_u(s) \tag{5.27}$$

Closing the loop one has

$$\delta\Omega(s) = T(s)\delta\Omega_r(s) + S(s)G_w(s)\delta w(s) \tag{5.28}$$

The sensitivity functions are here given by

$$T(s) = \frac{L(s)}{1 + L(s)}, \quad S(s) = \frac{1}{1 + L(s)} \tag{5.29}$$

As seen from (5.28) the complementary sensitivity function $T(s)$ characterizes the control system's ability in tracking a reference signal. The sensitivity function $S(s)$ determines how well disturbances are rejected. These functions depend on the particulars of the plant and regulator. For the system at hand, the pitch input could be driven by a PI-regulator producing a second order system when accounting for the first order shaft dynamics. A robust design example is given by

$$L(s) = \frac{1}{s}\frac{\omega_b}{(s/\omega_b) + 2\zeta}, \quad T(s) = \frac{\omega_b^2}{s^2 + 2\zeta\omega_b s + \omega_b^2}, \quad S(s) = \frac{s^2 + 2\zeta\omega_b s}{s^2 + 2\zeta\omega_b + \omega_b^2} \tag{5.30}$$

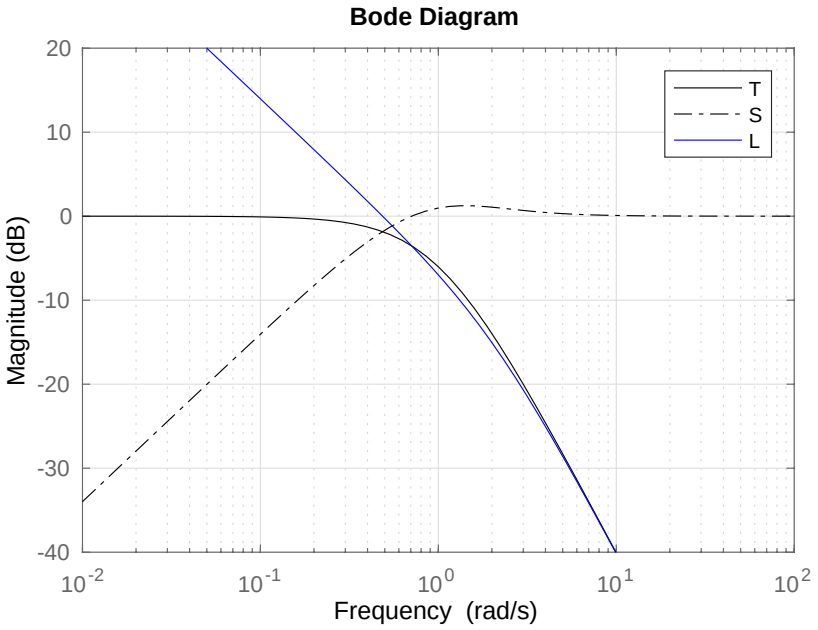

Figure 5.4.: Central transfer functions in a control system. Respectively; the complementary sensitivity function T, the sensitivity function S and the loop transfer function L. The transfer functions (5.30) with $\omega_b = 1$ and $\zeta = 1$ are shown here.

See Figure 5.4 for an illustration. The loop shaping design shown in the figure achieves a 40 dB/dec roll-off at high frequencies whilst ensuring that the complementary sensitivity function achieves $T(s) \simeq 1$ for frequencies below the bandwidth denoted by ω_b. Since $T(s) + S(s) = 1$ this also implies good disturbance rejection with $S(s) \simeq 0$. The control system rolls off above the bandwidth in order to mitigate high frequency control use and reduce the effects of measurement noise. Above the controller bandwidth one has $S(s) \simeq 1$ and $T(s) \simeq 0$. A well designed wind turbine system will be equipped with relations of this kind.

Having determined the dynamics of the angular velocity in closed loop one may proceed to examine the perturbed output δF whose Laplace domain representation reads as

$$\delta F(s) = -\frac{\bar{F}}{\bar{w}}\delta w(s) + \frac{s}{\bar{w}}\delta\sigma(s) \tag{5.31}$$

Linearizing (5.5) leads to the following Laplace model for perturbations in the storage manifold

$$\delta\sigma(s) \triangleq \mathcal{E}(s)\delta\Omega(s), \quad \mathcal{E}(s) \triangleq \frac{J\bar{\Omega}s + \bar{\Omega}C'(\bar{\Omega}) + C(\bar{\Omega})}{s} \tag{5.32}$$

It thus holds that

$$\delta\sigma(s) = \mathcal{E}(s)T(s)\delta\Omega_r(s) + S(s)\mathcal{E}(s)G_w(s)\delta w(s) \tag{5.33}$$

The product $\mathcal{E}(s)G_w(s)$ deserves special attention. In open loop, variations in the storage manifold follow from $\delta\sigma(s) = \mathcal{E}(s)G_w(s)\delta w(s)$. This equation also serves as a decent estimate past roll-off where $\omega \gg \omega_b$. Here, one may use the approximations $S \simeq 1$ and $|T| \ll 0$ giving $\delta\sigma(s) \simeq \mathcal{E}(s)G_w(s)\delta w(s)$.

Let three constants be defined by

$$k_1 \triangleq \frac{1 + (\bar{g}_w\bar{w})/\bar{g}}{2}, \quad k_2 \triangleq \frac{C(\bar{\Omega}) + \bar{w}\bar{g}_\Omega\bar{\Omega}}{J\bar{\Omega}}, \quad k_3 \triangleq \frac{C'(\bar{\Omega}) - \bar{w}\bar{g}_\Omega}{J} \tag{5.34}$$

Using the equilibrium $\bar{F} = \bar{g}\bar{\Omega}$ it is possible to rewrite the numerator in $G_w(s)$ in the following manner

$$\bar{g} + \bar{g}_w\bar{w} = 2\bar{g}\frac{1 + (\bar{g}_w\bar{w})/\bar{g}}{2} = \frac{2\bar{F}}{\bar{\Omega}}k_1 \tag{5.35}$$

A simple algebraic development involving (5.32) will reveal that the open loop response can be given the compact form

$$G_w(s) = \frac{2\bar{F}}{s\mathcal{E}(s)}\left(1 + \frac{k_2}{s + k_3}\right)k_1 \tag{5.36}$$

The constants in (5.34) can be estimated using the parametric model and invoking reasonable assumptions.

Bound 1: ($k_1 \geq 1$) A standing assumption will be that pitch-to-feather is utilized. This is the standard solution on utility grade VPVS wind turbines and permits the following bound to be established.

$$0 \leq u \leq \pi/2 \tag{5.37}$$

Recall that $g = k(\cos(u)w - \sin(u)\ell\Omega)$. Under assumption (5.37) the following bounds hold

$$\bar{g}_\Omega = -k\ell\sin(\bar{u}) \leq 0, \quad \bar{g}_w\bar{w} = k\cos(\bar{u})\bar{w} \geq \bar{g} \tag{5.38}$$

It follows that

$$k_1 \geq 1 \tag{5.39}$$

Bound 2: ($k_2 \geq 0$) Noting the equilibrium $C(\bar{\Omega}) = \bar{g}\bar{w}$ recounted in (5.23) one must ascertain the bound $\bar{g} + \bar{g}_\Omega\bar{\Omega} \geq 0$. The relative flux is assumed positive implying $\bar{w} > 0$. When pitch to feather is utilized so that (5.37) holds, a criterion equivalent to $\bar{g} + \bar{g}_\Omega\bar{\Omega} \geq 0$ based on (5.2) can be given as

$$\tan^{-1}\left(\frac{w}{2\Omega\ell}\right) \geq u \tag{5.40}$$

The explicit computation illustrated in Figure 5.5 provides anecdotal evidence that the inequality $g + g_\Omega\Omega \geq 0$ holds robustly for many modern three blade VPVS types (granted that the system operates close to an equilibrium point). The bound (5.40) will be assumed to hold herein. The following inequality has thus been justified

$$k_2 \geq 0 \tag{5.41}$$

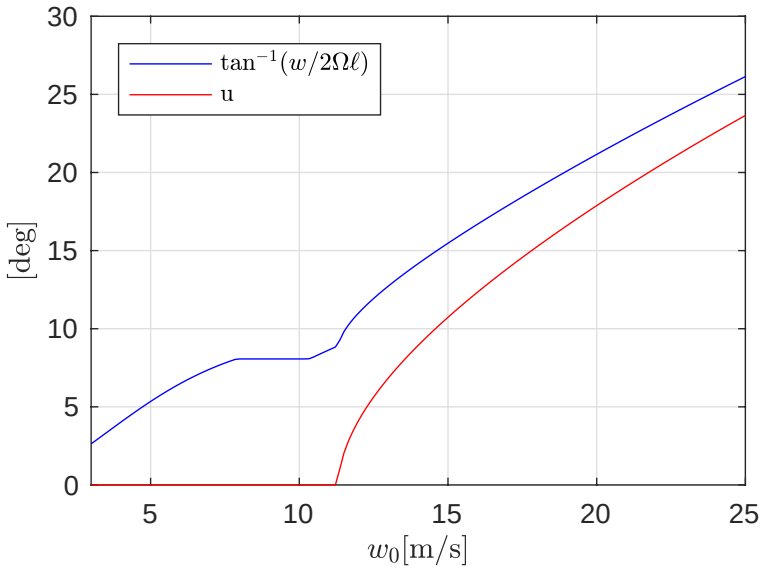

Figure 5.5.: Curves representing the inequality (5.40). The difference $g + g_\Omega \Omega$ is positive wherever the blue line upper bounds the red curve. Equilibria of a representative wind turbine [13] are used to generate the figure.

Bound 3: ($k_3 \geq 0$) Noting $C'(\bar{\Omega}) = Q'_E(\Omega) + 2b_d|\Omega|$ from (5.3) and $\bar{g}_\Omega \leq 0$ from (5.38) one must require a non-negative slope on the generator characteristic. With recourse to Section 2.6, this is satisfied by all the examples covered in the discussion on torque schedules save for the constant power strategy (2.34). Assuming $Q'_E(\Omega) \geq 0$ one has

$$k_3 \geq 0 \tag{5.42}$$

Gathering results gives rise to a simple Laplace domain model capable of representing the rotor subsystem in open and closed loop operation.

Model 5.2 (Linearized rotor model)**.**
Dynamics:

$$\delta\Omega(s) = T(s)\delta\Omega_r(s) + S(s)G_w(s)\delta w(s) \tag{5.43}$$

$$\delta F(s) = -\frac{\bar{F}}{\bar{w}}\delta w(s) + \frac{s}{\bar{w}}\mathcal{E}(s)\delta\Omega(s) \tag{5.44}$$

Transfer functions:

$$\mathcal{E}(s) \triangleq \frac{J\bar{\Omega}s + \bar{\Omega}C'(\bar{\Omega}) + C(\bar{\Omega})}{s}, \quad G_w(s) = \frac{2\bar{F}}{s\mathcal{E}(s)}\left(1 + \frac{k_2}{s + k_3}\right)k_1 \tag{5.45}$$

Regime specific models

The general nature of $T(s)$ and $S(s)$ suggest that a simplified approach is taken. Two cases will given special attention.

Case 1: Open loop In the absence of control $K(s) = 0$ one has $S(s) = 1$ and $T(s) = 0$. It follows that

$$\delta\Omega(s) = \frac{2\bar{F}}{s\mathcal{E}(s)}\left(1 + \frac{k_2}{s+k_3}\right)k_1\delta w(s) \tag{5.46}$$

$$\delta F(s) = \frac{\bar{F}}{\bar{w}}\left(2k_1 - 1 + \frac{2k_1k_2}{s+k_3}\right)\delta w(s) \tag{5.47}$$

Case 2: Effective control A high bandwidth ω_b is assumed. The response to excitations in the frequency band $\omega \ll \omega_b$ are well modeled by $T(s) \simeq 1$ and $S(s) \simeq 0$. This leads to the estimates

$$\delta\Omega(s) \simeq \delta\Omega_r(s) \tag{5.48}$$

$$\delta F(s) \simeq -\frac{\bar{F}}{\bar{w}}\delta w(s) + \frac{s}{\bar{w}}\mathcal{E}(s)\delta\Omega_r(s) \tag{5.49}$$

Note well that Case 1 avoids the destabilizing feedback from $\dot{x}$ indicated in (5.20). In open loop, sufficient variations in the storage manifold σ are generated by disturbances δw. Such disturbances are suppressed in Case 2 giving rise to a destabilizing feedback. In other words, the latter case sets up conditions for the circulatory reversal problem described above. From (5.32) one has

$$\delta\sigma(s) = \frac{2\bar{F}}{s}\left(1 + \frac{k_2}{s+k_3}\right)k_1\delta w(s) \qquad \text{(Case 1)} \tag{5.50a}$$

$$\delta\sigma(s) = \mathcal{E}(s)\delta\Omega_r(s) \qquad \text{(Case 2)} \tag{5.50b}$$

Note that closed loop operation with effective control renders σ constant lest one varies the reference signal. Doing this will in fact be necessary for stability as shown in Section 5.2.4.

5.1.2. The wake subsystem

The rotor subsystem operates in closed loop with the structural model detailed in Appendix A and the wake model from Chapter 3. For the analysis in this chapter, the low frequency approximation of the wake dynamics (3.73) will be used with the understanding that it under-predicts energy dissipation at high frequency perturbations.

Model 5.3 (Σ_i: Wake system)**.**

$$\mu R_p\dot{w}_i + |w|w_i = \frac{F}{2\rho A_p} \tag{5.51}$$

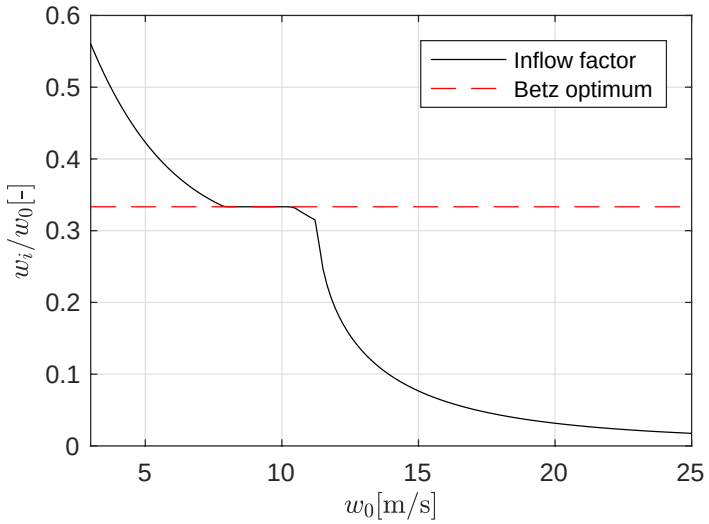

Figure 5.6.: The inflow factor as a function of wind speed on a pitch controlled wind turbine. Pitch control is active at wind speeds exceeding $w_0 > 11.5\,\mathrm{m\,s^{-1}}$. Power is limited here and the inflow will decrease from the Betz optimum at $a = 1/3$. At low wind speeds very high inflow factors may be experienced.

The model depends on the relative flux w giving rise to the vertical branch seen in Figure 5.1. Notably, nacelle motion $\dot{x}$ enters the dynamics.

The inflow model is equipped with a time constant on the order $\tau_i \sim R_p/w_0$. With a 5 MW wind turbine, a rough estimate based on a linearized model can be given as $2\,\mathrm{s} < \tau_i < 14\,\mathrm{s}$. The approximate lower bound is encountered at very high wind speeds and low thrust coefficients whereas the upper estimate is associated with optimal power extraction. The corner frequency of the wake will thus lie in the approximate range $0.04\,\mathrm{rad\,s^{-1}} < \omega_i < 0.5\,\mathrm{rad\,s^{-1}}$.

Recalling from Chapter 2 that the inflow will acquire magnitudes on the order $\sim w_0/3$ implies that an accurate inflow model is crucial for understanding the dynamics of large wind turbines. A smaller wind turbine with radius $R' < R$ will, at the same wind speed, have time constants described by $\tau_i' = (R'/R)\tau_i$. All else being equal, smaller wind turbines will see inflow dynamics with higher corner frequencies. A quasistatic assumption taking $\mu = 0$ may thus be suitable for small WTG types; not the modern breed of multi MW machines. The wake dynamics take place at time-scales comparable to platform motion and should not be neglected through a quasi-static approximation or similar simplifications.

The inflow factor $a = w_i/w_0$ quantifies the relation between the wind speed and the flow disturbance due to force application. Figure 5.6 illustrates how this quantity varies over the operating envelope of a VPVS wind turbine. Below rated wind speed the inflow may acquire large values, particularly in the start-up region where the rotor speed is kept constant. However, the bound $a < 0.8$ is unlikely to be exceeded. At high wind speeds where pitch control is active the lower bound $a < 1/3$ applies.

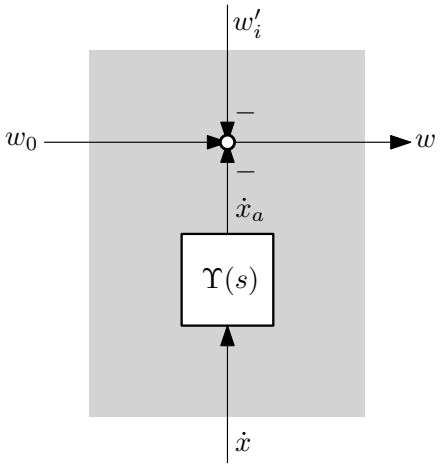

Figure 5.7.: The wake effect.

Vortical motion amplification

It is now assumed that the relative flux is positive $w > 0$ as is always verified in practice. The dynamic wake model (5.51) representing the vortical wake can be given on an alternative form that illustrates how $\dot{x}$ perturbs the inflow.

$$\mu R_p \dot{w}_i + (w_0 - w_i)w_i = \frac{F}{2\rho A_p} + w_i \dot{x} \tag{5.52}$$

Let a nominal wake model unperturbed by nacelle motion read as

$$\mu R_p \dot{w}_i' + (w_0 - w_i')w_i' = \frac{F}{2\rho A_p} \tag{5.53}$$

By decomposing the inflow into two constituents $w_i = w_i' + \xi$ it is possible to perform an approximate superposition using the nominal model along with a *motion amplification* system. See Figure 5.7. To first order in $\dot{x}$ and ξ one finds that

$$\mu R_p \dot{\xi} + (w_0 - 2w_i)\xi = w_i \dot{x} \tag{5.54}$$

At optimum loading with $w_i = w_0/3$ the DC-gain of this plant is unity. This means that the wake will amplify the effects of low-frequency nacelle motion by as much as 100% under nominal operation. The amplified motion $\dot{x}_a$ can be represented in the Laplace domain by

$$\dot{x}_a(s) \triangleq \dot{x}(s) + \xi(s) = \Upsilon(s)\dot{x}(s), \quad \Upsilon(s) \triangleq \frac{s\mu R_p + (\bar{w}_0 - \bar{w}_i)}{s\mu R_p + (\bar{w}_0 - 2\bar{w}_i)} \tag{5.55}$$

Subject to the requirement $w_i \leq w_0/3$ the following bounds hold

$$-19.5^\circ < \angle\Upsilon(\jmath\omega) \leq 0, \quad 1 \leq |\Upsilon(\jmath\omega)| \leq 2 \tag{5.56}$$

It is seen that the vortical wake acts, to close approximation, as a simple gain on the nacelle motion. Physically, the amplification arises as the vortex loops in the wake are packed more closely when moving the rotor backwards[1] and spread out as the rotor moves forwards. The inflow depends on the density of the downstream vortex distribution and this is captured by the model.

The crucial insight is that positive feedbacks in $\dot{x}$ actually act on $\dot{x}_a$. Correcting measures must account for this effect. In practice, this will imply higher feedforward corrections (up to $2\times$) from $\dot{x}$ than a simple analysis omitting wake dynamics would suggest.

Small-signal model

It will be convenient to use the modified force introduced in Chapter 3. Recalling (3.62) this input describes the imbalance in applied force and momentum flux.

$$\tilde{F} \triangleq F - 2\rho A_p |w| w_i \tag{5.57}$$

The modified force vanishes at steady state in accordance with Rankine-Froude momentum theory, see Chapter 2. With this device, (5.51) reduces to a linear plant thus obviating the need for linearization in the first place.

Model 5.4 (Σ_i': Modified wake system)**.**

$$2\mu\rho A_p R_p \dot{w}_i = \tilde{F} \tag{5.58}$$

One may proceed to determine the equilibrium

$$\bar{\tilde{F}} = \bar{F} - 2\rho A_p |\bar{w}| \bar{w}_i = 0 \tag{5.59}$$

and the associated perturbation

$$\delta\tilde{F} = \delta F - \frac{\bar{F}}{\bar{w}} \left[\delta w_0 - \delta\dot{x} - \left(2 - \frac{1}{\bar{a}} \right) \delta w_i \right] \tag{5.60}$$

Here, $\bar{a} = \bar{w}_i / \bar{w}_0$ describes the inflow factor at the operating point.

5.1.3. Vectorial model

The modified force $\tilde{F}$ can be obtained by equipping the rotor model Σ_Ω with an additional output. The additional force signal $\tilde{F}$ gives rise to a force vector defined by

$$\boldsymbol{f} \triangleq \begin{bmatrix} F \\ \tilde{F} \end{bmatrix} \tag{5.61a}$$

[1] Towards the trailing wake tube.

It will be desirable to retain a square structure for Σ_Ω necessitating the definition of an augmented input. To this end, a flow vector will be defined by

$$\boldsymbol{w} \triangleq \begin{bmatrix} w_0 - \dot{x} \\ -w_i \end{bmatrix} \tag{5.61b}$$

The negative signs on $\dot{x}$ and w_i in $\boldsymbol{w}$ reflect the negative feedback seen in Figure 5.1.

Letting the force vector perturb as $\boldsymbol{f}(t) = \bar{\boldsymbol{f}} + \delta\boldsymbol{f}(t)$ and recalling (5.23) leads to an extended force model neatly incorporating the nonlinearities of the dynamic wake model.

$$\delta\boldsymbol{f} = \frac{\bar{F}}{\bar{w}}\left(\boldsymbol{D}_0\delta\boldsymbol{w} + \begin{bmatrix} 1 \\ 1 \end{bmatrix}\frac{\delta\dot{\sigma}}{\bar{F}}\right), \quad \boldsymbol{D}_0 \triangleq -\begin{bmatrix} 1 & 1 \\ 2 & 3-\bar{a}^{-1} \end{bmatrix} \tag{5.62}$$

Several items are worthy of notice. The off-diagonal elements in the matrix $\boldsymbol{D}_0$ relating $\delta\boldsymbol{w}$ and $\delta\boldsymbol{f}$ represent couplings between the wake and nacelle motion. On the first diagonal element one finds the reversal effect discussed in Section 5.1.1 whereas the second element is associated with wake damping. This element is negative under nominal operation at optimal and suboptimal power extraction, i.e. $\bar{a} \leq 1/3$. The rotor's angular velocity enters the force vector through the last term.

Specializing to the open loop Case 1 with (5.50) leads to the following Laplace-domain force model

$$\delta\boldsymbol{f}(s) = \frac{\bar{F}}{\bar{w}}\left(\boldsymbol{D}_1 + \frac{2k_1k_2}{s+k_3}\begin{bmatrix} 1 & 1 \\ 1 & 1 \end{bmatrix}\right)\delta\boldsymbol{w}(s)$$

$$\boldsymbol{D}_1 \triangleq \begin{bmatrix} 2k_1 - 1 & 2k_1 - 1 \\ 2k_1 - 2 & 2k_1 + \bar{a}^{-1} - 3 \end{bmatrix} \quad \text{(Case 1)} \tag{5.63}$$

The closed loop Case 2 gives rise to the following expression

$$\delta\boldsymbol{f}(s) = \frac{\bar{F}}{\bar{w}}\left(\boldsymbol{D}_0\delta\boldsymbol{w}(s) + \frac{s\mathcal{E}(s)}{\bar{F}}\begin{bmatrix} 1 \\ 1 \end{bmatrix}\delta\Omega_r(s)\right) \qquad \text{(Case 2)} \tag{5.64}$$

The force vector $\boldsymbol{f}$ perturbs the hydroelastic system through the first element F and the modified wake dynamics through the second element $\tilde{F}$. The hydroelastic module Σ_x is described in Appendix A. There, a linear model relating the thrust force F to nacelle motion $\dot{x}$ is found.

Model 5.5 (Σ_x: Hydroelastic module)**.**

$$\dot{x}(s) = H(s)F(s) \tag{5.65}$$

As discussed in Appendix A the model $H(s)$ is output strictly passive. More will be said on this later. For now, it suffices to note that the modified wake

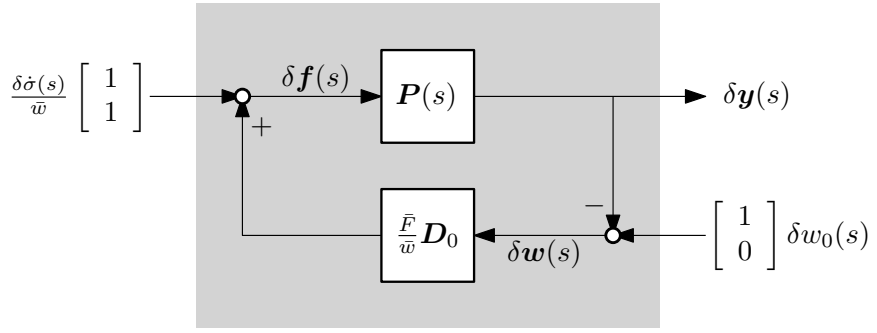

Figure 5.8.: The vectorial model represented in the Laplace domain. Variations in the storage manifold $\delta\sigma$ associated with cases 1 and 2 can be found in (5.50).

model (5.58) can be represented by a passive transfer function just like the the hydroelastic system.

$$\dot{w}_i(s) = W(s)\tilde{F}(s), \quad W(s) \triangleq \frac{1}{2\mu\rho A_p R_p s} \tag{5.66}$$

It is well known that integrators like $W(s)$ may be categorized as lossless passive systems [21]. The linear models describing hydroelastics and the modified wake dynamics are conveniently arrayed by defining the following vector

$$\boldsymbol{y} \triangleq \begin{bmatrix} \dot{x} \\ w_i \end{bmatrix} \tag{5.67}$$

Now, the response of the wake and support structure may be represented by

$$\boldsymbol{y}(s) = \boldsymbol{P}(s)\boldsymbol{f}(s), \quad \boldsymbol{P}(s) \triangleq \mathrm{diag}[H(s), W(s)] \tag{5.68}$$

The definition of $\boldsymbol{f}$ can be found in (5.61). Combining (5.68) with the extended force model (5.62) gives rise to the small-signal feedback structure depicted in Figure 5.8.

5.2. Stability

This section examines stability of the interconnected wind turbine system. The workhorse of the stability analysis will be *passivity theory* based on the dynamics illustrated in Figure 5.8. The model subdivision shown in the figure is chosen for a very specific reason. It turns out that $\boldsymbol{P}(s)$ is *passive* implying that

$$\int_0^\tau \delta\boldsymbol{f}^T(t)\delta\boldsymbol{y}(t)\, dt \geq -\alpha \tag{5.69}$$

Physically, this equation indicates that the energy delivered over the input/output terminals must be *positive*[2]. In other words, no net energy can be delivered to

[2]The α accounts for nonzero initial conditions.

the surroundings, hence the notion of "passive". Recall that $\boldsymbol{P}(s)$ contains the modified wake dynamics and the hydroelastic module on its diagonal according to its definition in (5.68). The modified wake dynamics (5.58) are indeed passive as demonstrated in Section 3.3.1. The hydroelastic system satisfies a stronger property known as output strict passivity. This is demonstrated in Appendix A.2.1. In light of this property note that the inequality (5.69) is somewhat conservative since it disregards internal damping in the hydroelastic system.

5.2.1. Input/output stability

Input-output stability theory is a very useful approach for dealing with interconnected systems. The theory considers systems of the type shown below.

$$\boldsymbol{y} = \boldsymbol{H}\boldsymbol{u} \tag{5.70}$$

Input/output methodologies concern themselves with the relationship between the input $\boldsymbol{u}$ and the attendant output $\boldsymbol{y}$ of some system $\boldsymbol{H}$. It is here assumed that $\boldsymbol{H}$ is an $n \times n$ square system with an equal number of inputs and outputs. Note that $\boldsymbol{H}$ can be nonlinear and time-varying.

It is customary to consider inputs drawn from an $\mathcal{L}_p$-space defined by

$$\|\boldsymbol{u}\|_p = \left(\sum_i \int_0^\infty |u_i(t)|^p \, dt \right)^{\frac{1}{p}} < \infty, \quad p \geq 1 \tag{5.71}$$

If the integral exists then $\boldsymbol{u}(t) \in \mathcal{L}_p$ and the signal is informally referred to as "well behaved". If the output belongs to the same space as the input then $\boldsymbol{H}$ describes an $\mathcal{L}_p$-stable system. In other words, the output is well behaved. It is often necessary to consider signals that do not pass the strict criterion imposed above. To this end, define the truncation operator

$$\boldsymbol{u}_\tau(t) = \begin{cases} \boldsymbol{u}(t) & 0 \leq t \leq \tau \\ 0 & t > \tau \end{cases} \tag{5.72}$$

The idea is that unbounded signals such as $u(t) = t$ may imply $u(t) \notin \mathcal{L}_p$ whereas a truncated signal will result in $u_\tau(t) \in \mathcal{L}_p$. I/O stability can now be characterized by

Definition 5.2 (Finite-gain stable)**.** *A system $\boldsymbol{H}$ is finite-gain $\mathcal{L}_p$-stable if there exists nonnegative constants γ (gain) and β (bias) such that*

$$\|\boldsymbol{y}_\tau\|_p \leq \gamma \|\boldsymbol{u}_\tau\|_p + \beta \tag{5.73}$$

for all $\boldsymbol{u}_\tau \in \mathcal{L}_p$ and $\tau \geq 0$.

The choice of norm is dictated by the application. In this work, special emphasis will be placed on the $\mathcal{L}_2$-space defined by

$$\|\boldsymbol{u}\|_2^2 = \int_0^\infty \boldsymbol{u}^T(t)\boldsymbol{u}(t)\ dt < \infty \tag{5.74}$$

It will be useful to introduce the specialized notation shown below.

$$\langle \boldsymbol{u}, \boldsymbol{v} \rangle_\tau = \int_0^\tau \boldsymbol{u}^T(t)\boldsymbol{v}(t)\ dt \tag{5.75}$$

Note that the truncation operator permits the equivalent statements

$$\langle \boldsymbol{u}, \boldsymbol{v} \rangle_\tau = \langle \boldsymbol{u}, \boldsymbol{v}_\tau \rangle = \langle \boldsymbol{u}_\tau, \boldsymbol{v} \rangle = \langle \boldsymbol{u}_\tau, \boldsymbol{v}_\tau \rangle \tag{5.76}$$

The criterion for set membership $\boldsymbol{u}_\tau \in \mathcal{L}_2$ now acquires the compact formulation $\langle \boldsymbol{u}, \boldsymbol{u} \rangle_\tau < \infty$. Note furthermore that $\mathcal{L}_2$ stability can be established by

$$\|\boldsymbol{y}_\tau\|_2^2 = \langle \boldsymbol{y}, \boldsymbol{y} \rangle_\tau \leq \gamma^2 \langle \boldsymbol{u}, \boldsymbol{u} \rangle_\tau + \beta^2 \leq (\gamma \|\boldsymbol{u}_\tau\|_2 + \beta)^2 \tag{5.77}$$

Taking the square root on both sides establishes that

$$\|\boldsymbol{y}_\tau\|_2 \leq \gamma \|\boldsymbol{u}_\tau\|_2 + \beta \tag{5.78}$$

Interconnected systems

I/O-stability theory is well-suited for the analysis of feedback systems. Let two subsystems be represented by

$$\boldsymbol{y}_1 = \boldsymbol{H}_1 \boldsymbol{u}_1, \quad \boldsymbol{y}_2 = \boldsymbol{H}_2 \boldsymbol{u}_2 \tag{5.79}$$

Consider now the feedback interconnection shown below

$$\boldsymbol{u}_1 = \boldsymbol{d}_1 - \boldsymbol{y}_2, \quad \boldsymbol{u}_2 = \boldsymbol{d}_2 + \boldsymbol{y}_1 \tag{5.80}$$

The dynamics of the interconnected plant satisfies

$$\boldsymbol{y}_1 = \boldsymbol{H}_1(\boldsymbol{d}_1 - \boldsymbol{y}_2), \quad \boldsymbol{y}_2 = \boldsymbol{H}_2(\boldsymbol{d}_2 + \boldsymbol{y}_1) \tag{5.81}$$

Define the joint input and output respectively by

$$\boldsymbol{d} \triangleq \begin{bmatrix} \boldsymbol{d}_1 \\ \boldsymbol{d}_2 \end{bmatrix}, \quad \boldsymbol{y} \triangleq \begin{bmatrix} \boldsymbol{y}_1 \\ \boldsymbol{y}_2 \end{bmatrix} \tag{5.82}$$

It is natural to ask whether the interconnected plant is input-output stable. There are (at least) two routes towards an answer; the small-gain approach and the passivity approach. The former route will not be used herein and attention will be focused on passivity theory. The property is defined below.

Definition 5.3 (Passivity [16])**.**
Let $\boldsymbol{y} = \boldsymbol{H}\boldsymbol{u}$ represent a system with an equal number of inputs and outputs. Suppose that the following inequality holds with ϱ, ν and α being real constants.

$$\langle \boldsymbol{y}, \boldsymbol{u} \rangle_\tau \geq \varrho \langle \boldsymbol{y}, \boldsymbol{y} \rangle_\tau + \nu \langle \boldsymbol{u}, \boldsymbol{u} \rangle_\tau - \alpha \tag{5.83}$$

Let $\alpha \geq 0$. The following passivity properties are said to hold for $\boldsymbol{H}$.

Passive: *$\nu \geq 0$ and $\varrho \geq 0$.*

Input strictly passive: *$\nu > 0$ and $\varrho \geq 0$.*

Output strictly passive: *$\varrho > 0$ and $\nu \geq 0$.*

Very strictly passive: *$\varrho > 0$ and $\nu > 0$.*

Suppose now that the subsystems in (5.79) satisfy

$$\langle \boldsymbol{y}_1, \boldsymbol{u}_1 \rangle_\tau \geq \varrho_1 \langle \boldsymbol{y}_1, \boldsymbol{y}_1 \rangle_\tau + \nu_1 \langle \boldsymbol{u}_1, \boldsymbol{u}_1 \rangle_\tau - \alpha_1 \tag{5.84}$$

$$\langle \boldsymbol{y}_2, \boldsymbol{u}_2 \rangle_\tau \geq \varrho_2 \langle \boldsymbol{y}_2, \boldsymbol{y}_2 \rangle_\tau + \nu_2 \langle \boldsymbol{u}_2, \boldsymbol{u}_2 \rangle_\tau - \alpha_2 \tag{5.85}$$

If the subsystems are connected according to (5.80) finite-gain $\mathcal{L}_2$ stability from the input $\boldsymbol{d}$ to the output $\boldsymbol{y}$ can be established subject to the simple criterion

$$\nu_2 + \varrho_1 > 0, \quad \nu_1 + \varrho_2 > 0 \tag{5.86}$$

See Vidyasagar [77, Theorem 2.1] for a proof. Physically, the theorem represents the fact that two power-dissipating subsystems in feedback interconnection bleed off energy as time proceeds. This renders the system as a whole stable in the process. The theorem also allows for non-passive (active) systems since the individual constants in (5.86) need not be positive. A lack of dissipation in one subsystem can be compensated for by the other.

5.2.2. Open-loop stability

Suppose now that no pitch control is applied so that $\dot{u} = \delta u = 0$. This invokes the force model from (5.63). The results in this subsection apply to wind turbines operating in the power optimizing regime. With recourse to Section 2.6, it is assumed that the slope on the torque schedule is non-negative. It is also assumed that the bias corrected pitch angle u satisfies the pitch-to-feather assumption in (5.37). These assumptions are necessary to validate the bounds on the constants k_1, k_2 and k_3 found in Section 5.1.1.

The passive subsystems in $\boldsymbol{P}(s)$ are driven by the extended force vector defined in (5.61) which gives rise to perturbations in the inflow and nacelle motion described by

$$\delta \boldsymbol{y}(s) = \boldsymbol{P}(s) \delta \boldsymbol{f}(s) \tag{5.87}$$

As indicated in (5.69) $\boldsymbol{P}$ represents a passive system and this is reflected in the notation. The open loop force model (5.63) consists of two effects. Let $\delta \boldsymbol{f} = \delta \boldsymbol{f}_1 + \delta \boldsymbol{f}_2$. The first component is a direct feedthrough represented by

$$\delta \boldsymbol{f}_1 \triangleq \frac{\bar{F}}{\bar{w}} \boldsymbol{D}_1 \delta \boldsymbol{w} \tag{5.88}$$

The latter term represents a dynamic effect given in the Laplace domain by

$$\delta \boldsymbol{f}_2(s) \triangleq \frac{2k_1k_2}{s+k_3} \frac{\bar{F}}{\bar{w}} \begin{bmatrix} 1 & 1 \\ 1 & 1 \end{bmatrix} \delta \boldsymbol{w}(s) \tag{5.89}$$

The flow vector defined in (5.61) comes apart as

$$\delta \boldsymbol{w} = \begin{bmatrix} 1 \\ 0 \end{bmatrix} \delta w_0 - \delta \boldsymbol{y} \tag{5.90}$$

The simplest way of approaching the stability problem for the overall system is to "close the loop" with the feedthrough term $\delta \boldsymbol{f}_1$ first. To this end, define the following dummy inputs and outputs

$$\delta \boldsymbol{y}_1 \triangleq \delta \boldsymbol{y} \tag{5.91a}$$

$$\delta \boldsymbol{y}_2 \triangleq \delta \boldsymbol{f}_2 \tag{5.91b}$$

$$\delta \boldsymbol{u}_1 \triangleq \delta \boldsymbol{f} + \frac{\bar{F}}{\bar{w}} \boldsymbol{D}_1 \delta \boldsymbol{y} \tag{5.91c}$$

$$\delta \boldsymbol{u}_2 \triangleq \delta \boldsymbol{w} \tag{5.91d}$$

These signals corresponds to the subsystems

$$\delta \boldsymbol{y}_1 = \boldsymbol{H}_1 \delta \boldsymbol{u}_1, \quad \delta \boldsymbol{y}_2 = \boldsymbol{H}_2 \delta \boldsymbol{u}_2 \tag{5.92}$$

The exogenous signals driving the system are given by

$$\delta \boldsymbol{d}_1 \triangleq \frac{\bar{F}}{\bar{w}} \boldsymbol{D}_1 \begin{bmatrix} 1 \\ 0 \end{bmatrix} \delta w_0, \quad \delta \boldsymbol{d}_2 \triangleq \begin{bmatrix} 1 \\ 0 \end{bmatrix} \delta w_0 \tag{5.93}$$

Using these definitions one recovers the following feedback interconnection

$$\delta \boldsymbol{u}_1 = \delta \boldsymbol{d}_1 + \delta \boldsymbol{y}_2, \quad \delta \boldsymbol{u}_2 = \delta \boldsymbol{d}_2 - \delta \boldsymbol{y}_1 \tag{5.94}$$

Consider now the inequality (5.69). Inserting the dummy signals from (5.91) shows that

$$\int_0^\tau \delta \boldsymbol{u}_1^T(t) \delta \boldsymbol{y}_1(t) \, dt \geq \frac{\bar{F}}{\bar{w}} \int_0^\tau \delta \boldsymbol{y}_1^T(t) \left(\frac{\boldsymbol{D}_1 + \boldsymbol{D}_1^T}{2} \right) \delta \boldsymbol{y}_1(t) \, dt - \alpha_1 \tag{5.95}$$

A renaming $\alpha = \alpha_1$ has been performed for notational consistency. The product on the right hand side can be bounded from below in the following manner

$$\delta \boldsymbol{y}_1^T \left(\frac{\boldsymbol{D}_1 + \boldsymbol{D}_1^T}{2} \right) \delta \boldsymbol{y}_1 \geq \lambda_{\min} \left\{ \frac{\boldsymbol{D}_1 + \boldsymbol{D}_1^T}{2} \right\} \delta \boldsymbol{y}_1^T \delta \boldsymbol{y}_1 \tag{5.96}$$

Using the definition of $\boldsymbol{D}_1$ from (5.63) and noting the bound on k_1 from (5.39) an explicit formula can be produced

$$\lambda_{\min} = \frac{4(k_1-1)\bar{a} - \sqrt{\bar{a}\left((8k_1(2k_1-3)+13)\bar{a}-4\right)+1}+1}{2\bar{a}} \geq \frac{1-\sqrt{\bar{a}\left(5\bar{a}-4\right)+1}}{2\bar{a}} \tag{5.97}$$

If one is willing to assume that the inflow factor remains in the well-defined region $\bar{a} \leq 1/2$ one finds the simple lower bound

$$\lambda_{\min} \geq \frac{1}{2} \tag{5.98}$$

One must proceed well above this inflow factor to render $\lambda_{\min}$ negative. The limit is in fact found at $\bar{a} = 4/5$. Noting Figure 5.6 this is unlikely to occur in practice. Now that one can ascertain the bound $\lambda_{\min} > 0$ under reasonable circumstances the details will not matter. It is justifiable to assume the following properties for $\boldsymbol{H}_1$.

$$\langle \delta\boldsymbol{u}_1, \delta\boldsymbol{y}_1 \rangle_\tau \geq \varrho_1 \langle \delta\boldsymbol{y}_1, \delta\boldsymbol{y}_1 \rangle_\tau - \alpha_1, \quad \varrho_1 > 0, \quad \alpha_1 > 0 \tag{5.99}$$

According to Definition 5.3 $\boldsymbol{H}_1$ is an output strictly passive system.

The second subsystem $\boldsymbol{H}_2$ is described by (5.89). Using the dummy signals (5.91) and realizing the transfer matrix gives rise a time-domain representation of $\boldsymbol{H}_2$.

$$\dot{z} + k_3 z = 2k_1k_2 \begin{bmatrix} 1 & 1 \end{bmatrix} \delta\boldsymbol{u}_2, \quad \delta\boldsymbol{y}_2 = \frac{\bar{F}}{\bar{w}} \begin{bmatrix} 1 \\ 1 \end{bmatrix} z \tag{5.100}$$

This system can be examined by defining a suitable storage function S and taking its derivative.

$$S \triangleq \frac{\bar{F}}{\bar{w}} \frac{1}{2k_1k_2} \frac{z^2}{2}, \quad \dot{S} = \delta\boldsymbol{u}_2^T \delta\boldsymbol{y}_2 - \frac{\bar{w}}{\bar{F}} \frac{k_3}{4k_2k_1} \delta\boldsymbol{y}_2^T \delta\boldsymbol{y}_2 \tag{5.101}$$

Rearranging terms and integrating over time shows that

$$\int_0^\tau \delta\boldsymbol{u}_2^T(t)\delta\boldsymbol{y}_2(t)\, dt = \frac{\bar{w}}{\bar{F}} \frac{k_3}{4k_2k_1} \int_0^\tau \delta\boldsymbol{y}_2^T(t)\delta\boldsymbol{y}_2(t)\, dt + S(\tau) - S(0) \tag{5.102}$$

As demonstrated in (5.39), (5.41) and (5.42) all the constants k_i can be taken as positive. Since $S(\tau) \geq 0$ the following bound has been established for $\boldsymbol{H}_2$.

$$\langle \delta\boldsymbol{u}_2, \delta\boldsymbol{y}_2 \rangle_\tau \geq \varrho_2 \langle \delta\boldsymbol{y}_2, \delta\boldsymbol{y}_2 \rangle_\tau - \alpha_2, \quad \varrho_2 > 0, \quad \alpha_2 > 0 \tag{5.103}$$

Clearly, this is another output strictly passive subsystem. The passivity theorem (5.86) can now be put to use. It has been demonstrated that

$$\varrho_1 > 0, \quad \varrho_2 > 0 \tag{5.104}$$

The interconnected wind turbine system is therefore finite gain $\mathcal{L}_2$ stable.

Proposition 5.1 (Open loop stability)**.** *Assume that pitch-to-feather is used so that* $0 \leq u \leq \pi/2$*. Furthermore, suppose that the generator torque schedule satisfies the criterion* $Q'_E(\Omega) > 0$*. Then, the floating wind turbine system is locally finite gain* $\mathcal{L}_2$ *stable about an equilibrium point.*

This is a surprisingly general result. Examples of torque schedules satisfying the criterion of non-negative slope are the optimal control law

$$Q_E^{\mathrm{MPPT}}(\Omega) = b\Omega^2 \tag{5.105}$$

and the torque characteristic of synchronous generators $Q_E^{\mathrm{SYNC}}(\Omega) = k_g(\Omega - \Omega_s)$.

Summarizing, wind turbines operating in open loop appear to be extremely well behaved systems. Note also that the results hold for arbitrarily complex hydroelastic systems, they just need to be passive. As a final note, it is verified that the internal dynamics of the rotor subsystem are stable. Expanding the transfer function in (5.46) using (5.32) shows that the poles are stable.

$$\frac{\delta\Omega}{\delta w}(s) = \frac{2\bar{F}}{J\bar{\Omega}s + \bar{\Omega}C'(\bar{\Omega}) + C(\bar{\Omega})}\left(1 + \frac{k_2}{s + k_3}\right)k_1 \tag{5.106}$$

The eigenvalues of the system read as

$$\lambda_1 = -k_3 < 0, \quad \lambda_2 = -\frac{\bar{\Omega}C'(\bar{\Omega}) + C(\bar{\Omega})}{J\bar{\Omega}} < 0 \tag{5.107}$$

The second pole must be negative since $C'(\bar{\Omega}) = Q'_E(\Omega) + 2b_d|\Omega| > 0$ and the net shaft torque arising from electrical power extraction and dissipatory effects satisfies $C(\bar{\Omega}) > 0$. This is a very pleasant conclusion. However, the use of pitch control will reverse the situation as discussed in the next section.

5.2.3. Closed loop stability

We proceed to examine the case associated with effective control, Case 2. This invokes the force model (5.64). Here, the situation represents Region II operation with active attempts at controlling the angular velocity of the rotor. A power limiting or torque limiting control law is used, see (5.8).

The absence of a dynamic effect similar to (5.89) simplifies matters. Proceeding in a similar manner as before, consider the dummy vector

$$\delta\boldsymbol{u} \triangleq \delta\boldsymbol{f} + \frac{\bar{F}}{\bar{w}}\boldsymbol{D}_0\delta\boldsymbol{y} \tag{5.108}$$

The exogenous signal will in this case be represented by

$$\delta\boldsymbol{d}(s) \triangleq \frac{s\mathcal{E}(s)}{\bar{w}}\begin{bmatrix} 1 \\ 1 \end{bmatrix}\delta\Omega_r(s) + \frac{\bar{F}}{\bar{w}}\boldsymbol{D}_0\begin{bmatrix} 1 \\ 0 \end{bmatrix}\delta w_0(s) \tag{5.109}$$

Let the closed loop system be denoted by $\delta \boldsymbol{y} = \boldsymbol{H}\delta \boldsymbol{u}$ where $\delta \boldsymbol{u} = \delta \boldsymbol{d}$. In this case, the feedback from the extended force model is absorbed completely by $\delta \boldsymbol{u}$. We return to the inequality (5.69). Inserting the dummy input from (5.108) shows that

$$\int_0^\tau \delta \boldsymbol{u}^{\mathsf{T}}(t)\delta \boldsymbol{y}(t)\ dt \geq \frac{\bar{F}}{\bar{w}} \int_0^\tau \delta \boldsymbol{y}^{\mathsf{T}}(t) \left(\frac{\boldsymbol{D}_0 + \boldsymbol{D}_0^T}{2} \right) \delta \boldsymbol{y}(t)\ dt - \alpha \tag{5.110}$$

The matrix appearing on the right-hand side is in general indefinite. However, bounding cases can be computed by noting that

$$\lambda_{\min} \left\{ \frac{\boldsymbol{D}_0 + \boldsymbol{D}_0^T}{2} \right\} \delta \boldsymbol{y}_1^T \delta \boldsymbol{y}_1 \leq \delta \boldsymbol{y}^{\mathsf{T}} \left(\frac{\boldsymbol{D}_0 + \boldsymbol{D}_0^T}{2} \right) \delta \boldsymbol{y} \leq \lambda_{\max} \left\{ \frac{\boldsymbol{D}_0 + \boldsymbol{D}_0^T}{2} \right\} \delta \boldsymbol{y}_1^T \delta \boldsymbol{y}_1 \tag{5.111}$$

Using the definition of $\boldsymbol{D}_0$ found in (5.62) permits the following bounds.

$$\lambda_{\min} = \frac{1 - 4\bar{a} - \sqrt{13\bar{a}^2 - 4\bar{a}} + 1}{2\bar{a}}, \quad \lambda_{\max} = \frac{1 - 4\bar{a} + \sqrt{13\bar{a}^2 - 4\bar{a} + 1}}{2\bar{a}} \tag{5.112}$$

Consider for instance the lightly-loaded case $\bar{a} = 0$ which gives the highest $\lambda_{\min}$ possible with positive inflow factors and net aerodynamic power extraction. Here, $\lambda_{\min} = -1$ and a conservative estimate ensues as

$$\int_0^\tau \delta \boldsymbol{u}^{\mathsf{T}}(t)\delta \boldsymbol{y}(t)\ dt \geq -\frac{\bar{F}}{\bar{w}} \int_0^\tau \delta \boldsymbol{y}^{\mathsf{T}}(t)\delta \boldsymbol{y}(t)\ dt - \alpha \tag{5.113}$$

This implies a system with significant *lack* of passivity since one would require a negative feedback with a gain at least as high as $\delta \boldsymbol{u} = -(\bar{F}/\bar{w})\delta \boldsymbol{y}$ to render the plant $\mathcal{L}_2$-stable. For output strictly passive systems, like the ones applicable to the open loop case in Section 5.2.2, one has by definition

$$\varrho \langle \delta \boldsymbol{y}, \delta \boldsymbol{y} \rangle_\tau \leq \langle \delta \boldsymbol{y}, \delta \boldsymbol{u} \rangle_\tau + \alpha \tag{5.114}$$

This implies the output energy $\langle \delta \boldsymbol{y}, \delta \boldsymbol{y} \rangle_\tau$ will always be upper bounded by the energy supplied to the system $\langle \delta \boldsymbol{y}, \delta \boldsymbol{u} \rangle_\tau$. Let $\upsilon = -\lambda_{\min} > 0$. For the present system one has

$$\upsilon \langle \delta \boldsymbol{y}, \delta \boldsymbol{y} \rangle_\tau \geq 0 \geq \langle \delta \boldsymbol{y}, -\delta \boldsymbol{u} \rangle_\tau - \alpha \tag{5.115}$$

The output energy is now only lower bounded and can in principle acquire very large values. What is seen is a manifestation of the control-induced destabilization phenomena demonstrated in Section 1.2. It can be shown that the eigenvalues of the closed loop system will indeed tend to wander into the right half plane when attempting effective control. However, this involves the use of an explicit model for $\boldsymbol{P}$ giving rise to a less general conclusion. It has been shown that demonstrating stability through passivity arguments is impossible. The result is interesting since it does not depend on the particulars of $K(s)$. All effective attempts of regulating the system will ultimately lead to the same result.

The unfortunate situation illustrated above arises whenever effective regulation of Ω is attempted. The key distinguishing factor from the open-loop case is effective suppression of disturbances from $\delta\boldsymbol{w}$. This will in turn hinder variations in the storage manifold σ. In the next section, disturbances are reintroduced through feedforward and stability is reestablished.

5.2.4. Feedforward

The only signal amenable to manipulation in the closed loop model described above is the reference signal Ω_r. At this point it will be convenient to recount the force model associated with effective control.

$$\delta\boldsymbol{f}(s) = \frac{\bar{F}}{\bar{w}}\left(\boldsymbol{D}_0\delta\boldsymbol{w}(s) + \frac{s\mathcal{E}(s)}{\bar{F}}\begin{bmatrix}1\\1\end{bmatrix}\delta\Omega_r(s)\right), \quad \boldsymbol{D}_0 \triangleq -\begin{bmatrix}1 & 1\\ 2 & 3-\bar{a}^{-1}\end{bmatrix} \tag{5.116}$$

The chief problem in the closed-loop case was the indefinite nature of $\boldsymbol{D}_0$. So, what if the reference signal Ω_r is used to render $\boldsymbol{D}_0$ positive definite? Consider the following scheme with Ω_0 representing a constant setpoint.

$$\Omega_r(t) = \Omega_e(t) + \Omega_0 \tag{5.117}$$

Let the "correction signal" Ω_e be generated by the following stable first order ODE.

$$J\Omega_0\dot{\Omega}_e(t) + [\Omega_0 C'(\Omega_0) + C(\Omega_0)]\Omega_e(t) = -K_e F(t)\dot{x}(t) \tag{5.118}$$

Here K_e represents a positive constant to be determined later. Note that a constant power torque schedule $Q_E(\Omega) = E^+/\Omega$ will not hinder the preceding equation from use. The eigenvalue of the ODE remains in the left half plane as seen from

$$\Omega_0 C'(\Omega_0) + C(\Omega_0) = \frac{\partial\Omega C(\Omega)}{\partial\Omega}(\Omega_0) = 3b_d|\Omega_0|\Omega_0^2 > 0 \tag{5.119}$$

Linearization about $\bar{\Omega} = \Omega_0$ and subsequent Laplace transformation shows that the reference signal will be equipped with feedforward dynamics given by

$$\delta\Omega_r(s) = \delta\Omega_e(s) = -\frac{K_e\bar{F}\delta\dot{x}(s)}{J\bar{\Omega}s + \bar{\Omega}C'(\bar{\Omega}) + C(\bar{\Omega})} \tag{5.120}$$

No feedforward from the inflow w_i will be attempted since reliable measurements cannot realistically be expected. Recalling (5.32) one may proceed to find the compact expression

$$\delta\Omega_r(s) = -\frac{K_e\bar{F}}{s\mathcal{E}(s)}\delta\dot{x}(s) \tag{5.121}$$

Variations in the storage manifold are determined by $\delta\Omega_r$ in closed loop according to (5.50). Plugging in the preceding equation shows that the feedforward

mechanism proposed above attempts to sequester energy when moving into the wind with $\dot{x} < 0$. On the other hand, energy will be extracted from the spinning mass when moving out of the wind and $\dot{x} > 0$.

$$\delta\sigma(t) = -\int_0^t K_e \bar{F} \delta\dot{x}(t')\, dt' \tag{5.122}$$

This relation motivates the notion of an *energy shaping reference feedforward* when referring to the equation (5.118).

One may proceed to examine if the desired stabilizing effect has been realized. Substitution in (5.116) noting that $\boldsymbol{w} = \mathrm{col}[w_0 - \dot{x}, -w_i]$ leads to the following expression

$$\delta\boldsymbol{f}(s) = \frac{\bar{F}}{\bar{w}} \left(\boldsymbol{D}_2 \delta\boldsymbol{w}(s) - K_e \begin{bmatrix} 1 \\ 1 \end{bmatrix} \delta w_0(s) \right), \quad \boldsymbol{D}_2 \triangleq \begin{bmatrix} K_e - 1 & 1 \\ K_e - 2 & \bar{a}^{-1} - 3 \end{bmatrix} \tag{5.123}$$

If K_e is chosen with care it is possible to render $\boldsymbol{D}_2$ positive definite over the operating envelope in which pitch control is utilized. It is assumed that the wind turbine is operating below the point of optimal power extraction implying $\bar{a} \leq 1/3$. This is an inevitable consequence of applying pitch control which aims to hinder utilization of the full wind energy potential. See Figure 2.9.

Consider Figure 5.9. Here, values for K_e yielding a positive definite matrix $\boldsymbol{D}_2 + \boldsymbol{D}_2^T \succ 0$ are represented by the area under the black curve. Around the optimum $a = 1/3$ this range is limited to $K_e \approx 3$. But, as the thrust tapers off at higher wind speeds K_e can assume large values. The vortical motion amplification discussed in Section 5.1.2 influences this result in a significant manner. Had there been no inflow it would have been sufficient with $K_e > 1$.

The feedforward necessary to stabilize the plant in the region of effective regulation $T(s) \simeq 1$ can be given exactly by

$$\begin{aligned} K_e^-(a) < K_e < K_e^+(a) \\ K_e^-(a) \triangleq \frac{1 - (3/2)a - \sqrt{3a^2 - 4a + 1}}{2a} \geq 1 \\ K_e^+(a) \triangleq \frac{1 - (3/2)a + \sqrt{3a^2 - 4a + 1}}{2a} \geq 3 \end{aligned} \tag{5.124}$$

It may be inconvenient to utilize a direct thrust measurement $F(t)$ in (5.118). The following rule can be used as an alternative

$$K_e'(t) = \frac{3F^+}{F(t)} \tag{5.125}$$

Here, F^+ corresponds to the highest thrust loading experienced by the wind turbine over its operating envelope. This occurs at the optimal inflow $a = 1/3$. An illustration of the thrust as a function of wind speed can be found

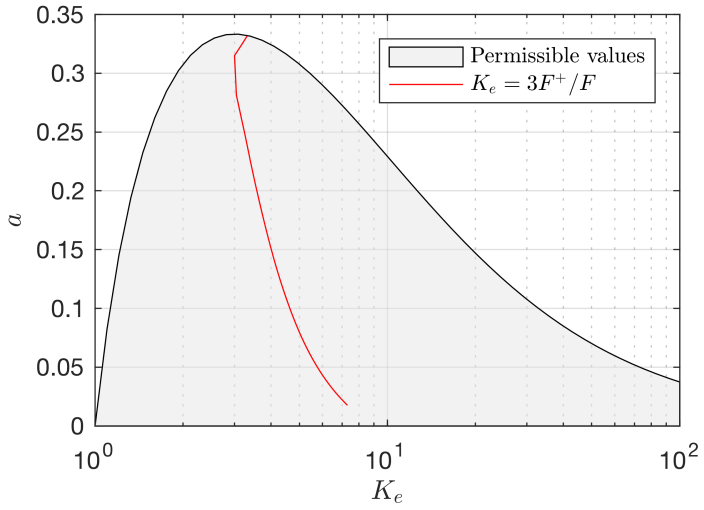

Figure 5.9.: Permissible values for K_e as a function of the inflow factor. The red line illustrates a fixed gain given in terms of the maximal thrust.

in Figure 2.10. Since the thrust F relates to the inflow factor a through the Rankine-Froude model given in (2.18) it can be shown that (5.125) will guarantee that the matrix $\boldsymbol{D}_2$ is positive definite throughout Region II operation. This is what the red line depicted in Figure 5.9 shows. As the wind speed increases, the thrust F is lowered giving rise to a higher K_e. But, the inflow also decreases and the higher gain is accommodated with good margin. Inserting (5.125) into (5.118) gives rise to a simplified time-invariant filter suitable for practical applications.

$$J\Omega_0\dot{\Omega}_e(t) + [\Omega_0 C'(\Omega_0) + C(\Omega_0)]\Omega_e(t) = -3F^+\dot{x}(t) \tag{5.126}$$

It remains to be shown that the feedforward corrected system is stable. We repeat the steps in Section 5.2.3, now with

$$\delta\boldsymbol{u} \triangleq \delta\boldsymbol{f} + \frac{\bar{F}}{\bar{w}}\boldsymbol{D}_2\delta\boldsymbol{y} \tag{5.127}$$

The exogenous signal is also modified and becomes

$$\delta\boldsymbol{d} \triangleq \frac{\bar{F}}{\bar{w}}\boldsymbol{D}_0\begin{bmatrix}1\\0\end{bmatrix}\delta w_0 \tag{5.128}$$

A suitably modified variation of (5.110) is readily recovered as

$$\int_0^\tau \delta\boldsymbol{d}^T(t)\delta\boldsymbol{y}(t)\,dt \geq \frac{\bar{F}}{\bar{w}}\int_0^\tau \delta\boldsymbol{y}^T(t)\left(\frac{\boldsymbol{D}_2 + \boldsymbol{D}_2^T}{2}\right)\delta\boldsymbol{y}(t) - \alpha \tag{5.129}$$

If the feedforward constant K_e is chosen in accordance with (5.124), most readily accomplished by using the mechanism in (5.126), the matrix $\boldsymbol{D}_2$ will be positive definite. This implies that there exists a positive constant $\varrho > 0$ so that

$$\frac{\bar{F}}{\bar{w}} \delta \boldsymbol{y}^{\mathsf{T}} \left(\frac{\boldsymbol{D}_2 + \boldsymbol{D}_2^{\mathsf{T}}}{2} \right) \delta \boldsymbol{y} \geq \varrho \delta \boldsymbol{y}^{\mathsf{T}} \delta \boldsymbol{y} \tag{5.130}$$

Hence the result

$$\langle \delta \boldsymbol{d}, \delta \boldsymbol{y} \rangle_\tau \geq \varrho \langle \delta \boldsymbol{y}, \delta \boldsymbol{y} \rangle_\tau - \alpha, \quad \varrho > 0, \quad \alpha > 0 \tag{5.131}$$

According to Definition 5.3 the feedforward stabilized wind turbine is an output strictly passive system. It is well known that such systems are $\mathcal{L}_2$-stable with gain $\gamma \leq \varrho^{-1}$. See Khalil [21, Lemma 6.5] for a mathematical proof of this fact. The astute reader will note that the feedforward control strategy described above is, in essence, precisely the one proposed in the Section 1.3.

Proposition 5.2 (Closed loop stability)**.** *Let a floating wind turbine be equipped with a control system realizing the behavior $\Omega(t) = \Omega_e(t) + \Omega_0$ where $\Omega_e(t)$ is governed by (5.126). Then, the system is locally finite gain $\mathcal{L}_2$ stable about an operating point $\bar{\Omega} = \Omega_0$.*

Remark 5.1. *This is not a statement of overall closed loop stability. Rather, that a major destabilizing effect has been removed. The frequency behavior of the full system around the crossover point ω_b is difficult to analyze in a general manner. However, noting that the system will tend towards stable open loop behavior at $\omega \gg \omega_b$, it can be stated that motion occurring in frequency bands at a sufficient remove from ω_b will indeed be stable.*

Other solutions

It appears that many researchers are cognizant of the control induced destabilization phenomena uncovered in Section 5.2.3 and hinted at in Section 1.2. Several authors have described damping methods aimed at reducing platform oscillations.

A rather simple approach is direct pitch alterations $u(t) = K\dot{x}(t)$. However, this methodology can be expected to be very ineffective below the regulator bandwidth ω_b. From the perspective of the regulator, these variations will simply count as another disturbance to be rejected. This prohibits effective variations in σ as Ω will be kept close to the setpoint Ω_0. Jonkman [6] describes this scheme and finds little to no improvement in the platform damping. The preceding reasoning shows why.

The dynamic reference method uses alterations in the reference signal to stabilize the system. This is similar to the energy shaping approach detailed above.

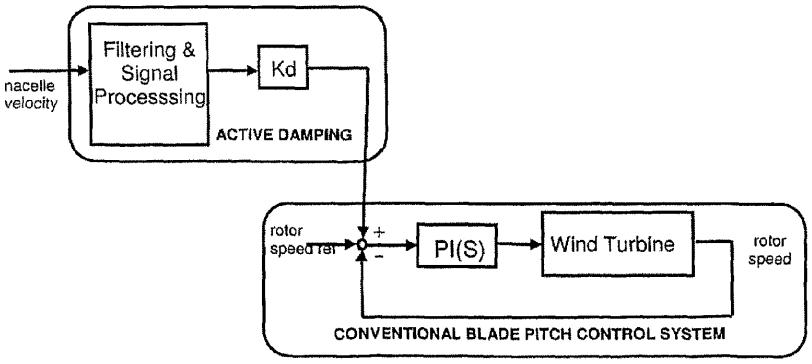

Figure 5.10.: Block diagram from the patent [12]. This is unmistakably a dynamic reference approach.

Other researchers have found that this method works well. Lackner [10] uses a reference signal given by

$$\Omega_r(t) = \Omega_0 - K\dot{x}(t) \tag{5.132}$$

Improvement in platform damping are indeed obtained. A compelling heuristic argument can be found in the cited work. There is reason to suspect that this mechanism is (or has been) used on the HYWIND prototype. Figure 5.10 shows an image gleaned from a recent patent (2013) clearly showing a dynamic reference approach. Improvements are reported in the document and platform motion is restrained.

These methods differ from the present approach in the filtering action described by (5.126). To put it another way, the methods of [10] and [12] pass $\dot{x}$ through a high-pass filter when compared to the present approach. Using (5.121) one finds the difference

$$\frac{\dot{x}_{\mathrm{dr}}}{\dot{x}_{\mathrm{es}}}(s) = \frac{s\mathcal{E}(s)}{\bar{F}}\frac{K}{K_e} \tag{5.133}$$

This transfer function describes how the dynamic reference method compares to the energy shaping method. Note that

$$s\mathcal{E}(s) = J\bar{\Omega}s + \bar{\Omega}C'(\bar{\Omega}) + C(\bar{\Omega}) \tag{5.134}$$

The presence of the constant term $\bar{\Omega}C'(\bar{\Omega}) + C(\bar{\Omega})$ indicates that the matrix $\boldsymbol{D}_2$ may indeed acquire the property of positive definite using the scheme in [10] or [12]. However, high-frequency variations in the reference signal will be incurred due to the differentiation through $J\bar{\Omega}s$.

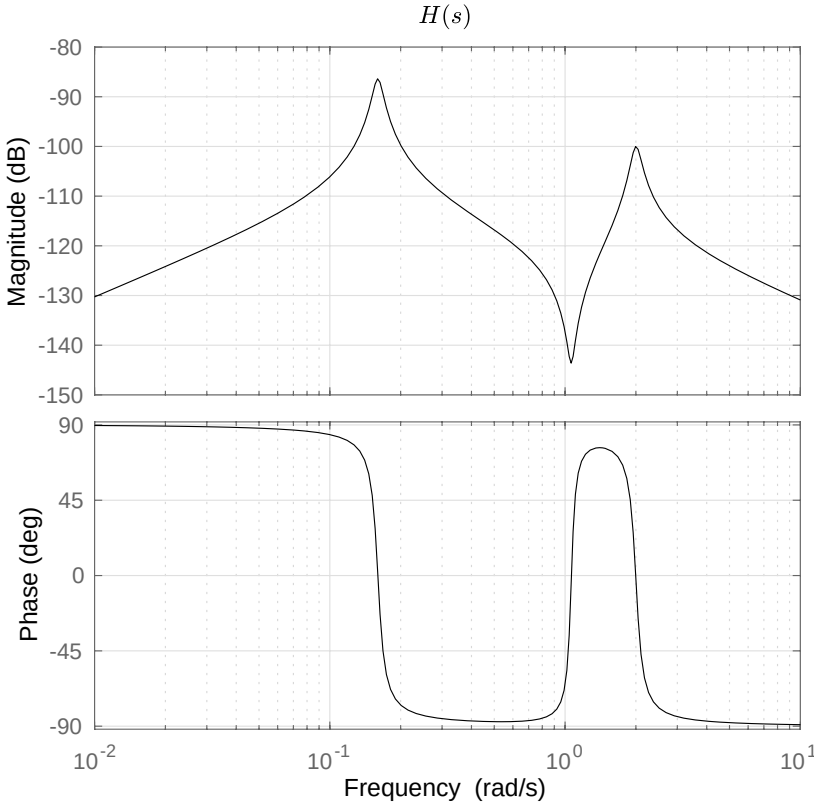

Figure 5.11.: The simulated frequency response of the nacelle velocity $\dot{x}$ subject to a thrust force F. The slow mode corresponds to platform displacements in surge and the fast mode captures tower bending.

5.3. Case study

5.3.1. Simulation model

The model used for technical analysis is somewhat simpler than the one showcased in the time domain simulations displayed below. Unless specified otherwise, the full DVT wake model will be used rather than the low-frequency approximation. Drag in thrust will also be included.

The representative 5 MW wind turbine described in Jonkman et al. [13] will supply numerical values to the simplified rotor subsystem. Simulations in Region II are performed with a mean wind speed of $w_0^{\text{mean}} = 17\,\text{m}\,\text{s}^{-1}$. Turbulence is generated with methods similar to the one described in Section 2.2. The various model constants are computed from the relations shown below.

$$k = \frac{2\rho A_p R}{3\lambda_*}, \quad b_d = \frac{1}{2}\rho A \left(B^2 \frac{16}{27} - C_P^* \right) \left(\frac{R}{\lambda_*} \right)^3, \quad d = \frac{1}{2}\rho A C_F \tag{5.135}$$

Recall that $R_p = BR$ and $A_p = \pi R_p^2$.

J	$4 \times 10^7 \mathrm{kg\,m^2}$
R	$63\,\mathrm{m}$
E^+	$5.3\,\mathrm{MW}$
Ω_0	$1.25\,\mathrm{rad\,s^{-1}}$
ρ	$1.225\,\mathrm{kg\,m^{-3}}$
C_P^*	0.48
λ_*	7.5
B	0.94
C_F	0.0145

Table 5.1.: Numerical values used for simulation of the rotor subsystem.

The platform model shown in the simulations is based on the TLP platform described in Goupee et al. [14]. A simple mass spring damper will be used to model the nacelle motion

$$H^{\mathrm{TLP}}(s) = \frac{k_0\omega_0^2 s}{s^2 + 2\zeta_0\omega_0 s + \omega_0^2}$$
$$\omega_0 = 0.16\,\mathrm{rad\,s^{-1}}, \quad k_0 = 3 \times 10^{-5}\mathrm{m\,N^{-1}}, \quad \zeta_0 = 0.05 \quad (5.136)$$

It will be interesting to test the control system's response over a wider frequency band. A tower bending mode is included towards this end. Based on the numbers in [13], the following model will be used

$$H^{\mathrm{TWR}}(s) = \frac{k_1\omega_1^2 s}{s^2 + 2\zeta_1\omega_1 s + \omega_1^2}$$
$$\omega_1 = 2\,\mathrm{rad\,s^{-1}}, \quad k_1 = 5 \times 10^{-7}\mathrm{m\,N^{-1}}, \quad \zeta_1 = 0.05 \quad (5.137)$$

As a matter of notation, x_0 will denote the platform displacement in surge whereas x_1 will signify the horizontal tower bending deflection at the nacelle. Summarizing, the simulation model for the hydroelastic subsystem will reads as the sum

$$H(s) = H^{\mathrm{TWR}}(s) + H^{\mathrm{TLP}}(s) \quad (5.138)$$

A Bode diagram of this function is shown in Figure 5.11. When operating in closed loop a PI-regulator similar to the standard variation found in Jonkman et al. [13] is used. The bandwidth of the control system will be denoted ω_b.

5.3.2. Open loop operation

The MPPT control law detailed in Section 2.6 not only extracts wind power in a quasi-optimal manner. It also facilitates stabilization of the tower and plat-

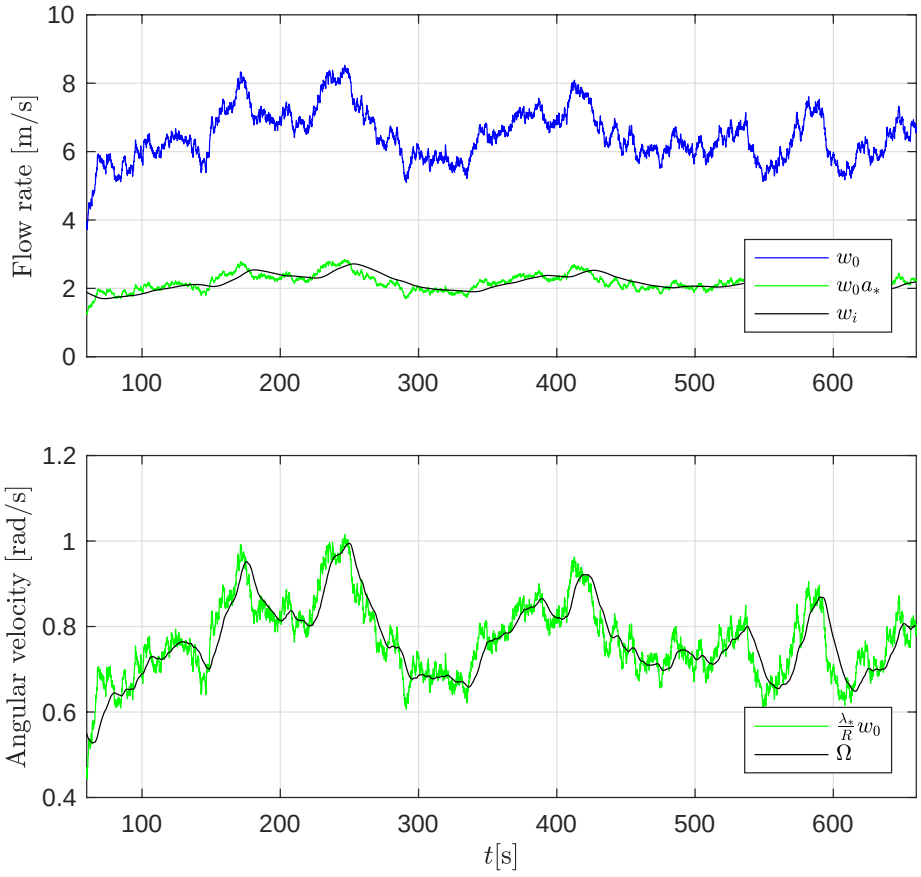

Figure 5.12.: The MPPT algorithm under turbulent wind conditions. The platform motion is not considered in this simulation.

form due to its non-negative slope, as discussed in Section 5.2.2. A simulation highlighting the efficacy of the algorithm is shown in Figure 5.12. Here, the floating platform is disconnected from the loop. The angular velocity is seen to track the reference generated by the wind speed quite well despite turbulence.

$$\Omega_r^{\mathrm{MPPT}}(t) = \frac{\lambda_*}{R} w_0(t) \tag{5.139}$$

Interestingly, *this is achieved without measurements of* $w_0(t)$. There are significant challenges with wind speed measurement due to the rotor's aerodynamic disturbance. A measurement free control law achieving tracking of a time varying optimal point is therefore highly advantageous. The figure also shows that the inflow w_i tracks the quasi-static optimum $w_i = a_* w_0$ with $a_* = 1/3$, albeit with a significant amount of lag; the sizable time constant associated with the inflow dynamics is the reason behind this phenomena.

Figure 5.13 illustrates the rotor's effect on the platform. The "open loop" case represents the situation where the nacelle motion $\dot{x}$ is not permitted to feed back through w; the loop is broken. The "closed loop" case reintroduces the feedback.

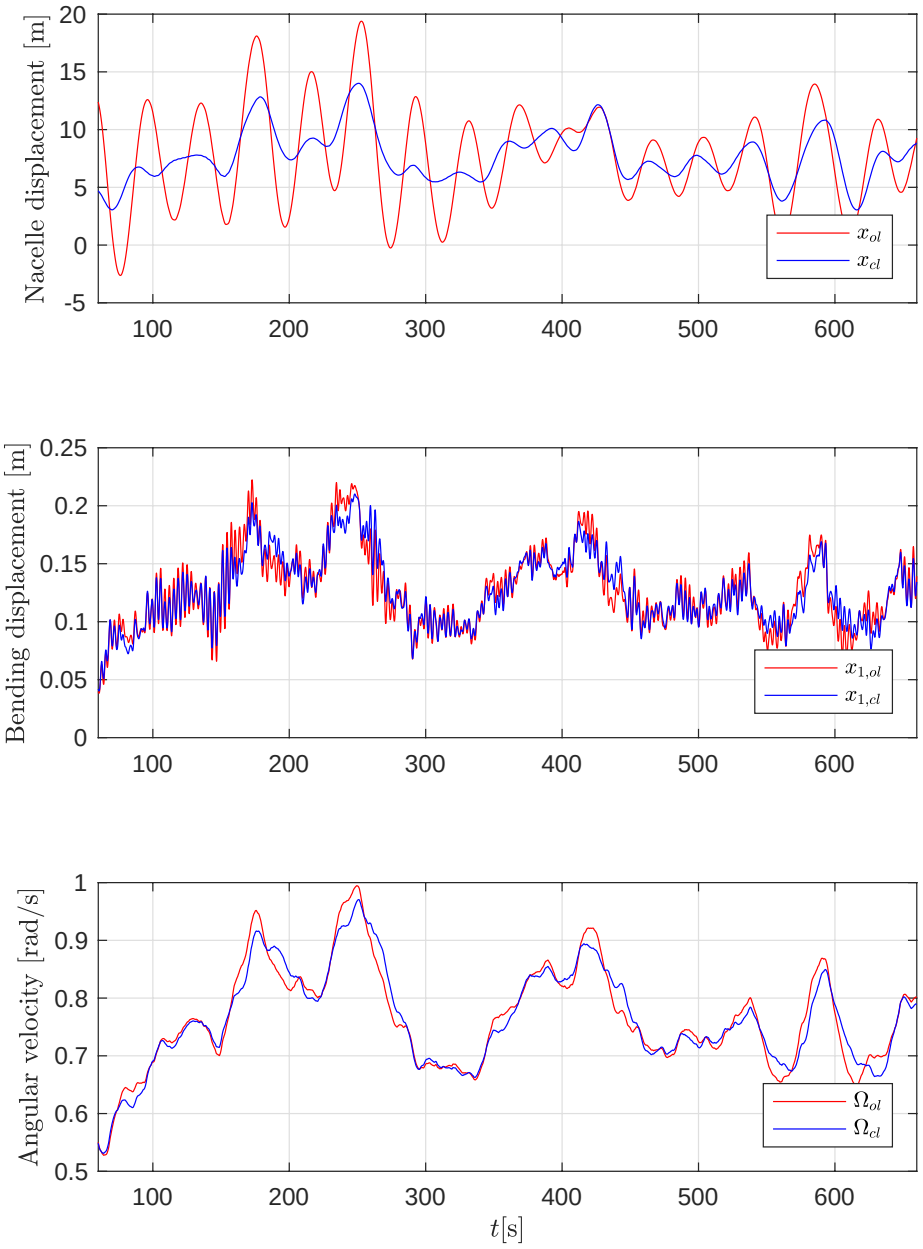

Figure 5.13.: A simulation of the MPPT law with a floating platform in the loop. The wind signal is similar to the one depicted in Figure 5.12.

This permits an examination of the rotor system's effect on platform motion. Verify that the rotor introduces significant amounts of damping into the platform dynamics. Both the high frequency tower bending and the low frequency TLP surge are damped. This provides a practical illustration of Proposition 5.2. Note that the angular velocity suffers little from closing the loop with the platform.

5.3.3. Closed loop operation

A constant torque control strategy will be used for the simulations presented here.

$$Q_E(\Omega) = Q_E^+ \tag{5.140}$$

Pitch regulation is used to achieve the dual objective of set-point regulation and balancing the difference in aerodynamic and electrical torque $Q(t) - Q_E^+$. The PI-controller is chosen so that the crossover frequency ω_b is placed above the platform's resonance at $\omega_0 = 0.16\,\mathrm{rad\,s^{-1}}$ but below the tower resonance at $\omega_1 = 2\,\mathrm{rad\,s^{-1}}$.

The benign characteristics of the wind turbine system in the absence of effective control suggests that damping should occur in the frequency band $\omega \gg \omega_b$. Figure 5.14 compares how the bending mode behaves when it is fed back in w and the case where the loop is broken. It is observed that motion taking place at frequencies well above ω_b will be damped, in line with the prediction.

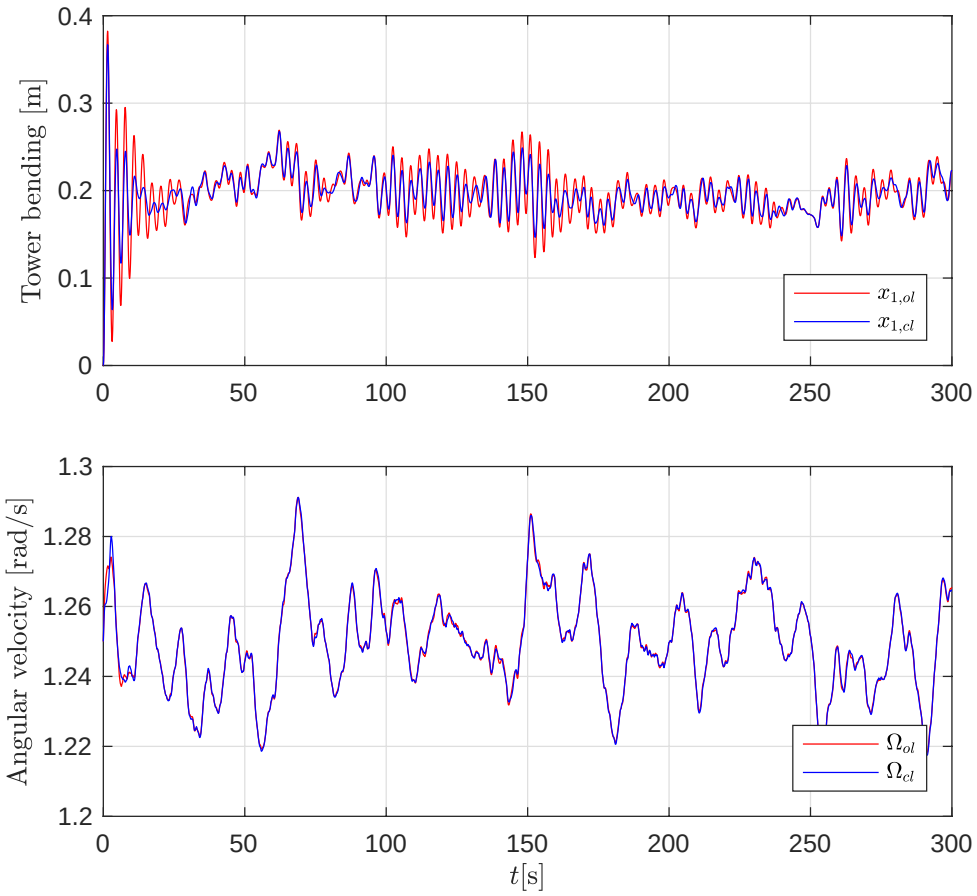

Figure 5.14.: Comparison study of the tower bending mode with and without feedback from the tower bending rate $\dot{x}_1$ in the interconnected plant.

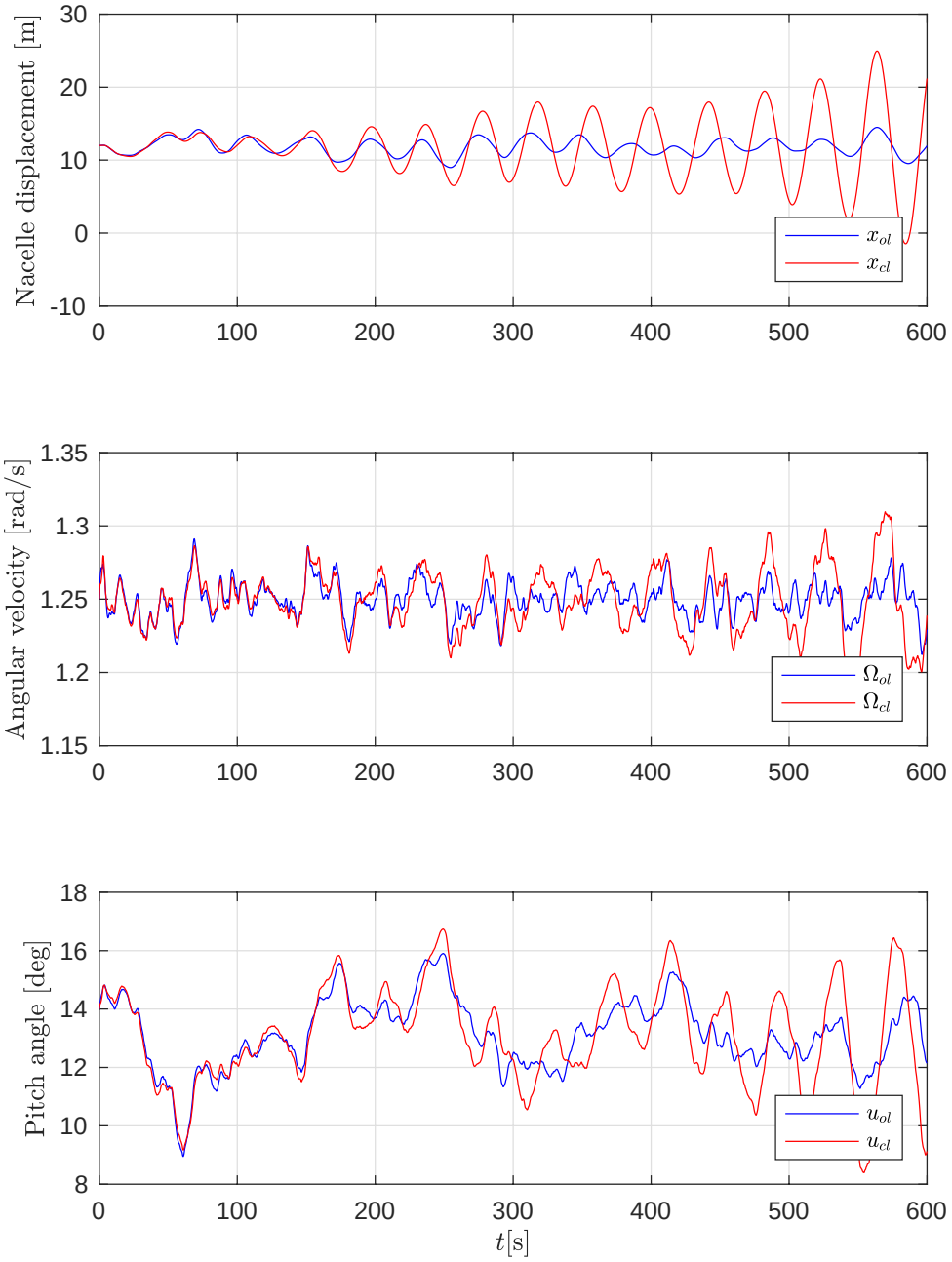

Figure 5.15.: Comparison study of the platform surge with and without feedback from the surge rate $\dot{x}_0$ in the interconnected plant.

The theory also makes a second prediction; namely that energy will be pumped into the support structure if the motion takes place in the frequency band of effective regulation. Since the resonance frequency in platform surge satisfies this criteria it should be destabilized according to the present theory. Indeed, Figure 5.15 demonstrates just such a phenomena. This is a practical demonstration of control-induced destabilization.

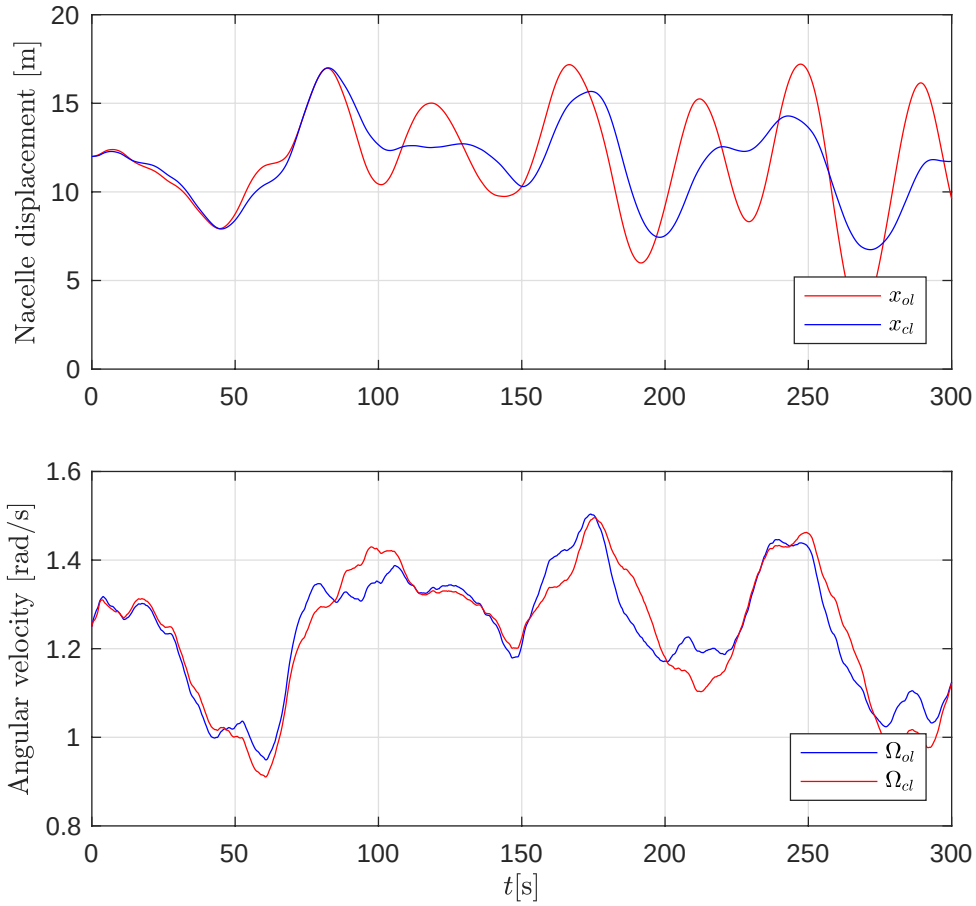

Figure 5.16.: Response of a detuned regulation system under turbulent wind conditions.

Controller detuning

An obvious solution to the resonance problem is to regulate with a lower bandwidth so as to bring a wider frequency band into $\omega \gg \omega_b$. That is, one avoids the problem of effective regulation by making the control system ineffective over a wider frequency band. For the present problem, this implies $\omega_b \ll 0.16\,\mathrm{rad\,s^{-1}}$. With such a low controller gain the resulting system will be vulnerable to large overshoots and slow convergence. Figure 5.16 illustrates this approach with $\omega_b = 0.1\,\mathrm{rad\,s^{-1}}$. While platform motion is restrained somewhat, the angular velocity strays very far from the setpoint at $\Omega_0 = 1.25\,\mathrm{rad\,s^{-1}}$. This result reflects the findings of Larsen and Hanson [5] and Jonkman [6] who both attempted so-called "detuning". Since this control methodology has been proven unreliable, both here and in the cited works, it will not be examined further.

5.3.4. Feedforward stabilization

Figure 5.17 compares some stabilization methods from the literature, all recounted in Section 5.2.4. The direct pitch method is implemented as

$$u(t) = K_{\mathrm{dp}}\dot{x}(t), \quad K_{\mathrm{dp}} = 1\,\mathrm{rad\,s\,m^{-1}} \tag{5.141}$$

No tuning attempts resulted in satisfactory performance. The platform motion is not better than if pitch correction had not been applied. Extreme excursions in collective pitch are seen to occur. This is not a viable method.

A reference injection approach based on Skaare and Nielsen [12] is also shown. The dynamic reference used for the simulation was computed using the law

$$\Omega_d(t) = \Omega_0 - K_{\mathrm{dr}}\dot{x}(t), \quad K_{\mathrm{dr}} = 1\,\mathrm{rad\,m^{-1}} \tag{5.142}$$

Increasing the gain beyond this point introduced significant ripple in the control signal u. Some is still present in the figure, but the tradeoff seems fair at the gain chosen above. The platform stabilization furnished by this method is quite satisfactory and the setpoint reference is tracked well.

The energy shaping method attains a reference tracking of a comparable quality to the dynamic reference approach. Here, a maximum thrust of $F^+ = 8 \times 10^5\,\mathrm{N}$ is used with the feedforward mechanism (5.126). Some additional platform undulations are present compared to the dynamic reference method. The discussion in Section 5.2.4 pointed out that the energy shaping approach passes the nacelle motion through a low pass filter. A key difference between the proposed method and the dynamic reference method is therefore lowered damping at higher frequencies. However, benefits are accrued in terms of smoother pitch application.

A situation where the energy shaping method outperforms the dynamic reference method is when a constant power strategy is used. The filter converting the nacelle motion into a reference signal will in this case reduce to

$$\Omega_e(s) = -\frac{3F^+}{J\Omega_0 s + 3b_d|\Omega_0|\Omega_0}\delta\dot{x}(s) \tag{5.143}$$

This has the effect of generating larger reference signals Ω_e when compared to a constant torque strategy with the denominator $J\Omega_0 s + Q_E^+ + 3b_d|\Omega_0|\Omega_0$. Longer time constants will also be incurred.

The present theory suggests that the damping properties of the method will persist as long as an appropriate energy shaping filter is used. Figure 5.18 bolsters this contention; the energy shaping method stabilizes the system with a smoother pitch input and less deviations in the angular velocity than the dynamic reference method.

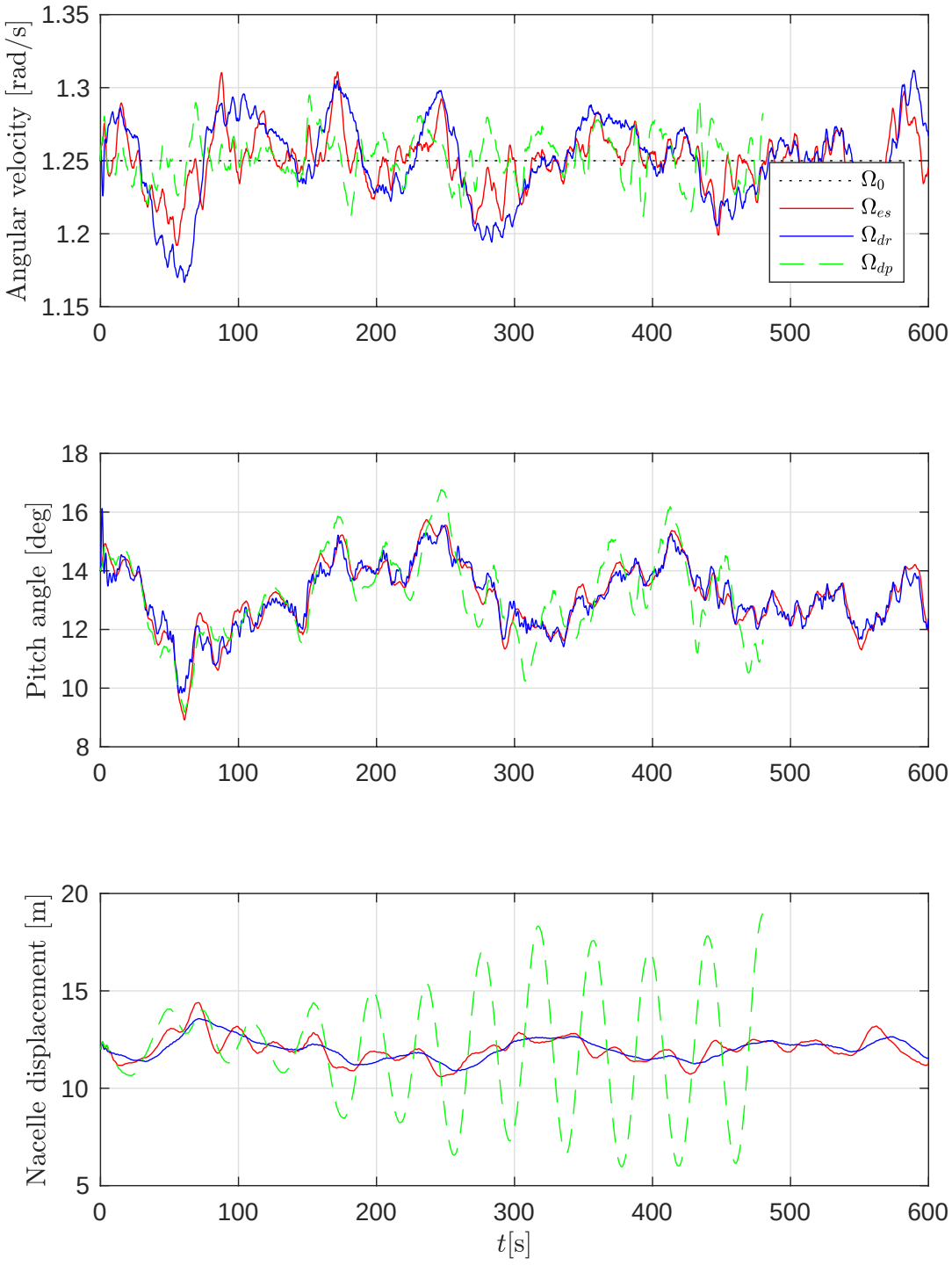

Figure 5.17.: The direct pitch method (dp), dynamic reference method (dr) and the energy shaping stabilizer (es).

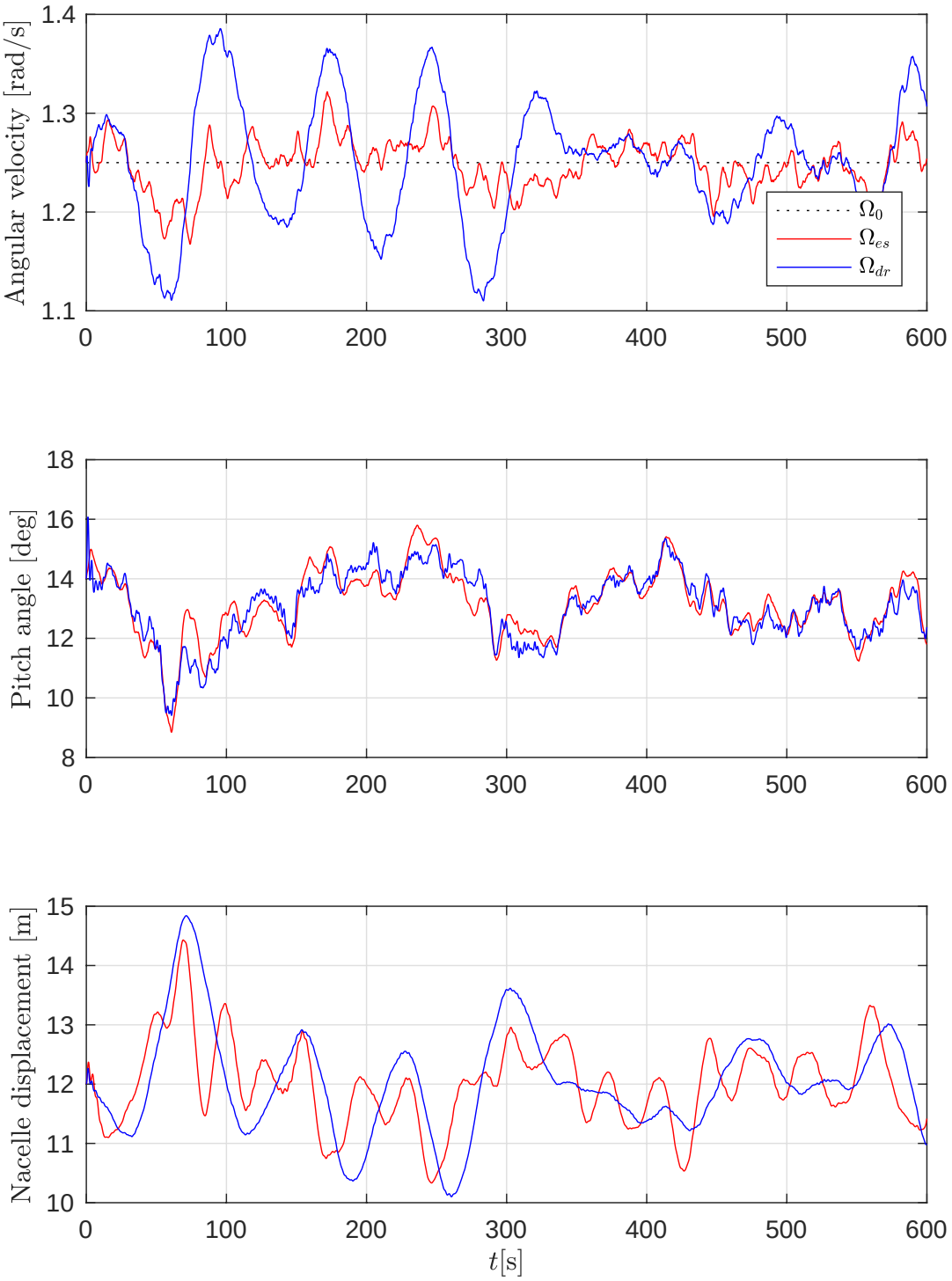

Figure 5.18.: The direct pitch method (dp) and dynamic reference method (dr) with a constant power strategy.

5.4. Chapter summary

This chapter can be summarized as follows.

- The first part of the chapter Section 5.1 detailed the model and its properties.

  In Section 5.1.1 the rotor system was defined and analyzed. The energetics associated with the module were captured by defining a storage manifold representing the energy sequestered as motion or through power extraction and dissipation. A brief discussion of operating regions I and II was presented along with implications for the model. The circulatory reversal phenomena was described and linked to the control-induced resonance phenomena. A small-signal model capable of representing both open and closed loop operation was detailed and refined.

  The wake dynamics were discussed in Section 5.1.2. It was demonstrated that inflow models are important for two main reasons: (1) they give rise to significant transient at time-scales salient for automatic control and (2) the inflow will amplify the effects of nacelle motion through a phenomena referred to as vortical motion amplification.

- The stability of the interconnected floating wind turbine system was examined in Section 5.2. A brief exposition of input/output stability concepts was given in Section 5.2.1 along with the important passivity theorem. In Section 5.2.2 a very general result pertaining to wind turbines operating in the absence of pitch control was given; they are locally finite gain $\mathcal{L}_2$-stable. As the discussion turned to closed loop operation in Section 5.2.3 less encouraging results were found. Here, it was shown that any attempt at effective setpoint regulation of the angular velocity will lead to destabilization. The section on stability was concluded in Section 5.2.4 where an energy shaping feedforward mechanism capable of restoring $\mathcal{L}_2$ stability was proposed and proved effective. Due notice was made of existing attempts towards the same end.

- Section 5.3 presented an extensive simulation study highlighting the results of previous sections. A 5 MW wind turbine on a tension-leg platform served as a realistic model of future offshore wind power systems. The benign open loop behavior identified in Section 5.2.2 as well as the control-induced destabilization phenomena from Section 5.2.3 were demonstrated. A number of stabilization schemes including direct pitch control, reference injection and the energy-shaping methodology of Section 5.2.4 were compared. The new approach acquitted itself well, providing comparable or better performance than existing solutions.

6. Conclusion

This thesis started with a simple idea; an energy balance model of a floating wind turbine. However, while the concept was sound, it glossed over many important effects. A new theory of wind turbine dynamics, combining old ideas such as the Joukowsky rotor with new ideas such as frequency domain identification, followed as greater insight was pursued. The title of the thesis is somewhat misleading. While the theory did indeed result in a convincing solution of the platform stabilization problem, it is the framework and not the application that is most interesting. It has been shown that several distinct aerodynamical effects, the vortex lifting law and the vortical wake, can be put on a form relevant for control design and systems analysis. It has also been demonstrated that control theoretical concepts have great utility in aerodynamics. Who would have thought that the helical vortex wake could be modeled using an impulse response and analyzed with a scattering transform? The success in addressing the control induced resonance phenomena indicates that the the passive systems approach to aerodynamics is a fruitful methodology.

A vast majority of control studies dealing with wind turbines utilize the coefficient models described in Chapter 2 or a linearized dynamic model given as an output from some engineering code. These approaches are not ineffective, but they do lack elegance and hinder physical insight. It is hoped that this thesis will give the reader a glimpse of the aesthetic pleasures associated with classical aerodynamics. A key inspiration behind the present work was the thesis [78]. Here, a complicated hydrodynamic model was boiled down to a compact vectorial representation with clear physical properties. An immediate consequence was that simulation and control became far easier. The model is now accepted as the standard way of representing marine vessels within the control community. A great deal of effective control methodologies were facilitated by the clarity and physical soundness of the representation. The models of wind engineering are often complex and geared towards other purposes than control theory. The field would benefit greatly from a model akin to that proposed in [78]. This work hopes to push current research towards such a goal.

On a more practical note, the destabilization phenomena does indeed appear to be solved. It has been demonstrated that the energy shaping stabilization method works, both with theory and simulation. This is accomplished with an extremely simple reference model that can be implemented directly on most wind turbine regulators.

Topics for Further Research

It appears possible to generalize Dynamic Vortex Theory to nonuniform loading and inflow whilst retaining the underlying structure described in Chapter 3. Since the very basic method presented herein performs well compared to experiment, further improvements may be obtained through generalization. It is hoped that the underlying ideas have been presented clearly enough that other researchers can pick up the thread. Inflow dynamics under yawed conditions are deviously difficult, see e.g. Snel and Schepers [73]. The impulse response approach developed herein could furnish an improved understanding of these phenomena.

The parametric model developed in Chapter 4 works very well with VSVP wind turbines. However, for fixed speed types it underperforms. The reason being that a quadratic drag model $b_d\Omega^2$ is too crude. It may be possible to find improved representations, but this must be done in manner that does not encumber the minimalistic form of the representation.

Another suggestion for further research opportunities is the development of true nonlinear control strategies on the parametric wind turbine model. This author was unsuccessful in that quest; the reversal problem inherent in the model structure appeared to prohibit the application of standard approaches from nonlinear control theory. The fact that one cannot passivate the plant whilst simultaneously regulating the internal states implies some sort of underactuation. A closer look at this problem could be quite fruitful.

Finally, and perhaps most importantly; circulatory loading models seem almost absent from the aerospace control field. This author did not find a single reference describing this viewpoint. The thesis is therefore concluded with a small example that could stimulate research efforts in this direction. Let the position of a straight flying wing, defined in a plane normal to the lifting line, by denoted by $\boldsymbol{x} = \mathrm{col}[x, z]$. Here z denotes the altitude of the wing whereas x denotes the horizontal coordinate. The vectorial lifting law used in Chapter 3 predicts the dynamics

$$m \begin{bmatrix} \ddot{x} \\ \ddot{z} \end{bmatrix} = \begin{bmatrix} 0 & -\Gamma \\ \Gamma & 0 \end{bmatrix} \begin{bmatrix} \dot{x} \\ \dot{z} \end{bmatrix} - \begin{bmatrix} 0 \\ mg \end{bmatrix} \tag{6.1}$$

Assuming small perturbations about a steady rate of translation $\dot{\boldsymbol{x}} = \mathrm{col}[U, 0]$ yields the first order approximation

$$\begin{bmatrix} \delta\ddot{x} \\ \delta\ddot{z} \end{bmatrix} = \frac{g}{U} \begin{bmatrix} 0 & -1 \\ 1 & 0 \end{bmatrix} \begin{bmatrix} \delta\dot{x} \\ \delta\dot{z} \end{bmatrix} \tag{6.2}$$

This is the phugoid mode, a well known phenomena in flight stability [79]. Noting the simple analysis, circulatory loading models seems to have potential for flight dynamics. There is much more to know.

A. Hydroelastic model

The variable $\dot{x}$ is used to describe backwards nacelle motion. Here, some properties of the relation between the force F and $\dot{x}$ are deduced. The structural model will depend on the particulars of the support structure as well as the rotor design. It will however be possible to uncover some salient properties of a more general nature. This section aims to show that a wide variety of support structures shares the common property of passivity, despite significant differences in the actual physical design.

A.1. Lagrangian mechanics

It is now assumed that platform deformations may be parameterized *linearly* in terms of n generalized coordinates q_i. Time-invariant dynamics are also assumed. It is well known that the dynamics of mechanical systems can be derived from the principle of least action [80]. The Lagrangian of a linear plant will have the general form

$$\mathcal{L}(\boldsymbol{q}, \dot{\boldsymbol{q}}) = \frac{1}{2}\dot{\boldsymbol{q}}^T \boldsymbol{M}\dot{\boldsymbol{q}} - \frac{1}{2}\boldsymbol{q}^T \boldsymbol{K}\boldsymbol{q}$$
$$\boldsymbol{M} = \boldsymbol{M}^T, \quad \boldsymbol{M} \succ 0, \quad \boldsymbol{K} = \boldsymbol{K}^T, \quad \boldsymbol{K} \succ 0 \quad \text{(A.1)}$$

The mass and stiffness matrices are positive definite and symmetric. Dissipation is incorporated through the use of a Rayleigh dissipation function, viz.

$$\mathcal{R}(\dot{\boldsymbol{q}}) = \frac{1}{2}\dot{\boldsymbol{q}}^T \boldsymbol{D}\dot{\boldsymbol{q}}, \quad \boldsymbol{D} = \boldsymbol{D}^T, \quad \boldsymbol{D} \succ 0 \quad \text{(A.2)}$$

A symmetric and positive definite damping matrix implies that all structural modes will decay asymptotically in the absence of a perturbing force. This is a reasonable assumption. The equations of motion follow from

$$\frac{d}{dt}\left[\frac{\partial \mathcal{L}}{\partial \dot{\boldsymbol{q}}}^T\right] - \frac{\partial \mathcal{L}}{\partial \boldsymbol{q}}^T + \frac{\partial \mathcal{R}}{\partial \dot{\boldsymbol{q}}} = \boldsymbol{Q} \quad \text{(A.3)}$$

The generalized force $\boldsymbol{Q}$ consists of an aerodynamic term and a hydrodynamic term

$$\boldsymbol{Q} = \boldsymbol{Q}_A + \boldsymbol{Q}_H \quad \text{(A.4)}$$

Here, the aerodynamic constituent is readily computed. Since the net structural motion $\dot{x}$ must relate linearly to the internal states of the plant one can write

$$\dot{x} = \boldsymbol{b}^T \dot{\boldsymbol{q}} \quad \text{(A.5)}$$

Here, $\boldsymbol{b}$ is a constant column vector with as many elements as $\boldsymbol{q}$. The elements of $\boldsymbol{b}$ are taken as non-zero. Conservation of energy can be applied to identify the generalized forces due to the thrust force. Define the generalized aerodynamic force by

$$\boldsymbol{Q}_A \triangleq \boldsymbol{b}F \tag{A.6}$$

This is the correct expression since, in accordance with conservation of energy, one must require that

$$\boldsymbol{Q}_A^T \dot{\boldsymbol{q}} = F\dot{x} \tag{A.7}$$

The hydrodynamic forcing $\boldsymbol{Q}_H$ requires additional physics.

A.2. Hydrodynamic forces

The assumption of linearly parameterized motion is now extended to encompass motion of the submerged platform. We follow Damaren [29] closely since this work considers the hydrodynamic forces on bodies whose motion is linearly parameterized. The problem is also discussed in e.g. Kristiansen et al. [81], albeit for the restricted case of rigid-body motion.

Summarizing [29], the hydrodynamic force can be given in the Laplace domain as

$$\boldsymbol{Q}_H(s) = \boldsymbol{f}_R(s) + \boldsymbol{f}_D(s) - \boldsymbol{G}\boldsymbol{q}(s) \tag{A.8}$$

Here $\boldsymbol{f}_R$ and $\boldsymbol{f}_D$ represent the radiation and diffraction forces, respectively. These contributions are presented in [29] as

$$\boldsymbol{f}_R(s) = -\boldsymbol{A}\ddot{\boldsymbol{q}}(s) - \boldsymbol{H}(s)\dot{\boldsymbol{q}}(s), \quad \boldsymbol{f}_D(s) = \boldsymbol{X}(s)A(s) \tag{A.9}$$

Note here that the cited work uses the notation $\boldsymbol{H}(s) = s\boldsymbol{A} + \boldsymbol{H}_r(s)$. Hydrostatic restoring forces are captured by $\boldsymbol{G}\boldsymbol{q}(s)$ which incorporates both buoyancy and gravity effects. The constant infinite-frequency added-mass matrix $\boldsymbol{A}$ and restoring matrix $\boldsymbol{G}$ are both symmetric and positive semi-definite

$$\boldsymbol{A} = \boldsymbol{A}^T, \quad \boldsymbol{A} \succeq 0, \quad \boldsymbol{G} = \boldsymbol{G}^T, \quad \boldsymbol{G} \succeq 0 \tag{A.10}$$

The fluid-memory effects represented by $\boldsymbol{H}(s)$ ensure that energy is carried away from the support structure. The transfer function $\boldsymbol{H}(s)$ is therefore positive real and also strictly proper. These qualities are guaranteed by

$$\boldsymbol{H}(\jmath\omega) + \boldsymbol{H}(-\jmath\omega)^T \succeq 0, \quad \lim_{s\to\infty} \boldsymbol{H}(s) = \boldsymbol{0} \tag{A.11}$$

and the requirement that all poles of $H_{ij}(s)$ lie in the closed LHP $\Re\{s\} \leq 0$. There are no repeated poles on the imaginary axis.

The structure of the equations suggest the definition of a *hydroelastic* Lagrangian

$$\mathcal{L}_{\text{he}}(\boldsymbol{q}, \dot{\boldsymbol{q}}) = \frac{1}{2}\dot{\boldsymbol{q}}^T(\boldsymbol{M} + \boldsymbol{A})\dot{\boldsymbol{q}} - \frac{1}{2}\boldsymbol{q}^T(\boldsymbol{K} + \boldsymbol{G})\boldsymbol{q} \tag{A.12}$$

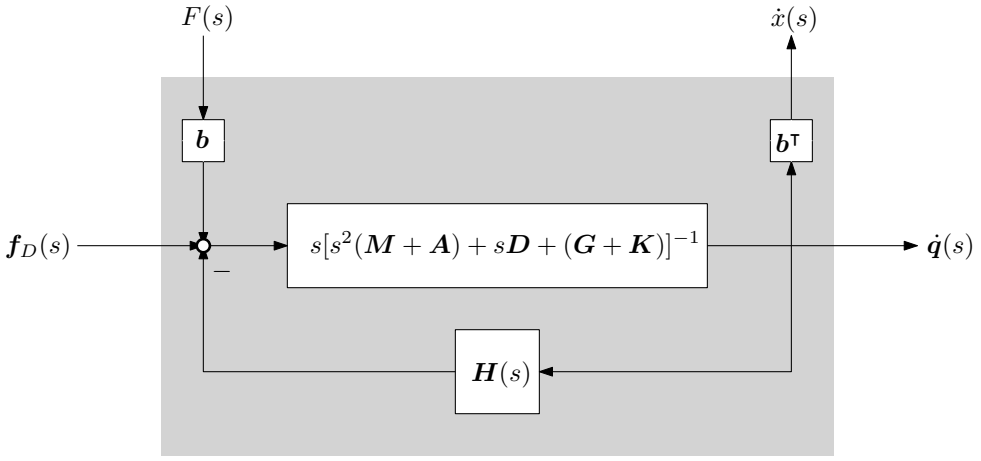

Figure A.1.: Hydroelastics on block diagram form.

The resulting dynamics are driven by a force where the added-mass contribution and restoring term have been subtracted. That is

$$\begin{aligned}&\frac{d}{dt}\left[\frac{\partial \mathcal{L}_{\text{he}}}{\partial \dot{\boldsymbol{q}}}^\mathsf{T}\right] - \frac{\partial \mathcal{L}_{\text{he}}}{\partial \boldsymbol{q}}^\mathsf{T} + \frac{\partial \mathcal{R}}{\partial \dot{\boldsymbol{q}}} \\ &= (\boldsymbol{M}+\boldsymbol{A})\ddot{\boldsymbol{q}} + \boldsymbol{D}\dot{\boldsymbol{q}} + (\boldsymbol{K}+\boldsymbol{G})\boldsymbol{q} = \boldsymbol{f}_D + \boldsymbol{b}F - \int_0^t \boldsymbol{H}(t-t')\dot{\boldsymbol{q}}(t')\,dt' \quad \text{(A.13)}\end{aligned}$$

A graphical illustration of this equation is shown in Figure A.1.

A.2.1. Model properties

The positive definite *hydroelastic* Hamiltonian of the plant is given by

$$\mathcal{H}_{\text{he}}(\boldsymbol{q},\dot{\boldsymbol{q}}) = \frac{\partial \mathcal{L}_{\text{he}}}{\partial \dot{\boldsymbol{q}}}(\boldsymbol{q},\dot{\boldsymbol{q}})\dot{\boldsymbol{q}} - \mathcal{L}_{\text{he}}(\boldsymbol{q},\dot{\boldsymbol{q}}) = \frac{1}{2}\dot{\boldsymbol{q}}^\mathsf{T}(\boldsymbol{M}+\boldsymbol{A})\dot{\boldsymbol{q}} + \frac{1}{2}\boldsymbol{q}^\mathsf{T}(\boldsymbol{K}+\boldsymbol{G})\boldsymbol{q} \quad \text{(A.14)}$$

Now verify that the rate of change in internal energy follows from

$$\dot{\mathcal{H}}_{\text{he}} = \dot{\boldsymbol{q}}^\mathsf{T}\boldsymbol{f}_D + \dot{x}F - \dot{\boldsymbol{q}}^\mathsf{T}\boldsymbol{D}\dot{\boldsymbol{q}} - \int_0^t \dot{\boldsymbol{q}}(t)^\mathsf{T}\boldsymbol{H}(t-t')\dot{\boldsymbol{q}}(t')\,dt' \quad \text{(A.15)}$$

The very last term can be reduced to an inequality by utilizing the positive-real property of $\boldsymbol{H}(s)$ [65].

$$\int_0^t \dot{\boldsymbol{q}}(t)^\mathsf{T}\boldsymbol{H}(t-t')\dot{\boldsymbol{q}}(t')\,dt' \geq 0 \quad \text{(A.16)}$$

Physically, this relationship reflects dissipation due to wave radiation. The damping matrix $\boldsymbol{D}$ is positive definite. Let $\varrho_1 > 0$ and $\varrho_2 > 0$ denote positive

constants small enough to ensure that the following matrix is positive semi-definite

$$\boldsymbol{D} - \varrho_1 \boldsymbol{b}\boldsymbol{b}^T - \varrho_2 \boldsymbol{I}_n \succeq 0 \tag{A.17}$$

Then, the following bound can be established

$$\dot{\boldsymbol{q}}^T \boldsymbol{f}_D + \dot{x}F \geq \dot{\mathcal{H}}_{\text{he}} + \varrho_2 \dot{\boldsymbol{q}}^T \dot{\boldsymbol{q}} + \varrho_1 \dot{x}^2 \tag{A.18}$$

Let $\mathcal{H}_{\text{he}}$ be interpreted as a positive definite storage function. Furthermore, let the vectors $\boldsymbol{u}_{\text{he}} \triangleq \text{col}[F, \boldsymbol{f}_D]$ and $\boldsymbol{y}_{\text{he}} \triangleq \text{col}[\dot{x}, \dot{\boldsymbol{q}}]$ serve respectively as input and output. These definitions permits the classification of (A.13) as an *output strictly passive* system. See [21, Definition 6.3].

Denote the transfer function from thrust to net structural motion by

$$H(s) = \frac{\dot{x}}{F}(s) = s\boldsymbol{b}^T[s^2(\boldsymbol{M} + \boldsymbol{A}) + s(\boldsymbol{D} + \boldsymbol{H}(s)) + (\boldsymbol{K} + \boldsymbol{G})]^{-1}\boldsymbol{b} \tag{A.19}$$

Setting $\boldsymbol{f}_D = 0$ in (A.18) allows the following useful conclusions to be struck about the transfer function.

1. The transfer function $H(s)$ is *positive real* so that

$$\Re[H(\jmath\omega)] \geq 0, \ \forall\omega \tag{A.20}$$

   This follows from the KYP-lemma. See Lemma 6.4 in [21] for a mathematical proof. An equivalent statement on the phase is that

$$-\pi \leq \angle H(\jmath\omega) \leq \pi \tag{A.21}$$

2. The gain of $H(s)$ is equipped with an upper bound given by

$$\sup_{\omega} |H(\jmath\omega)| \leq \frac{1}{\varrho_1} \tag{A.22}$$

   See Theorem 5.4 and Lemma 6.5 in [21].

3. The poles of $H(s)$ have negative real parts.

Due to linearity, these properties also hold for models perturbed around an equilibrium point, e.g. $\boldsymbol{q}(t) = \bar{\boldsymbol{q}} + \delta\boldsymbol{q}(t)$.

Bibliography

[1] F. L., L. Q., S. S., and S. S., "Global wind report, annual market update 2015," Global Wind Energy Council (GWEC), April 2016.

[2] W. Musial, S. Butterfield, and B. Ram, "Energy from offshore wind," in *Offshore Technology Conference*, Offshore Technology Conference. Society of Petroleum Engineers, 2006.

[3] I. Rummelhoff and S. Bull, "Building the world's first floating offshore wind farm," Presentation from https://www.statoil.com, November 2015.

[4] F. G. Nielsen, T. D. Hanson, and B. Skaare, "Integrated dynamic analysis of floating offshore wind turbines," in *25th International Conference on Offshore Mechanics and Arctic Engineering*. American Society of Mechanical Engineers, 2006, pp. 671–679.

[5] T. J. Larsen and T. D. Hanson, "A method to avoid negative damped low frequent tower vibrations for a floating, pitch controlled wind turbine," in *Journal of Physics: Conference Series*, vol. 75, no. 1. IOP Publishing, 2007, p. 012073.

[6] J. M. Jonkman, "Influence of control on the pitch damping of a floating wind turbine," NREL, Tech. Rep. NREL/CP-500-42589, 2008.

[7] H. Namik and K. Stol, "Control methods for reducing platform pitching motion of floating wind turbines," in *European offshore wind 2009*, 2009.

[8] ——, "Individual blade pitch control of floating offshore wind turbines," *Wind energy*, vol. 13, no. 1, pp. 74–85, 2010.

[9] M. A. Lackner, "Controlling platform motions and reducing blade loads for floating wind turbines," *Wind Engineering*, vol. 33, no. 6, pp. 541–553, 2009.

[10] ——, "An investigation of variable power collective pitch control for load mitigation of floating offshore wind turbines," *Wind Energy*, vol. 16, no. 4, pp. 519–528, 2013.

[11] D. Schlipf, F. Sandner, S. Raach, D. Matha, and P. W. Cheng, "Nonlinear model predictive control of floating wind turbines," in *The Twenty-third International Offshore and Polar Engineering Conference*. International Society of Offshore and Polar Engineers, 2013.

[12] B. Skaare and F. G. Nielsen, "Blade pitch control in a wind turbine installation." U.S. Patent 8,487,464 B2, July 16, 2013.

[13] J. M. Jonkman, S. Butterfield, W. Musial, and G. Scott, "Definition of a 5-mw wind turbine for offshore system development," National Renewable Energy Laboratory, Technical Report NREL/TP-500-38060, February 2009.

[14] A. J. Goupee, B. J. Koo, R. W. Kimball, K. F. Lambrakos, and H. J. Dagher, "Experimental comparison of three floating wind turbine concepts," *Journal of Offshore Mechanics and Arctic Engineering*, vol. 136, no. 2, p. 020906, 2014.

[15] O. Faltinsen, "Sea loads on ships and offshore structures," ser. Cambridge Ocean Technology Series, I. Dyer, E. Taylor, N. J.N., and P. W.G., Eds. Cambridge university press, 1990, no. 1.

[16] B. Brogliato, R. Lozano, B. Maschke, and O. Egeland, *Dissipative Systems Analysis and Control*, 2nd ed., ser. Communications and Control Engineering Series, E. Sontag, M. Thoma, A. Isidori, and J. van Schuppen, Eds. Springer, 2007.

[17] A. Monroy, L. Alvarez-Icaza, and G. Espinosa-Perez, "Passivity-based control for variable speed constant frequency operation of a dfig wind turbine," *International Journal of control*, vol. 81, no. 9, pp. 1399–1407, 2008.

[18] R. Fernández, R. Mantz, and P. Battaiotto, "Wind farm control for stabilisation of electrical networks based on passivity," *International Journal of Control*, vol. 83, no. 1, pp. 105–114, 2010.

[19] F. Valenciaga, P. F. Puleston, and P. E. Battaiotto, "Power control of a solar/wind generation system without wind measurement: A passivity/sliding mode approach," *IEEE Transactions on Energy Conversion*, vol. 18, no. 4, pp. 501–507, 2003.

[20] T. I. Fossen, *Handbook of marine craft hydrodynamics and motion control*, 1st ed. Chichester, West Sussex: John Wiley & Sons Ltd., 2011.

[21] H. K. Khalil, *Nonlinear systems*. Prentice Hall, 2002.

[22] A. Van der Schaft, *L2-gain and passivity techniques in nonlinear control*. Springer Science & Business Media, 2012.

[23] F. D. Bianchi, H. De Battista, and R. J. Mantz, *Wind turbine control systems : principles, modelling and gain scheduling design*, ser. Advances in industrial control,. London: Springer, 2007.

[24] G. J. W. Van Bussel, "The aerodynamics of horizontal axis wind turbine rotors explored with asymptotic expansion methods," Ph.D. dissertation, Technische Universiteit Delft, 1995.

[25] D. A. Peters and N. HaQuang, "Dynamic inflow for practical applications," *Journal of the American Helicopter Society*, vol. 33, no. 4, 10 1988.

[26] K. Merz and M. D. Pedersen, *Offshore Wind Energy Technology; Offshore wind turbine controls.* John Wiley & Sons Limited, 2017, ch. 5.

[27] M. Pedersen, "Steady and transient inflow dynamics with actuator disk vortex theory," *Wind Energy*, 2017, submitted for review August 2015.

[28] M. D. Pedersen and T. I. Fossen, "Efficient nonlinear wind-turbine modeling for control applications," *IFAC Proceedings Volumes*, vol. 45, no. 2, pp. 264–269, 2012.

[29] C. J. Damaren, "Time-domain floating body dynamics by rational approximation of the radiation impedance and diffraction mapping," *Ocean Engineering*, vol. 27, no. 6, pp. 687–705, 2000.

[30] I. Van der Hoven, "Power spectrum of horizontal wind speed in the frequency range from 0.0007 to 900 cycles per hour," *Journal of Meteorology*, vol. 14, no. 2, pp. 160–164, 1957.

[31] T. Burton, D. Sharpe, N. Jenkins, and E. Bossanyi, *Wind Energy Handbook.* Chichester, West Sussex: John Wiley & Sons Ltd., 2001.

[32] W. Leithead, S. De la Salle, and D. Reardon, "Role and objectives of control for wind turbines," in *IEE Proceedings C (Generation, Transmission and Distribution)*, vol. 138, no. 2. IET, 1991, pp. 135–148.

[33] E. Welfonder, R. Neifer, and M. Spanner, "Development and experimental identification of dynamic models for wind turbines," *Control Engineering Practice*, vol. 5, no. 1, pp. 63 – 73, 1997.

[34] L. Kristensen and S. Frandsen, "Model for power spectra of the blade of a wind turbine measured from the moving frame of reference," *Journal of Wind Engineering and Industrial Aerodynamics*, vol. 10, no. 2, pp. 249–262, 1982.

[35] R. E. Froude, "On the part played in propulsion by difference in pressure," *Transaction of the Institute of Naval Architects*, vol. 30, pp. 390–423, 1889.

[36] W. Johnson, *Helicopter theory.* New York: Dover Publications, 1994.

[37] Q. R. Wald, "The aerodynamics of propellers," *Progress in Aerospace Sciences*, vol. 42, no. 2, pp. 85–128, 2006.

[38] P. R. Spalart, "On the simple actuator disk," *Journal of Fluid Mechanics*, vol. 494, pp. 399–405, 2003.

[39] M. O. L. Hansen, *Aerodynamics of wind turbines*, 2nd ed. London: Earthscan, 2008.

[40] S. F. Hoerner, *Fluid-dynamic drag; practical information on aerodynamic drag and hydrodynamic resistance.* Midland Park, N.J.: Published by the Author, 1965.

[41] R. E. Wilson and P. B. S. Lissaman, "Applied aerodynamics of wind power machines," Oregon State University, Tech. Rep., May 1974.

[42] P.-Å. Krogstad and P. E. Eriksen, "Blind test calculations of the performance and wake development for a model wind turbine," *Renewable energy*, vol. 50, pp. 325–333, 2013.

[43] D. Simms, S. Schreck, M. Hand, and L. Fingersh, "Nrel unsteady aerodynamics experiment in the nasa-ames wind tunnel: a comparison of predictions to measurements," *National Renewable Energy Laboratory, Golden, CO, Report No. NREL/TP-500-29494*, 2001.

[44] J. Jonkman, *Fast theory manual.* Golden, CO: National Renewable Energy Laboratory, 2013.

[45] T. J. Larsen and A. M. Hansen, "How 2 hawc2, the user's manual," Risø National Laboratory, Tech. Rep., 2007.

[46] P. J. Moriarty and A. C. Hansen, *AeroDyn theory manual.* Golden, CO: National Renewable Energy Laboratory, 2005.

[47] A. Platt and M. J. Buhl, *Wt perf user guide for version 3.05.* Golden, CO: National Renewable Energy Laboratory, 2012.

[48] K. E. Johnson, L. Y. Pao, M. J. Balas, and L. J. Fingersh, "Control of variable-speed wind turbines: standard and adaptive techniques for maximizing energy capture," *IEEE control systems*, vol. 26, no. 3, pp. 70–81, 2006.

[49] E. Bossanyi, "The design of closed loop controllers for wind turbines," *Wind energy*, vol. 3, no. 3, pp. 149–163, 2000.

[50] M. H. Hansen, A. D. Hansen, T. J. Larsen, S. , P. S, and P. Fuglsang, "Control design for a pitch-regulated, variable speed wind turbine," Risø-National Laboratory, Tech. Rep. Risø-R-1500(EN), January 2005.

[51] W. Leithead and B. Connor, "Control of variable speed wind turbines: dynamic models," *International Journal of Control*, vol. 73, no. 13, pp. 1173–1188, 2000.

[52] N. Joukowsky, "Vortex theory of screw propellers, i." *Trudy Otdeleniya Fizicheskikh Nauk. Obshchestva Lubitelei Estestvoznaniya.*, vol. 16, no. 1, pp. 1–31, 1912.

[53] J. Katz and A. Plotkin, *Low speed aerodynamics*, 2nd ed., ser. Cambridge aerospace series. Cambridge, UK ; New York: Cambridge University Press, 2001.

[54] V. L. Okulov and J. N. Sørensen, "Maximum efficiency of wind turbine rotors using joukowsky and betz approaches," *Journal of Fluid Mechanics*, vol. 649, pp. 497–508, 2010.

[55] R. Krasny, "Computation of vortex sheet roll-up in the trefftz plane," *Journal of Fluid Mechanics*, vol. 184, pp. 123–155, 1987.

[56] L. Prandtl, "Applications of modern hydrodynamics to aeronautics," National Advisory Committee for Aeronautics, Tech. Rep. 116, 1923.

[57] V. L. Okulov, J. N. Sørensen, and D. H. Wood, "The rotor theories by professor joukowsky: Vortex theories," *Progress in Aerospace Sciences*, vol. 73, pp. 19–46, 2015.

[58] G. van Kuik, J. N. Sørensen, and V. Okulov, "Rotor theories by professor joukowsky: momentum theories," *Progress in Aerospace Sciences*, vol. 73, pp. 1–18, 2015.

[59] W. Phillips and D. Snyder, "Modern adaptation of prandtl's classic lifting-line theory," *Journal of Aircraft*, vol. 37, no. 4, pp. 662–670, 2000.

[60] P. G. Saffman, *Vortex dynamics*, 1st ed., ser. Cambridge monographs on mechanics and applied mathematics. Cambridge, New York: Cambridge University Press, 1995.

[61] H. Lamb, *Hydrodynamics*, 4th ed. Cambridge: Cambridge University Press, 1916.

[62] J. T. Conway, "Analytical solutions for the actuator disk with variable radial distribution of load," *Journal of Fluid Mechanics*, vol. 297, pp. 327–355, 1995.

[63] R. Miller, "Vortex theory for hovering rotors," *AIAA Journal*, vol. 20, no. 12, pp. 1754–1756, 1982.

[64] T. Theodorsen, "General theory of aerodynamic instability and the mechanism of flutter," NACA, Tech. Rep. 496, 1935.

[65] N. Kottenstette and P. J. Antsaklis, "Relationships between positive real, passive dissipative, & positive systems," in *Proceedings of the 2010 American control conference*. IEEE, 2010, pp. 409–416.

[66] B. Gustavsen and A. Semlyen, "Rational approximation of frequency domain responses by vector fitting," *IEEE Transactions on power delivery*, vol. 14, no. 3, pp. 1052–1061, 1999.

[67] B. Gustavsen, "Matrix fitting toolbox," *User's guide and reference, SINTEF Energy Research*, 2009.

[68] S. Øye, "Unsteady wake effects caused by pitch–angle changes," in *IEA R&D WECS Joint Action on Aerodynamics of Wind Turbines, 1st Symposium*, 1986, pp. 58–79.

[69] P. J. Carpenter and B. Fridovich, "Effect of a rapid blade-pitch increase on the thrust and induced-velocity response of a full-scale helicopter rotor," NACA, Langley Aeronautical Laboratory, Langley Field, Va., Tech. Rep. Technical Note 3044, 1953.

[70] D. M. Pitt and D. A. Peters, "Theoretical prediction of dynamic-inflow derivatives," *Vertica*, vol. 5, no. 1, pp. 21–34, 1981.

[71] W. Kinner, "Über tragflügel mit kreisförmigem grundriß," *ZAMM-Journal of Applied Mathematics and Mechanics/Zeitschrift für Angewandte Mathematik und Mechanik*, vol. 16, no. 6, pp. 349–352, 1936.

[72] D. A. Peters, D. D. Boyd, and C. J. He, "Finite-state induced-flow model for rotors in hover and forward flight," *Journal of the American Helicopter Society*, vol. 34, no. 4, pp. 5–17, 1989.

[73] H. Snel and J. Schepers, "Joint investigation of dynamic inflow effects and implementation of an engineering method," Netherlands Energy Research Foundation ECN, Tech. Rep., 1995.

[74] I. ELSAM, "The tjæreborg wind turbine," Elsamprosjekt A/S, Final Report EP92/334, 1992.

[75] S. Øye, "Tjæreborg wind turbine. 4. dynamic inflow measurements," Department of fluid mechanics, DTH Lyngby, AFM Notat VK 204, October 1991.

[76] R. C. Dorf and R. H. Bishop, *Modern control systems*, 12th ed. Upper Saddle River: Prentice Hall, 2010.

[77] M. Vidyasagar, "$\mathcal{L}_2$-stability of interconnected systems using a reformulation of the passivity theorem," *IEEE Transactions on Circuits and Systems*, vol. 24, no. 11, pp. 637–645, 1977.

[78] T. I. Fossen, *Nonlinear modelling and control of underwater vehicles*. Fakultet for informasjonsteknologi, matematikk og elektroteknikk, 1991.

[79] B. Etkin and L. D. Reid, *Dynamics of flight: stability and control.* New York: John Wiley & Sons Inc., 1996, vol. 3.

[80] H. Goldstein, C. P. Poole, and J. L. Safko, *Classical mechanics*, 3rd ed. San Francisco: Addison Wesley, 2002.

[81] E. Kristiansen, Å. Hjulstad, and O. Egeland, "State-space representation of radiation forces in time-domain vessel models," *Ocean Engineering*, vol. 32, no. 17, pp. 2195–2216, 2005.